

# **Electromanipulation of Ellipsoidal Cells in Fluidic Micro-Electrode Systems**

## **Dissertation**

zur

Erlangung des akademischen Grades

doctor rerum naturalium (Dr. rer. nat.)

der Mathematisch-Naturwissenschaftlichen Fakultät

der Universität Rostock

vorgelegt von

**Kanokkan Maswivat**

geb. am 25.03.1974

in Phatthalung, Thailand

Rostock, October 2007

**Referees:**

1. Prof. Dr. Jan Gimsa, University of Rostock (supervisor)
2. Prof. Dr. emer. Eberhard Neumann, University of Bielefeld

Date of doctoral examination: 17.03.2008

*Dedicated to my family for love and encouragement*

# Acknowledgements

I would like to acknowledge all those who have provided guidance and support while I was studying at the University of Rostock. First of all, I would like to thank my supervisor Prof. Dr. J. Gimsa for his valuable guidance, constructive suggestions and support throughout my study. I thank all referees for providing valuable suggestions and kindly being my co-examiners as well as Mr. R. Sleigh for his help with some manuscripts. I also thank Assoc. Prof. Dr. P. Wanichapichart from the Department of Physics, Faculty of Science, Prince of Songkla University for her recommendation and invaluable suggestion. I definitely thank D. Wachner for his fruitful discussions, encouragement and permanent willing to help.

I gratefully thank the minister-counsellor (Education), Mrs. S. Rungsinan and her group of the office of educational affairs in London as well as the group of Thai Students Consulting in Berlin for their consulting and support. I also thank Prof. Dr. D. G. Weiß as the head of Ph.D-commission at the institute of biology as well as Ms. P. Schmidtke at the international office, University of Rostock for their helpful consulting. I am grateful for a stipend of the Royal Thai government. This study has also partly been supported by grant StSch 20020418A of the Bundesamt für Strahlenschutz to Prof. Dr. J. Gimsa and by the IPP (International Postgraduate Programmes) at the University of Rostock supported by DAAD (Deutscher Akademischer Austauschdienst), BMBF (Bundesministerium für Bildung und Forschung) and DFG (Deutsche Forschungsgemeinschaft).

I kindly thank Ms. J. Donath and Ms. J. Sudsiri who taught me all experimental methods. Other members in the biophysics group that I wish to acknowledge are Dr. M-L Hubert, Dr. W. Baumann, Dr. J. Sakowski, Dr. W. Kröger, Dr. S. Kuznetsov, K-H Polack, R. Kühner, M. Holtappels, L. Haberland, Dr. A. Scheunemann, Dr. M. Simeonova, Dr. B. Habel, S. Lippert, M. Stubbe, C. Taurat, P. Köster, S. Bühler, K. Kröger, A. Podßun, H. Altrichter, J. Kern, R. Schrott, R. Warnke, C. Westendorf and M. Rose for their encouragements, helpful discussions and for being friends. I also thank Prof. Dr. L. Jonas from the “Electron Microscopy Centre” of the Medical Faculty, University of Rostock for the SEM micrographs.

Last but certainly not least, I would like to thank my mother and my daughter who strengthen my willpower. I also thank my husband for his persistence, encouragement and everlasting love.

## Abstract

Recently, electromanipulation technologies for handling and characterizing individual cells or particles have been applied to lab-on-chip devices. These devices play a role in pharmacological and clinical applications as well as environmental and nanotechnologies. Electromanipulation of ellipsoidal cells in fluidic micro-electrode systems has been studied by numerical simulations, theoretical analysis and experiment. The field distributions in electrorotation chip chambers were analyzed using numerical field simulations in combination with analytical post-processing. The optimal design for two-dimensional electrorotation chips features electrodes with pyramidal rounded tips. Moreover, the three-dimensional electric field distributions in the electroporation and electrorotation chambers were analyzed. The advantage of electroporation chip chambers is to avoid strongly increasing temperatures after pulse application. New chips may be developed for nanoscale applications in the future.

New simplified analytical equations have been developed for the transmembrane potential ( $\Delta\phi$ ) induced in cells resembling ellipsoids of rotation, i.e. spheroids, by homogeneous DC or AC fields. The new equations avoid the complicated description by the depolarizing factors. Also the dielectrophoretic force expression for spheroidal objects has been simplified. Furthermore, the effects of cell orientation and electric field frequency on the  $\Delta\phi$  induced in ellipsoidal cells were studied. Simplified equations were derived. They show that the membrane surface points for the maximum of  $\Delta\phi$  depend on cell shape, cell orientation, electric cell parameters and field frequency. The theoretical results were compared to electropermeabilization experiments with chicken red blood cells. Experiments confirmed that equations for the transmembrane potential were advantageous for describing the transmembrane potential induced in arbitrarily oriented ellipsoidal cells.

# Zusammenfassung

In letzter Zeit sind Elektromanipulations-Technologien für die Manipulation und die Charakterisierung von einzelnen Zellen oder Partikeln in Lab-on-Chip Systeme integriert worden. Die neuen Systeme spielen eine Rolle in pharmakologischen und klinischen Anwendungen sowie in Umwelt- und Nanotechnologien. Die Elektromanipulation von ellipsoiden Zellen in fluidischen Mikro-Elektrodensystemen wurde mit Hilfe numerischer Simulation, theoretischer Analyse sowie Experimenten beschrieben. Die Feldverteilung in Elektrorotationskammern wurde mit numerischen Simulationen analysiert und optimiert. Als geeignetes Elektrodendesign in zwei-dimensionalen Elektrorotationskammern erwiesen sich pyramidale, abgerundete Elektrodenspitzen. Zusätzlich wurden die drei-dimensionalen Feldverteilungen in den Elektroproportions- und Elektrorotationskammern analysiert, um starke Temperaturerhöhungen durch den elektrischen Puls zu vermeiden. Mit diesen Ergebnissen könnten neue Chips für Anwendungen im Nanometerbereich entwickelt werden.

Neue und vereinfachte analytische Gleichungen für das Transmembranpotential ( $\Delta\phi$ ), welches in einem homogenen Gleich- oder Wechselfeld in Zellen ähnlich Rotationsellipsoiden, d.h. Spheroide, induziert wird, wurden unter Vermeidung der Depolarisierungsfaktoren hergeleitet. Ebenso wurde die Gleichung für die dielektrophoretische Kraft auf spheroide Objekte vereinfacht, sowie die Effekte von Zellorientierung und Frequenz des Wechselfeldes auf das  $\Delta\phi$  von ellipsoiden Zellen untersucht und vereinfachte Gleichungen abgeleitet. Sie zeigen, dass die Membranpunkte mit maximalem  $\Delta\phi$  abhängig sind von der Zellform, der Zellorientierung, den elektrischen Eigenschaften der Zelle und der Frequenz des Wechselfeldes. Die theoretischen Ergebnisse wurden mit Experimenten zur Elektropermeabilität von Hühnererythrozyten verglichen, die bestätigten, dass die vereinfachten Gleichungen das in beliebig orientierten elliptischen Zellen induzierte Transmembranpotential richtig beschreiben.

# Content

<b>List of Abbreviations.....</b>	<b>xi</b>
<b>1 Introduction.....</b>	<b>1</b>
1.1 Electromanipulation of cells .....	1
1.1.1 Overview of electromanipulation.....	1
1.1.2 Microfluidic devices .....	2
1.1.3 Electropermeabilization.....	3
1.1.4 Electrofusion.....	6
1.1.5 Cell movement in AC-fields.....	7
1.2 Aims.....	9
<b>2 Numerical electric field simulations in microfluidic systems.....</b>	<b>11</b>
2.1 Optimizing the electrode shape for four-electrode electrorotation chips.....	11
2.2 Electric field distribution in three-dimensional electroporation and electrorotation chambers.....	15
<b>3 Materials and Methods.....</b>	<b>17</b>
3.1 Microfluidic chips design.....	17
3.1.1 Electroporation chip.....	17
3.1.2 Electrorotation chip.....	19
3.1.3 Traveling-wave chip.....	20
3.1.4 Chip carriers.....	21
3.2 Electropermeabilization instrumentation.....	23
3.3 Temperature sensor calibration.....	25
3.4 Cells and solutions.....	25
3.4.1 Alsever's solution.....	26
3.4.2 Phosphate buffer solution.....	26
3.4.3 Measuring solution.....	27



# Content

<b>4 Transmembrane potential induced in ellipsoidal cells.....</b>	<b>28</b>
4.1 Simplified equations for the transmembrane potential induced in ellipsoidal cells of rotational symmetry.....	28
4.1.1 Introduction.....	28
4.1.2 Simplification of $\Delta\phi$ for spheroids at high frequencies.....	29
4.2 Effects of cell orientation and electric field frequency on the transmembrane potential induced in ellipsoidal cells.....	32
4.3 Electroporation experiments.....	32
4.3.1 On-chip temperature sensor calibration.....	32
4.3.2 Temperature changes in the chambers by pulse application.....	34
4.3.3 Shape of chicken red blood cells.....	36
4.3.4 Conductivity of cell suspensions.....	39
4.3.5 Electroporation of oriented chicken red blood cells in linear square-wave AC-fields.....	40
4.3.6 Electroporation of chicken red blood cells in square-wave rotating electric fields.....	47
<b>5 Simplifications of dielectrophoretic force.....</b>	<b>52</b>
5.1 Introduction.....	52
5.2 Simplifications of dielectrophoretic force for spheroidal cells.....	53
5.3 Simplifications for zero membrane conductance.....	58
5.4 Simplifications for the cytoplasmic conductivity infinitely higher than the external conductivity.....	59
<b>6 Conclusions.....</b>	<b>60</b>

# Content

<b>Appendix.....</b>	<b>63</b>
<b>Appendix A</b> Paper 1: <u>Maswiat K</u> , Holtappels M and Gimsa J 2006 On the field distribution in electrorotation chambers-influence of electrode shape. <i>Electrochimica Acta</i> <b>51</b> 5215-20.....	63
<b>Appendix B</b> Paper 2: <u>Maswiat K</u> , Holtappels M and Gimsa J 2007a Optimizing the electrode shape for four-electrode electrorotation chips. <i>ScienceAsia</i> <b>33</b> 61-7.....	70
<b>Appendix C</b> Paper 3: <u>Maswiat K</u> , Wachner D, Warnke R and Gimsa J 2007b Simplified equations for the transmembrane potential induced in ellipsoidal cells of rotational symmetry. <i>J. Phys. D: Appl. Phys.</i> <b>40</b> 914-23 .....	78
<b>Appendix D</b> Submitted manuscript: <u>Maswiat K</u> , Wachner D and Gimsa J 2007 Effects of cell orientation and electric field frequency on the transmembrane potential induced in ellipsoidal cells.....	89
 <b>Bibliography.....</b>	 <b>131</b>
<b>Erklärung.....</b>	<b>149</b>
<b>Curriculum vitae.....</b>	<b>150</b>
<b>List of Publications and Presentations.....</b>	<b>152</b>

## List of Abbreviations

AC	Alternating current
CMF	Clausius Mossotti factor
CRBCs	Chicken red blood cells
DC	Direct current
DP	Dielectrophoresis
ECC	Electroconformational coupling
ED	Electrodeformation
EO	Electroorientation
EP	Electroporation
ER	Electrorotation
LBM	Lipid bilayer membrane
PB	Phosphate buffer
PI	Propidium iodide
RF	Radio-frequency
SEM	Scanning Electron Microscopy
SMB	Subminiature B
SMD	Surface mount device
TWD	Traveling-wave dielectrophoresis

---

# Chapter 1 Introduction

## 1.1 Electromanipulation of cells

### 1.1.1 Overview of electromanipulation

Electromanipulation of cells is applied in many areas of biotechnology and biomedicine. Electroinjection, electrorotation (ER), dielectrophoresis (DP), electroorientation (EO), electrodeformation (ED) and electrofusion are standard electromanipulation techniques. Electroinjection (also called electroporation (EP) or electrotransfection in the case of plasmid injection) as well as electrofusion following the dielectrophoretic alignment of cells may be the most important electromanipulation techniques (Chang *et al.* 1992, Glaser 2001, Neumann *et al.* 1989 and Zimmermann and Neil 1996). Both methods are based on the induction of a potential difference across the membrane by an external electric field. Besides these applications, the induced transmembrane potential ( $\Delta\phi$ ) became also important for new medical therapies.

Although phenomena like the electric alignment of freely suspended cells (DP) and the electric disruption of the cell membrane were already described in the mid 20<sup>th</sup> century, the fundamentals of the more sophisticated cellular electromanipulation techniques in fluidic microstructures are based on very recent developments. Meanwhile, the power of these technologies in handling and characterizing individual cells or particles has been recognized. Despite the increasing number of groups working in this field most probably not all possible principles that can be applied in so called lab-on-chip devices have been elaborated, yet. In future, microscopic systems combining electronic, optic and microfluidic parts will provide the means for investigating and handling individual particles from cellular down to molecular dimensions. These devices will allow for following changes in the physiological status of individual cells, for the characterization of viruses or DNA molecules, etc.

### 1.1.2 Microfluidic devices

Andersson and Berg (2003) have summarized several reasons making microfluidic devices and systems interesting for cellomics (see also Fuhr *et al.* 1997):

- Increased interest in biochemical experimentation/analysis of living single cells
- Possibility of uncomplicated integration of all kinds of analytical standard operations into microfluidic systems
- Several methods for manipulating large numbers of cells simultaneously can be used.
- The size of cells fits very well with that of commonly used fluidic devices (10-100  $\mu\text{m}$ ).
- Micromechanical devices are very well capable of manipulating single objects with cellular dimensions.
- Using geometries with small dimensions large electrical field strengths can be obtained with small voltage.
- Heat and mass transfer are very fast in microfluidic systems.

Microfluidic devices and systems have been developed for analysis of living cells, e.g. cell sampling, cell trapping and sorting, cell treatment and cell analysis (Andersson and Berg 2003). In recent years, several publications have focused on the process of EP in microfluidic devices produced by microfabrication techniques. BTX (BTX Instrument Division Harvard Apparatus, Inc., Massachusetts, US), the leader in EP products and specialty electrodes, has developed a new and innovative product line for experiment optimization and large volume EP. However, compared to commercial equipment, a flow-type EP microchip overcomes the limit in the amount of target cells and the potential risk of using high voltage, which are the two drawbacks in current EP technology (Andersson and Berg 2003). A review on single-cell EP has been presented for the investigation of cell-to-cell variations in a population and to manipulate as well as investigate the intracellular chemistry of a cell (Olofsson *et al.* 2003 and Fox *et al.* 2006). Huang and Rubinsky (1999, 2001 and 2003) have presented the first microfabricated devices, developed to control EP process at the single cell level. In a typical process,

individual cells flow through the inlet tube to the top chamber between the top and the middle layers. Individual cells can be captured in the hole and thus oriented in the electrical circuit between two electrodes of the chip. Experiments showed the capability of introducing desirable macromolecules into specific individual cells with micro-electroporation chips. In addition, Khine *et al.* (2005) developed a polymeric chip that can selectively immobilize and locally electroporate single cells.

One aim was to handle cells in EP microchip channels precisely to achieve high effectiveness in the genetic manipulation of cells (Lin and Huang 2001, Lin *et al.* 2003 and 2004). Furthermore, Kim *et al.* (2007) has developed a multi-channel EP microchip made of polydimethylsiloxane and glass for gene transfection in mammalian cells. Micro-electroporation devices were also employed for cell lysis prior to subcellular analysis (Lu *et al.* 2005).

### 1.1.3 Electroporabilization

#### *Electroporabilization in lipid bilayer membranes*

The lipid bilayer membrane (LBM) of cells is composed of lipid molecules, mainly phospholipids. The phosphate group is usually esterified with a nitrogen-containing alcohol. Two long hydrophobic fatty acid chains and a single phosphate group esterified with an ethanolamine residue are linked to a central glycerol molecule. The phosphate and amino-group of the ethanolamine residue represent the hydrophilic parts of the molecule. Normally, the hydrophilic polar heads are oriented toward water, whereas the hydrophobic groups (non-polar) toward oil (Glaser 2001). Many researchers have investigated the electroporabilization in LBM. The similarity of the phenomenological cell and lipid bilayer membrane breakdown indicated that pores, developed during the electrical breakdown of biological membranes, arise in their lipid matrices (Chernomordik *et al.* 1987). Membrane proteins affect the EP of the LBM by changing its mechanical properties. Glaser *et al.* (1988) have studied the mechanism of reversible electric breakdown of lipid membranes. They showed that the conductivity of the pores

depends on membrane voltage and the type of this dependence changed with the radius of the pore. Weaver and Chizmadzhev (1996) showed that their transient aqueous pore models could account for: (1) key features of mechanical instability (irreversible consequence of EP) of planar lipid bilayers at elevated voltages, (2) dramatic reversible electrical behavior of certain planar membranes and of cell membranes and (3) some features of molecular transport. However, at subcritical electric fields the average pore size was stationary and very small. At supercritical field strengths, the pore radius increased and the membrane ruptured after reaching a critical pore size (Sugar and Neumann 1984).

Tien and Ottova (2003) have reviewed that a transmembrane potential of the order of 0.5 to 1 V, promoted pore formation in both experimental LBM (planar LBM and liposomes) and natural membranes (see also Weaver 2000). The breakdown voltage of the artificial LBM also depends on the constituent of membranes, temperature and electric pulse (Benz *et al.* 1979, Freemann *et al.* 1994, Needham and Hochmuth 1989, Tsong 1992 and Winterhalter *et al.* 1996). Moreover, the breakdown voltage increased with increasing slope of the linear rising signal of voltage pulse (Kramar *et al.* 2007).

### ***Electropermeabilization of cells and tissues***

Cells suspended in a liquid can be modeled as a structure consisting of a non-conducting membrane with aqueous solutions on both sides. Exposure to an electric field leads to charge separation in the membrane similar to the charge separation in the dielectric layers of an electrical capacitor. This results in a transmembrane potential difference (Hofmann 1989). High intensity and short duration electric fields can result in membrane breakdown. This effect can be associated with electropermeabilization of the membrane (Zimmermann 1996). Electropermeabilization (also referred to EP or dielectric breakdown and sometimes “reversible electrical breakdown”) is important for the introduction of extracellular molecules that do not penetrate cell membranes under normal conditions. Membrane pore formation was previously discussed since the late 1970s (Kinosita and Tsong 1977). Later, many publications showed that small molecules,

such as dyes, ions or drugs can pass the electric field-induced membrane pores (Chang *et al.* 1992, Neumann *et al.* 1989 and Zimmermann and Neil 1996).

Electropermeabilization can be visualized by staining the cell membrane with a voltage-sensitive fluorescence dye (Gabriel and Teissié 1999, Hibino *et al.* 1991 and 1993 and Marszalek *et al.* 1990). The membrane structure of electropermeabilized red blood cells revealed by rapid freezing electron microscopy was related to the creation of volcano-shaped membrane pores (Chang *et al.* 1992). Electropermeabilization of cells depends on several electric parameters, e.g. field strength, pulse duration, number of pulses (Benz and Zimmermann 1981, Lebar and Miklavcic 2001, Müller *et al.* 2001, Puc *et al.* 2003, Rols and Teissié 1990, 1998, Teissié and Ramos 1998, Wolf *et al.* 1994 and Zimmermann and Benz 1980), pulse shape (Fologea *et al.* 1998, Konik *et al.* 2001 and 2003) and field properties such as a linear or rotating orientations (Gimsa *et al.* 1988a). Additionally, cell size, shape and orientation, medium conductivity and temperature are of great importance (Coster and Zimmermann 1975, Marszalek *et al.* 1990, Valic *et al.* 2003 and Zimmermann and Benz 1980). However, increasing electric field strength may cause conformational changes in the membrane structure, resulting in lysis and cell death (Sale and Hamilton 1967 and 1968).

Furthermore, at low intensity of AC-fields, the electroconformational coupling (ECC) model was used to interpret the result of DNA transfection (Tsong 1990 and Xie and Tsong 1990). The ECC model is a viable concept for understanding the electric activation of membranous ATPases, e.g. Na<sup>+</sup>-K<sup>+</sup>-ATPase (Chen *et al.* 1998, Markin and Tsong 1991, Xie *et al.* 1994 and 1997). Nevertheless, also other effects of pulsed electric fields on the permeability of a cell membrane can occur. The examples for these effects, e.g. colloid osmotic lysis of cells (Kinosita and Tsong 1977 and Sale and Hamilton 1968), electrotransfection of DNA (Xie *et al.* 1990, Xie and Tsong, 1990 and 1992) have been studied.

The effect of membrane breakdown can be applied for cell hybridization, production of monoclonal antibodies, cell transfection and other cell technology applications. More recent developments apply electric membrane poration of tissues for



electrochemotherapy (cancer treatment), gene therapy and transdermal drug delivery (Canatella *et al.* 2004, Cukjati *et al.* 2007, Davalos *et al.* 2005, Gothelf *et al.* 2003, Hofmann *et al.* 1999, Miklavcic *et al.* 2006, Mir and Orłowski 1999, Neumann *et al.* 1998, Pliquett 2003, Rubinsky 2007, Schoenbach *et al.* 2002, Smith *et al.* 2004 and Weaver 2000).

### 1.1.4 Electrofusion

The experimental procedures of electrofusion are very similar to EP, except that the cells to be fused must be brought into contact first. This cell contact can be accomplished by (Chang *et al.* 1992, Neumann *et al.* 1989 and Zimmermann and Neil 1996):

- (1) Natural membrane contact, e.g. the use of cells grown to confluence in monolayer cultures, on microcarriers, or on porous membranes
- (2) Cell pellets or chemical treatment, e.g. cells kept at high density or cells pelleted by sedimentation or centrifugation and chemical additives such as polyethylene glycol (PEG) and dextran, etc.
- (3) Physical force such as:
  - Mechanically induced contact
  - Ultrasonically and magnetically mediated cell alignment
  - Electrically induced cell-cell contact, e.g. dielectrophoresis (in which cells lined up in chains by applying a low-intensity, high frequency, non-uniform and AC-fields).

When two cells contact each other during electric pulse application or during a short time after the pulse, the points of induced membrane instability may interact, leading to a fusion of the lipid phases of both cells. Subsequently, osmotically governed process of fusion of the cytoplasm may follow. This process is called “electrofusion” (Glaser 2001). Electrofusion can be applied for biotechnology, plant breeding, cloning of embryos, hybridoma technology, etc. In recent years, electrofusion has been applied for immunotherapy (Katrina *et al.* 2004, Kjaergaard *et al.* 2003, Trefzer and Walden 2003 and Weise *et al.* 2004).

### 1.1.5 Cell movement in AC-fields

Cell movements in AC-fields or AC-electrokinetics of cells are also techniques for cell manipulations. AC-electrokinetics effects for dielectric characterization and manipulation have been studied for many years. Different AC-electrokinetics effects occur due to the interaction of induced dipoles with electric fields. Examples for cell movements in AC-fields are (Gimsa 2002, Glaser 2001, Hughes 2000, Jones 1995, Pohl 1978 and Zimmermann and Neil 1996):

- Dielectrophoresis (DP)
- Levitation and trapping
- Attraction
- Electrodeformation (ED)
- Electrorotation (ER)
- Electroorientation (EO)
- Traveling-wave dielectrophoresis (TWD)

The DP method is based on the ability of an inhomogeneous electric field to induce a dipole moment on polarizable objects, which leads to a net force on the object vice versa. Positive values of DP indicate that cells or particles can be attracted to high field area. The latter effect caused pearl chain formation along the field lines. The negative values correspond to compression or repulsion from high field areas in ED and DP. Negative DP can also be used to levitate cells or particles as well as for trapping of cells (Fuhr *et al.* 1992, Gimsa 2002, Jones 1995, Pohl 1978 and Zimmermann and Neil 1996).

ER is a common approach to characterize the dielectric properties of individual biological cells and particles by microscopic observation of their frequency dependent rotation speed (Gimsa 2002, Gimsa *et al.* 1996, Gimsa *et al.* 1991b and Jones 1995). Rotating fields of frequencies ranging from Hz to GHz are commonly generated by four microelectrodes energized by four potentials that are progressively phase shifted by 90°. The frequency spectrum of rotation at constant field strength can be analyzed to obtain the dielectric properties of the objects, e.g. cells, cell organelles or viruses. The direction

---

of cell rotation in a rotating field depends on field frequency. At low frequency, the impedance of the membrane is significantly higher than the resistance of the external and internal media. The interaction of the induced dipole moment and the external field produces the torque acting on the cell. This torque pushes the cell in a direction opposite to the external field rotation. Cells show anti-field rotation. For high frequency, the membrane is short-circuited. Because of its capacity, the current flows preferentially through the cell. The resistance of the membrane becomes negligible and the conductivity of the cell becomes essentially equal to the cytoplasmic conductivity. Thus, co-field rotation will occur. Co-field and anti-field phenomena are also dependent on the conductivity of the suspending solution (Gimsa *et al.* 1991b and Zimmermann and Neil 1996).

When a non-spherical particle is suspended in an electric field, orientation of particles can be observed. The particle orientation will vary according to the field frequency since each axis has a different dispersion frequency. However, the orientation torque does not depend on either dielectric or ohmic loss, while rotational torque requires it (Jones 1995).

The TWD is another method for cell manipulation in electric field. TWD is a linear motion analogue to ER using electrode tracks with a phase difference of  $90^\circ$  between consecutive electrodes (Fuhr *et al.* 1991). The velocity of translational motion is proportional to the imaginary part of the induced dipole moment and therefore related to the ER effect. The TWD method is advantageous for motion control and separation of particles or cells in microfluidic systems combined with fluidic pumps (Cui and Morgan 2000, Fuhr *et al.* 1994, Huang *et al.* 1993 and Morgan *et al.* 1997). The DP levitation force (negative DP) is proportional to the real component (Fuhr *et al.* 1991, Huang *et al.* 1993 and Morgan *et al.* 1997, 2001 and Pethig *et al.* 2003).

Recent advances in AC-electrokinetic techniques for cell manipulations such as DP and ER methods have been applied for nanotechnology (Dimaki and Boggild 2004, Hughes 2000 and Tuukkanen *et al.* 2005).

## 1.2 Aims

The aim of this work is to consider the characterization and manipulation of ellipsoidal cells in fluidic micro-electrode systems. Numerical simulation, theoretical analysis and experiment are considered. The electric field distributions in planar electrode chips were analyzed using finite element programs. Simplified equations for the transmembrane potential induced in ellipsoidal cells of rotational symmetry and dielectrophoretic force were analyzed. Furthermore, the effects of cell orientation and electric field frequency on the transmembrane potential induced in cells of an arbitrarily ellipsoidal shape have been a main focus of this work. The thesis is organized in the following chapters:

- **Chapter 1** gives the introduction.
- **Chapter 2** shows numerical simulations of electric field distributions in planar electrode chip chambers using finite element programs. The distribution of a sinusoidally rotating electric field was calculated for a two-dimensional model. Based on these calculations, torques have been compared acting on a spherical object at the center of chambers of different electrode designs. Furthermore, the electric field distribution in EP chip chambers for the three-dimensional model was analyzed. Since this work has already been published, please see appendices A and B for more details.
- **Chapter 3** presents the materials and methods of the experimental part. The electrode chips for EP experiments were designed. Cells and solutions have been prepared.
- **Chapter 4** presents the simplified equations for the transmembrane potential induced in ellipsoidal cells of rotational symmetry. However, the details of these simplifications have been shown in appendix C. The effects of electric field and cell orientation on the  $\Delta\phi$  induced in the arbitrarily ellipsoidal cells were also analyzed. Details are given in a full manuscript (appendix D). The theoretical results were compared to electropermeabilization experiments with chicken red blood cells (CRBCs). Electropermeabilization and cell lysis of CRBCs in linear AC-fields and rotating fields were also compared. Some experimental results have been presented in appendix D.

- **Chapter 5** shows the simplified equations for dielectrophoretic force of spheroidal cells.
- **Chapter 6** gives the conclusions of this work.

However, all papers were published with the help from my co-authors. They taught me how to use the finite element programs, some graphics software and Maple program. Moreover, we had very fruitful discussions and finally they help me with the language.

## Chapter 2

# Numerical electric field simulations in microfluidic systems

## 2.1 Optimizing the electrode shape for four-electrode electrorotation chips

In this study, the sinusoidally rotating electric fields in a two-dimensional chip-model for various electrode shapes have been compared using the finite element program QuickField (Tera Analysis Ltd., Denmark, <http://www.quickfield.com/free.htm>) and FEMLAB 3.1 (COMSOL AB, Stockholm, Sweden). Correction factors were calculated for the electric field strength and the object-torque. Based on these calculations, torques acting on a spherical object at the center and at distant sites within the electrode chamber have been analyzed. The site dependent deviation of the torque from the torque in the center of the chip has been compared for various electrode designs in order to find an optimal chip design. Please see appendices A and B for more details.

Starting from the QuickField finite element program, the limitation of this program was found. This program could not simulate the complex shape of electrodes. Moreover, the analytical data were not fine enough (Maswiwat *et al.* 2007a; appendix B), whereas their smooth curves analyzed using FEMLAB 3.1 finite element program were found (Maswiwat *et al.* 2006; appendix A). Accordingly, the results analyzed by the FEMLAB 3.1 program were selected for optimizing the electrode shape for four-electrode rotation chambers. However, the results from both programs show that the field properties depend very much on the location within the chamber and electrode design. The field vectors in the central regions are generally homogeneous. In the vicinity of the electrodes the field is highly inhomogeneous (figure 2.1). Figure 2.1 shows the electric

field strength distribution in the  $x$ - $y$  plane of the electrode chambers at  $0^\circ$ - and  $45^\circ$ -phase (see appendix A for details). The torque deviation inside the measuring volume of the chamber is the most important characteristics for the usability of a rotation chamber. In a plane chip this volume is confined to an area with comparable torques. The circular areas were defined from a torque deviation up to 10% with respect to the torque in the center, resulting in the specific radius distance ( $S_{10\%}$ ). The radius of the experimentally usable area was calculated from the minimum of the  $S_{10\%}$ -distances (table 2.1). Amongst all electrodes a maximum area of constant torque is found for the design P2. In this design the percentage of usable area is at least 40.11% (table 2.1 and compare to appendix B).

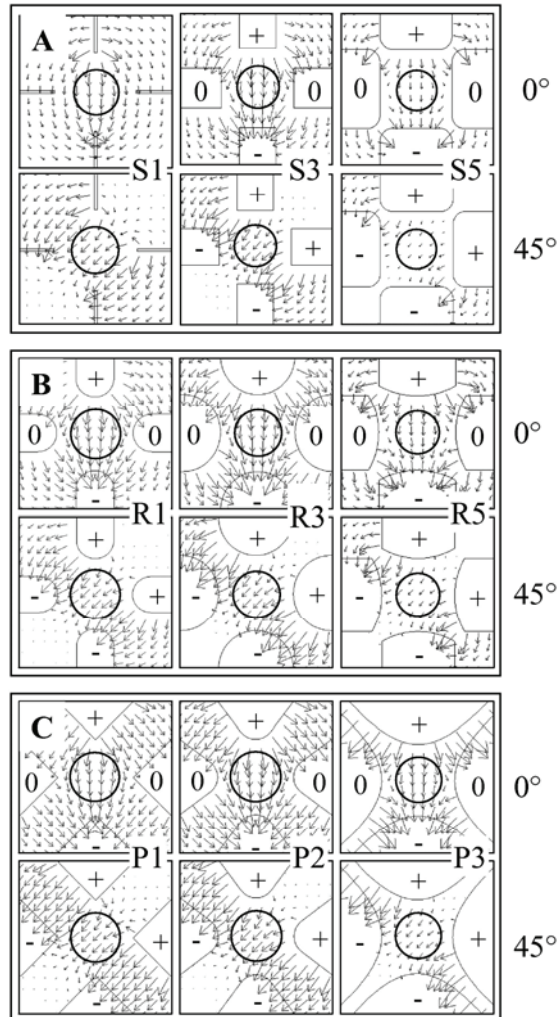


**Figure 2.1** Electric field strength distribution in the  $x$ - $y$  plane of the electrode chambers at  $0^\circ$ - and  $45^\circ$ -phase, respectively using the FEMLAB 3.1 finite element program. (A) squared electrodes S1, S3, S5. (B) rounded-tip electrode R1, R3, R5. (C) pointed pyramidal, rounded tip pyramidal and parabolic electrodes P1, P2, P3, respectively. The arrows are electric field strength vectors.

For a chip chamber the area with comparable torques limits the useable area or the size of larger cells. In all cases  $S_{10\%}$  was at least  $75 \mu\text{m}$  (table 2.1).



**Table 2.1** Torque correction factor  $r^2$  and distance from the center for a torque deviation of 10% ( $S_{10\%}$ ) for different electrode designs. The last column presents the relative area with respect to the inner electrode circle with a radius of 150  $\mu\text{m}$  inside which the torque deviation is below 10%. The circle areas were determined from the minima of  $S_{10\%}$ -values along the connecting lines and the diagonals marked by an asterisk (see figure 2.1).

Designs	$r^2$	Width $D$ ( $\mu\text{m}$ )	Radius $R$ ( $\mu\text{m}$ )	$S_{10\%}$ in $\mu\text{m}$		
				Connecting lines	Diagonals	% of usable area
S1	0.44	10	-	95	84*	31.36
S2	0.60	75	-	104	88*	34.42
S3	0.68	150	-	79*	114	27.73
S4	0.70	240	-	75*	171	25
S5	0.70	300	-	75*	167	25
R1	0.59	150	75	103	93*	38.44
R2	0.62	240	120	91*	100	36.80
R3	0.63	300	150	88*	104	34.42
R4	0.65	300	240	83*	114	30.62
R5	0.66	300	300	82*	119	29.88
P1	0.50	-	-	147	93*	38.44
<b>P2</b>	<b>0.59</b>	-	-	<b>103</b>	<b>95*</b>	<b>40.11</b>
P3	0.64	-	-	86*	110	32.87

Please note that the percentage of usable area at  $S_{10\%}$  is calculated by:

$$\frac{\text{Circle area of the minimum of } S_{10\%}}{\text{Circle area of the inner electrode circle with a radius of } 150 \mu\text{m}} \times 100$$

## 2.2 Electric field distribution in three-dimensional electroporation and electrorotation chambers

To address the EP experiments, the three-dimensional electric field distributions in the experimental chambers were studied. The COMSOL 3.3A Multiphysics finite element program (COMSOL AB, Stockholm, Sweden) was used assuming driving potentials of +/-10 V. The electric field strength distributions in the EP chip (figure 2.2(A)) and ER chip chambers (figure 2.2(B)) were compared. The arrowhead and the length of arrow show the direction and the magnitude of electric field strength, respectively. For EP chip the inhomogeneous fields was found at the edges of electrodes (figure 2.2(A)). The field vectors in between two-plane parallel electrodes are generally homogeneous. Highly inhomogeneous fields are observed in the vicinity of the electrodes of the ER chip chamber (figure 2.2(B)). The field vectors in the central regions are homogeneous.

The electric field strengths in EP chip chamber were calculated as shown in appendix D. The results show that the electric field strengths near the vicinity of the electrodes and close to the chamber bottom are stronger than in the center. However, at positions above the chamber bottom the electric field strength becomes lower (see appendix D for details).

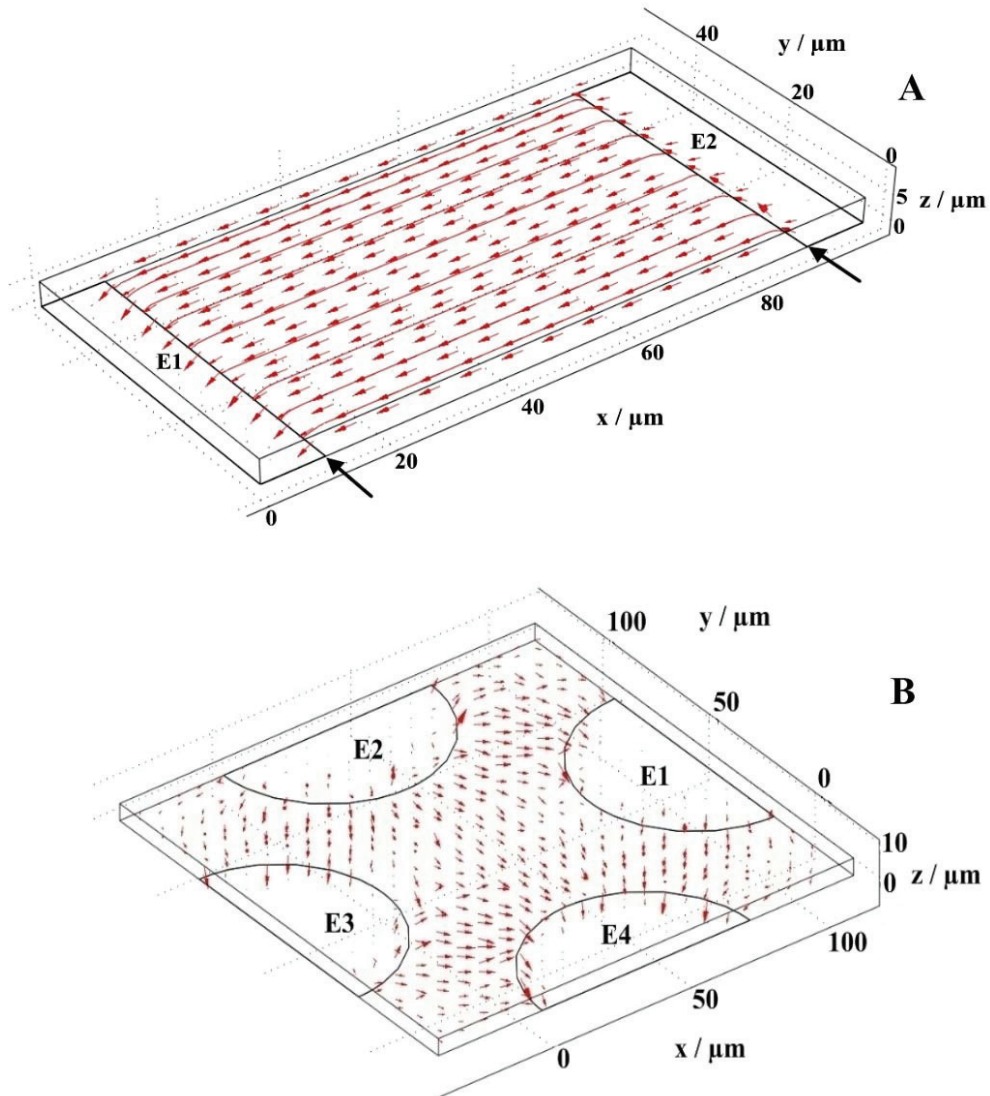


**Figure 2.2** Three-dimensional electric field distributions in EP and ER chip chambers calculated by the COMSOL 3.3 A finite element program. (A) the electric field lines between two plane-parallel electrodes E1 and E2. The distance between electrodes is  $80\ \mu\text{m}$ . The width, the length and the thickness of each electrode are  $10\ \mu\text{m}$ ,  $50\ \mu\text{m}$  and  $100\ \text{nm}$ , respectively. (B) the electric field lines between rounded tip four-electrode. E1, E2, E3 and E4 were progressively phase-shifted by  $90^\circ$ . The radius of electrode tip, the distance between tip to tip and the thickness of each electrode are  $37.5\ \mu\text{m}$ ,  $75\ \mu\text{m}$  and  $100\ \text{nm}$ , respectively. The aqueous measuring solution with a height of  $5\ \mu\text{m}$  was assumed for both chip chambers.

# Chapter 3

## Materials and Methods

### 3.1 Microfluidic chips design

EP and ER chips for electroporation experiments as well as the chip for TWD study were designed using Micrografx Designer 9.0 program (iGrafX, a division of Corel-Corel GmbH, Unterschleißheim, Germany).

#### 3.1.1 Electroporation chip

A glass EP chip was designed for observation of the electroporation of CRBCs in square-wave AC-fields. This chip allowed for five different inter-electrode gap widths of 80  $\mu\text{m}$ , 100  $\mu\text{m}$ , 150  $\mu\text{m}$ , 300  $\mu\text{m}$  and 450  $\mu\text{m}$  (figure 3.1) generating five electric field strengths for the same supply voltage. Only the three shorter distances (80  $\mu\text{m}$ , 100  $\mu\text{m}$  and 150  $\mu\text{m}$ ) were used for CRBCs. Bigger cells can be observed with the larger distances (300  $\mu\text{m}$  and 450  $\mu\text{m}$ ). Temperature sensors were designed for the measurement of temperature changes in the chamber. A photoresist structure forms the side walls limiting the sample volume (figure 3.1).

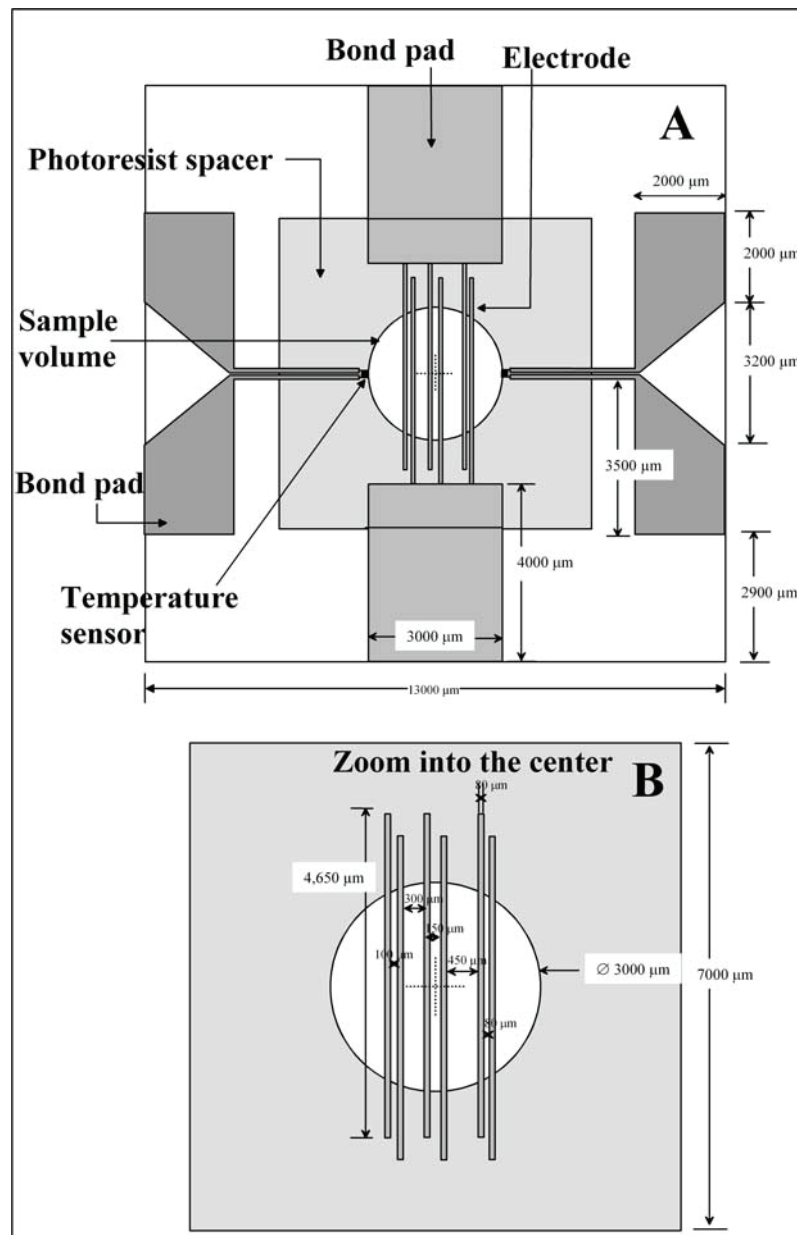


**Figure 3.1** The electroporation chip design. (A) electrode chip design (13x13 mm<sup>2</sup>). The meander-structure of temperature sensor was connected to the sample volume. A photoresist structure forms the side walls limiting the sample volume which diameter is 3 mm. (B) zoom of the plane-parallel electrodes. The width and the length of each electrode were kept constant at 80  $\mu\text{m}$  and 4.65 mm, respectively.

### 3.1.2 Electroration chip

The ER chip with four platinum rounded-tip electrodes was designed for investigation of electropermeabilization in square-wave rotating electric fields (figure 3.2). Two electrode pairs simultaneously generate the two field components (see appendices A and B).

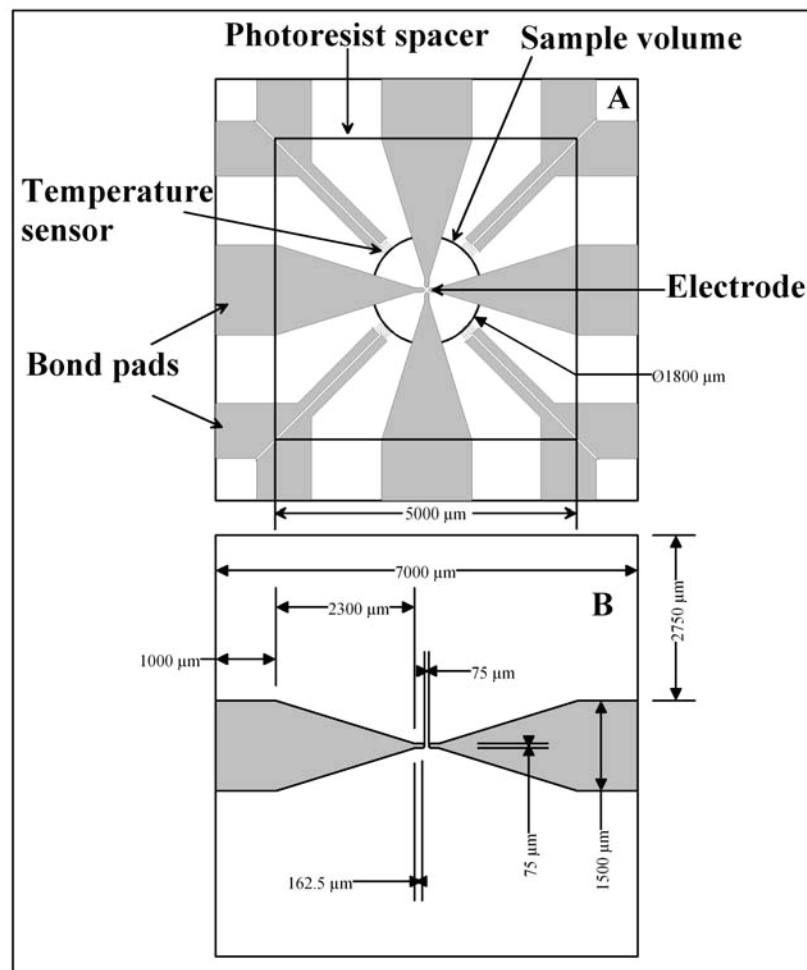


**Figure 3.2** Electroration chip design. (A) the electrode chip design ( $7 \times 7 \text{ mm}^2$ ). The temperature sensor was a meander-structure connected to the sample volume. A photoresist structure forms the side walls limiting the sample volume to a circular diameter of 1.8 mm. (B) measures of the electrodes. The radius of each electrode tip was  $37.5 \text{ }\mu\text{m}$ . The distance between two opposing electrodes and the width of each electrode tip were  $75 \text{ }\mu\text{m}$ .

### 3.1.3 Traveling-wave chip

To investigate the TWD of cells or particles, a chip with eight parallel-electrodes was designed. The traveling-wave electric fields were generated by supplying adjacent electrodes with  $90^\circ$  phase-shifted voltages.

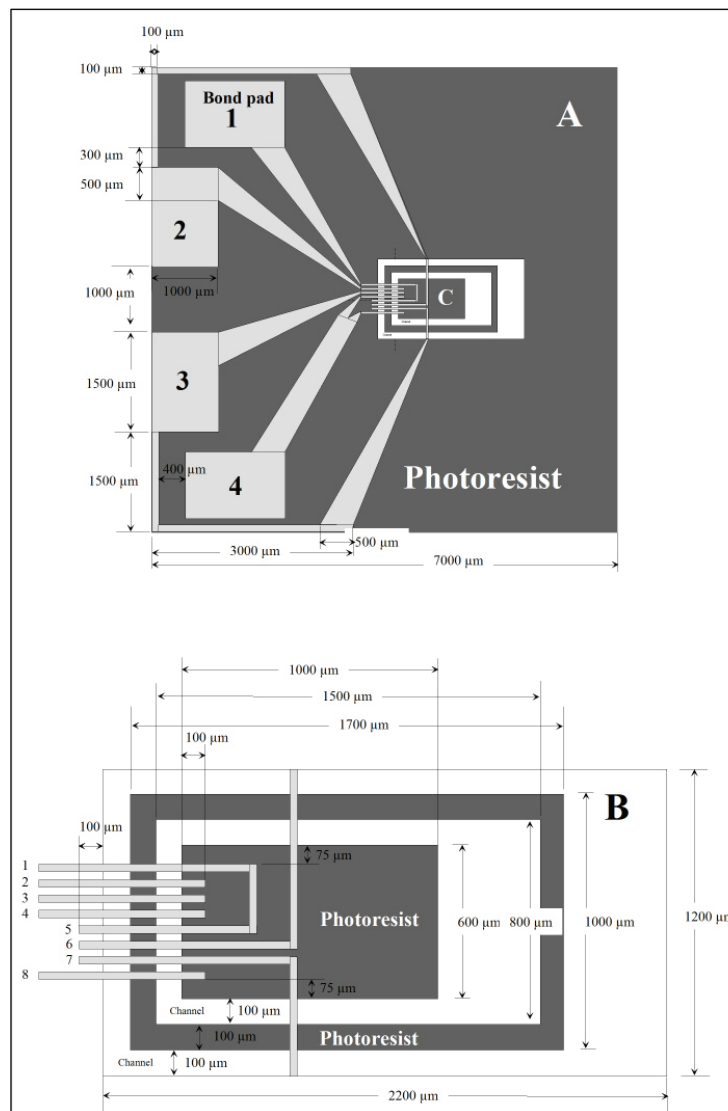


**Figure 3.3** Traveling-wave chip design. (A) the electrode chip design ( $7 \times 7 \text{ mm}^2$ ). A photoresist structure forms two channels with a width of  $100 \mu\text{m}$ . (B) zoom of eight parallel-electrodes. The electrode width and the inter-electrode gap were  $30 \mu\text{m}$ .

### 3.1.4 Chip carriers

All chip designs were fabricated by GeSiM GmbH (Grosserkmannsdorf, Germany, [www.gesim.de](http://www.gesim.de)). The thickness of each platinum electrode and photoresist was 100 nm and 60  $\mu\text{m}$ , respectively. Double layered circuit board material was used for the chip carriers. Chip carriers were designed using Eagle Layout Editor 4.16 program (CadSoft Computer, Inc., Florida, USA). Chip and chip carrier for electropermeabilization in linear AC-fields are shown in appendix D. Figures 3.4 and 3.5 show the chip and chip carrier for electropermeabilization in rotating fields and TWD studies, respectively.

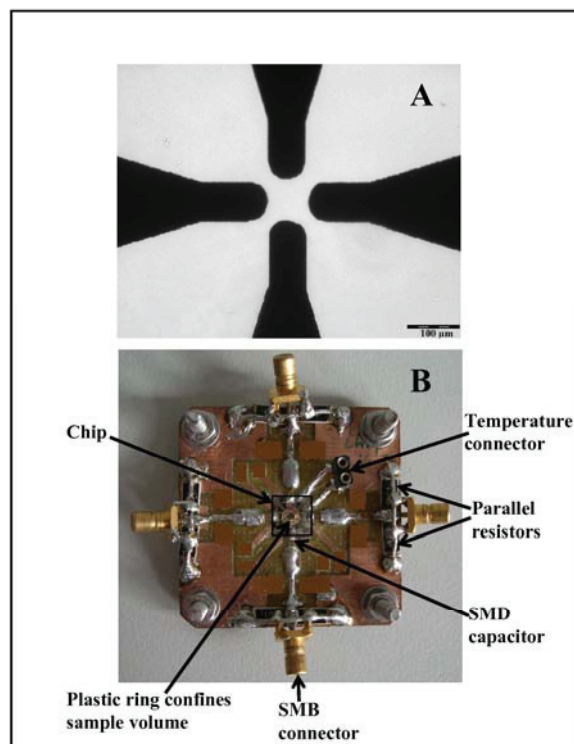


**Figure 3.4** Chip and chip carrier for electropermeabilization in rotating electric fields. (A) four platinum rounded-tip electrode chip. (B) chip carrier. The bond pad of each electrode was connected to SMD capacitors (0.1  $\mu\text{F}$ ), two parallel 100  $\Omega$  resistors and SMB connectors (50  $\Omega$  of impedance). The plastic ring in the center of the chamber was glued to the photoresist to limit the sample volume (5  $\mu\text{l}$ ). The chamber was sealed by a cover slip during measurements.



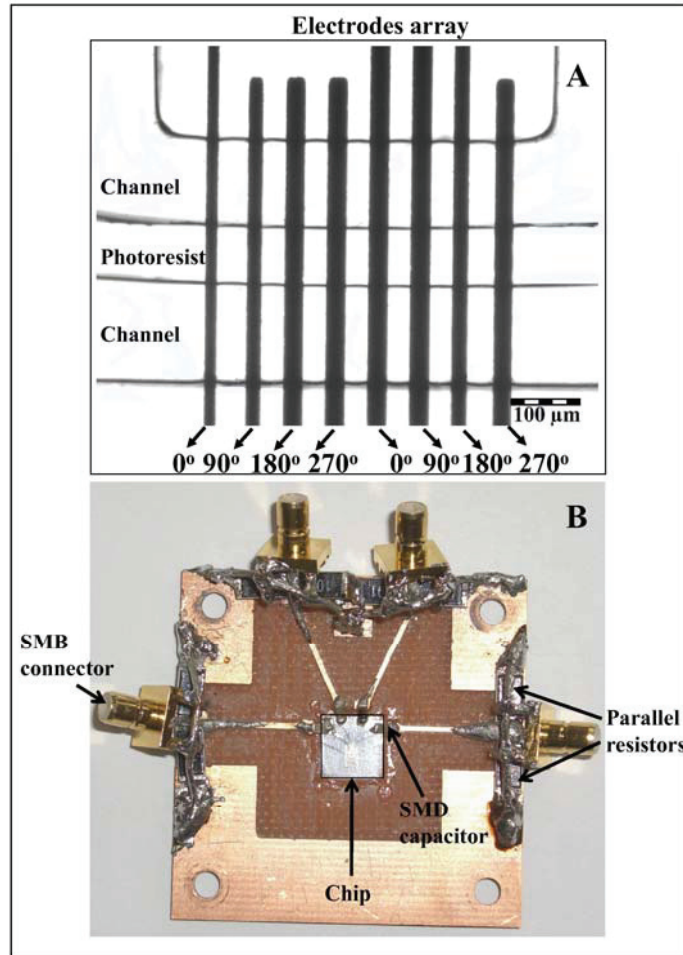


**Figure 3.5** Chip and chip carrier for travelling-wave dielectrophoresis. (A) the platinum electrode chip with eight parallel-electrodes. The photoresist forms two channels. (B) chip carrier. The bond pad of each electrode was connected to SMD capacitors ( $0.1 \mu\text{F}$ ), two parallel  $100 \Omega$  resistors and SMB connectors ( $50 \Omega$  of impedance).

However, the traveling-wave chip (figure 3.5(A)) fabricated by GeSiM GmbH did not fully correspond to the original design (figure 3.3). The width and the inter-electrode gap were not equally  $30 \mu\text{m}$  resulting in an inhomogeneous electric field in between the inter-electrode gap. Moreover, the photoresist was easily damaged. Accordingly, the TWD study has been canceled.

### 3.2 Electroporation instrumentation

Block diagram of instruments and chip chamber for electroporation in linear AC-fields is shown in figure 3.6 (see appendix D for details). The same setup can also be used for electroporation in rotating fields. The method of observing PI-permeabilization by fluorescence is presented in appendix D. The electric field strength ( $E$ ) generated in between a pair of parallel electrodes by a square-wave AC-pulse with a key ratio of 1:1 is also described in appendix D. In the case of cell permeabilization in rotating fields, the electric field strength in the central region depends on the electrodes shape (Chapter 2). Accordingly, the field correction factor ( $r = 0.79$ ) obtained from electrode design R3 (table 2.1) was used for field calculations. The equation of  $E$  in the chip chamber becomes  $E = 0.79V_{ss}/d$ , where  $V_{ss}$  and  $d$  stand for the voltage difference between the electrodes and the distance between the two opposite electrodes (see appendix D for details).

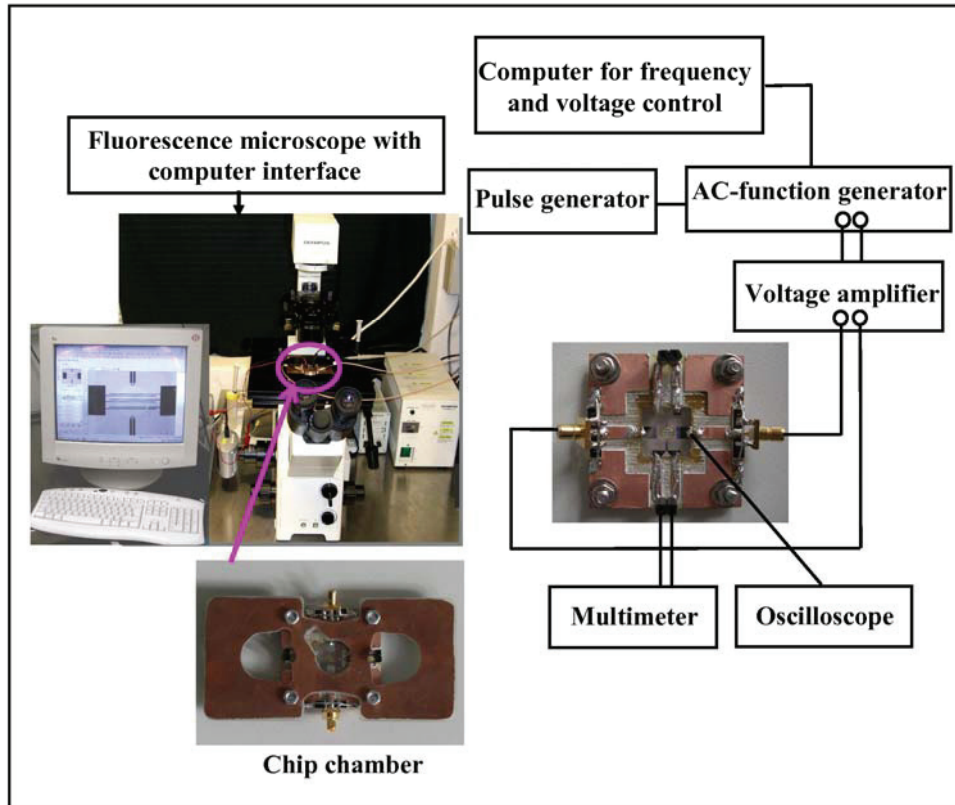


**Figure 3.6** Block diagram of instruments and chip chamber for electroporation experiments. The chip chamber was connected to the voltage amplifier, AC function generator and pulse generator. The AC function generator was controlled by a computer program (courtesy of Derk Wachner). The waveform, amplitude, and frequency of square-wave AC-fields across two electrodes were monitored directly with an oscilloscope. The temperature sensor was connected to a multimeter for resistance measurements. Electroporation of cells was observed under the fluorescence microscope. The photos were monitored and recorded by a computer interface.

### **3.3 Temperature sensor calibration**

A temperature sensor was used for investigating the temperature changes in the chamber. However, the temperature cannot be directly measured. The temperature on the chip was obtained from a temperature sensor calibration. For calibration of the temperature sensor, the resistance of sensor and temperature on the chip were measured using a multimeter (model 2000, Keithley Instruments Inc., USA) and a digital thermometer (Omega HH506R, Deckenpfronn, Germany), respectively. The system was controlled in an oven (Mettler UM400, Mettler GmbH, Schwabach, Germany) in the temperatures range of 25 °C - 60 °C. For lower temperatures, the system was transferred to a common refrigerator. The calibration curves of resistances and temperatures on the chips were plotted using the SigmaPlot 9.0 program (Systat Software GmbH, Germany) shown in Chapter 4.

### **3.4 Cells and solutions**

CRBCs were obtained from BfR (Bundesinstitut für Risikobewertung, Berlin, Germany). Fresh blood samples were taken from the wing vein of Italian cocks and preserved in Alsever's solution as an anticoagulant. The concentration of CRBCs in this solution was measured by centrifugation at 10,000×g (speed = 10,500 rpm) for 5 minutes with a centrifuge (Sigma 1-5, Fisher Bioblock Scientific, Osterode, Germany). The hematocrit of CRBCs was found at  $19.28 \pm 3.62$  %. Please note that fresh blood should be treated gently and also not squirted through thin needles to avoid haemolysis (Grimes 2002).

### 3.4.1 Alsever's solution

#### *Materials*

- |                                      |         |
|--------------------------------------|---------|
| 1. Dextrose (glucose)                | 18.66 g |
| 2. NaCl                              | 3.18 g  |
| 3. tri-Na-citrate-2-hydrate          | 8.0 g   |
| 4. Filled up with distilled water to | 1 l     |

Fresh blood was suspended in this solution with a dilution ratio of 1:1 at pH 6.1.

### 3.4.2 Phosphate buffer solution

Phosphate buffer (PB) solution was prepared from the mixture of two solutions shown below.

#### *Solutions*

- |   |                               |                           |       |
|---|-------------------------------|---------------------------|-------|
| 1. Sodium di-hydrogen phosphate monohydrate ( $\text{NaH}_2\text{PO}_4\text{H}_2\text{O}$ , Karl Roth GmbH & Co.KG, Germany)      |                               |                           |       |
|   | Mw 137.99 g mol <sup>-1</sup> | 8.0034 g l <sup>-1</sup>  | 58 mM |
| 2. Di-sodium hydrogen phosphate dodecahydrate ( $\text{Na}_2\text{HPO}_4 12\text{H}_2\text{O}$ , Karl Roth GmbH & Co.KG, Germany) |                               |                           |       |
|   | Mw 358.14 g mol <sup>-1</sup> | 20.7721 g l <sup>-1</sup> | 58 mM |

The pH values were measured by a microprocessor pH meter (pH 211, Hanna instruments, Italy). The pH values of both solutions were  $3.66 \pm 0.20$  and  $8.72 \pm 0.15$ , respectively measured at a temperature of  $22 \pm 1.5$  °C. Both solutions were mixed to adjust the final pH to 6.8.

### 3.4.3 Measuring solution

For electropermeabilization experiment, CRBCs were suspended in the measuring solution. This solution was a mixture of sucrose and NaCl solutions. Both solutions had an osmolarity of 300 mOsm and contained 1 mM PB solution at pH 6.8 (Lippert and Gimsa 2002, see below). The solutions were mixed to adjust the medium conductivity to  $0.12 \text{ S m}^{-1}$ . The solution conductivity was measured with a conductometer (inoLab Cond Level 1, WTW GmbH, Weilheim, Germany) in the temperature compensation mode ( $20^\circ\text{C}$ ).

#### *Solutions*

1. Sodium chloride (NaCl, Karl Roth GmbH & Co.KG, Germany)

M  $58.44 \text{ g mol}^{-1}$        $9.175 \text{ g l}^{-1}$       157 mM (300 mOsm)

2. Sucrose ( $\text{C}_6\text{H}_{12}\text{O}_{11}$ , Karl Roth GmbH & Co.KG, Germany)

M  $342.3 \text{ g mol}^{-1}$        $90.07 \text{ g l}^{-1}$       263 mM (300 mOsm)

1 mM PB solution, pH 6.8 was added to both solutions.

## Chapter 4

# Transmembrane potential induced in ellipsoidal cells

### 4.1 Simplified equations for the transmembrane potential induced in ellipsoidal cells of rotational symmetry

#### 4.1.1 Introduction

New simplified analytical equations for the influential radii, i.e. the geometry-factors  $1/(1-n_a)$  that avoid the complicated description by the full expressions for the depolarizing factors  $n_a$  and  $n_c$  (Gimsa and Wachner 1999) are presented. These equations apply for the  $\Delta\phi$  induced in oblate and prolate cells (or tissue bodies such as abscesses, bruises etc.) by homogeneous DC or AC fields. In practice, there will always be errors arising from the measurement of the geometric cell parameters, as well as deviations of the cell shapes from an idealized spheroidal shape. In any case, new approximations will be superior than the assumption of a spherical shape with a mean or effective radius and the experimental errors will be larger than the discrepancies introduced by these simplifications (see appendix C for details). Starting from the simplified equations of influential radii ( $a_{\text{infl}}$  and  $c_{\text{infl}}$  in appendix C),  $\Delta\phi_a$  and  $\Delta\phi_c$  for spheroids will be further simplified at high frequencies in following.

### 4.1.2 Simplification of $\Delta\phi$ for spheroids at high frequencies

At high frequencies the  $\Delta\phi$  decreases since frequency-independent ionic conductivities are superseded by capacitive currents (figure 4.1). Please compare to the full RC-lump model in appendix D and see also Gimsa and Wachner (1999 and 2001a). This model contains three different media, internal, membrane layer and external designated by the indices  $i$ ,  $m$  and  $e$  respectively. Three elements of equal cross-sectional area ( $A$ ) are required. The impedance  $Z^*$  of each element is given by:

$$Z^* = \frac{-j}{\omega C} \quad (4.1)$$

$j$ ,  $\omega$  and  $C$  stand for the imaginary unit ( $-1^{0.5}$ ), circular frequency and capacitance of the considered medium, respectively.

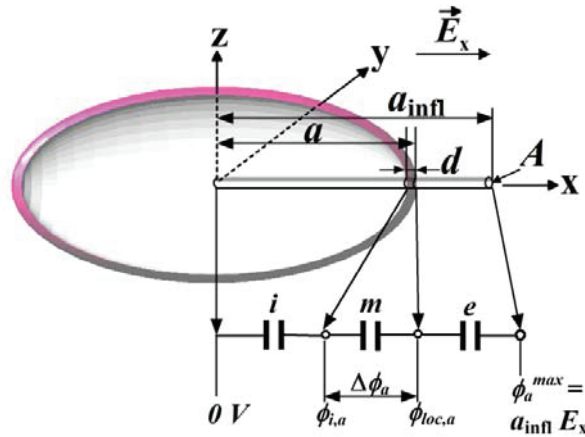


**Figure 4.1** Sketch of three finite elements of capacitance lump model for high frequencies.  $C_i$ ,  $C_m$  and  $C_e$  stand for the capacitance of cytoplasm, membrane and external medium, respectively.  $A$ ,  $d$ ,  $a$  and  $a_{infl}$  stand for cross-sectional area, membrane thickness, the semi-axis length and influential radius along the semi-axis  $a$ , respectively.  $E_x$ ,  $\Delta\phi$ ,  $\phi_{i,a}$ ,  $\phi_{loc,a}$  and  $\phi_a^{max}$  denote the external field strength, the induced transmembrane potential, the cytoplasmic potential, the actual potential at the surface and the maximum potential at the surface, respectively. For symmetry reasons, the induced potential in the center is assumed 0 V (redrawn after Gimsa and Wachner 2001a).



In the case of semiaxis  $a$  being oriented in the field direction  $\Delta\phi_a$  can be expressed by the voltage divider properties of lump model,  $\Delta\phi_a$  becomes (compare to appendix D):

$$\Delta\phi_a = \frac{C_i C_e}{(C_m C_e + C_i C_e + C_m C_i)} \phi_a^{\max} \quad (4.2)$$

where  $C_i$ ,  $C_m$  and  $C_e$  are the capacitance of cytoplasm, membrane and external medium, respectively.  $\phi_a^{\max}$  stands for the maximum of  $\phi_{loc,a}$  determined by the influential radius distance from the symmetry plane along semiaxis  $a$ ,  $a_{infl}$  (see appendix D and Gimsa and Wachner 2001a). The relation of capacitance and permittivity of each element is given by:

$$\begin{aligned} C_i &= \frac{\varepsilon_i \varepsilon_0 A}{a} \\ C_m &= \frac{\varepsilon_m \varepsilon_0 A}{d} \\ C_e &= \frac{\varepsilon_e \varepsilon_0 A}{a_{infl} - a} \end{aligned} \quad (4.3)$$

$\varepsilon_0$ ,  $\varepsilon_i$ ,  $\varepsilon_m$  and  $\varepsilon_e$  stand for permittivity of vacuum, relative permittivities of cytoplasm, membrane and external, respectively. Introduction equation (4.3) into equation (4.2),  $\Delta\phi_a$  can be given by:

$$\Delta\phi_a = \frac{\varepsilon_i \varepsilon_e d}{\varepsilon_m (\varepsilon_e a + (a_{infl} - a) \varepsilon_i)} \phi_a^{\max} \quad (4.4)$$

Analogous expression holds along semiaxis  $c$ . Introducing the simplified influential radii,  $a_{infl}$  and  $c_{infl}$  (appendix C) into equation (4.4) leads to:

$$\Delta\phi_a = \frac{(a + 2c) \varepsilon_i \varepsilon_e E d}{\varepsilon_m ((a + c) \varepsilon_e + c \varepsilon_i)} \quad (4.5)$$

$$\Delta\phi_c = \frac{(a+2c)\varepsilon_i \varepsilon_e E d}{\varepsilon_m (2c\varepsilon_e + a\varepsilon_i)} \quad (4.6)$$

For a single shell sphere both equations (4.5) and (4.6) reduce to (see also Wachner *et al.* 2002):

$$\Delta\phi = \frac{3\varepsilon_i \varepsilon_e E d}{\varepsilon_m (2\varepsilon_e + \varepsilon_i)} \quad (4.7)$$

Interesting cases for limiting shapes are disks or cylinders.  $\Delta\phi$  can be further simplified. For the disk shape,  $\Delta\phi$  of equations (4.5) and (4.6) is:

$$\Delta\phi_a = \frac{\varepsilon_i E d}{\varepsilon_m} \quad (4.8)$$

$$\Delta\phi_c = \frac{\varepsilon_e E d}{\varepsilon_m} \quad (4.9)$$

Equation (4.8) shows that  $\Delta\phi_a$  depends on  $\varepsilon_i$ , whereas  $\Delta\phi_c$  depends on  $\varepsilon_e$  (equation (4.9)).

For the cylinder-shape the  $\Delta\phi$ -equations in equations (4.5) and (4.6) are simplified to:

$$\Delta\phi_a = \frac{2\varepsilon_i \varepsilon_e E d}{\varepsilon_m (\varepsilon_e + \varepsilon_i)} \quad (4.10)$$

$$\Delta\phi_c = \frac{\varepsilon_i E d}{\varepsilon_m} \quad (4.11)$$

The  $\Delta\phi_a$  induced in the cylinder-shape depends not only on the  $\varepsilon_i$  but also the  $\varepsilon_e$  (equation (4.10)). However, the  $\Delta\phi_c$  of the cylinder-shape is independent on  $\varepsilon_e$  (equation (4.11)).

## 4.2 Effects of cell orientation and electric field frequency on the transmembrane potential induced in ellipsoidal cells

The effects of electric field and cell orientation on the  $\Delta\phi$  induced in ellipsoidal cells were analyzed. The angle at the membrane surface point for the maximum  $\Delta\phi$  of any oriented cells was studied. The theoretical analysis showed that the maximum  $\Delta\phi$  is located at different points of the membrane depending on cell orientation, cell shape, cell parameters and frequency. The theoretical results are compared to experiments obtained from the electropermeabilization of CRBCs in a special chip system with five different distances. Cell permeabilization was determined from propidium iodide (PI) fluorescence-staining of the cell nuclei and cell lysis. The critical field strengths,  $E_{\text{crit}}$  were analyzed for PI permeabilization and non-lysis of cells. In the analysis, the critical transmembrane potential,  $\Delta\phi_{\text{crit}}$  for PI permeabilization was also estimated. Details are presented in appendix D. However, other experimental results are given in the following.

## 4.3 Electropermeabilization experiments

### 4.3.1 On-chip temperature sensor calibration

The resistance and the temperature on EP and ER chips were measured for temperature sensors calibration. The calibration curves are shown in figures 4.2(A) and (B), respectively. During experiments, the resistance of the on-chip temperature sensors was directly measured whereas the temperature on the chips was calculated from the equations of the linear regression as following:

$$R = 99.47 + 0.25T \quad (4.12)$$

and

$$R = 434.05 + 1.13T \quad (4.13)$$

$R$  and  $T$  represent resistance and temperature, respectively. Equations (4.12) and (4.13) were used for temperature calculation on EP and ER chips, respectively.

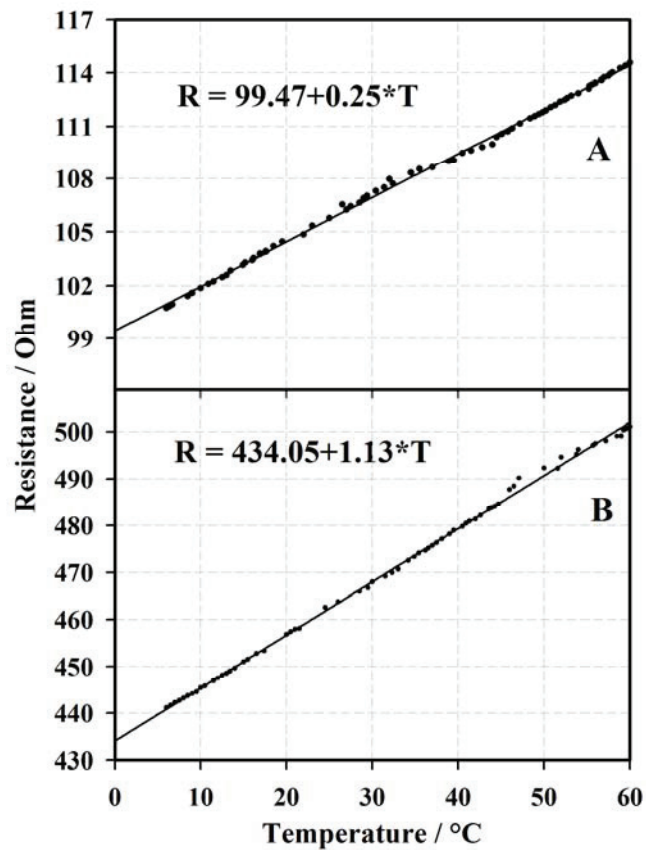


**Figure 4.2** On-chip temperature sensor calibration. (A) relation of resistance and temperature on EP chip. (B) relation of resistance and temperature on the ER chip. The data points were fitted by linear regression. The equations obtained from linear regression were used for temperature calculation.

### 4.3.2 Temperature changes in the chambers by pulse application

Temperature changes in the chamber were obtained from resistance changes of the sensor on each chip measured before and after pulse applications. The temperature changes in EP and ER chip chambers were calculated using equations (4.12) and (4.13), respectively. The increasing temperatures were investigated after pulse application depending on frequency, pulse duration and exposure voltage (figures 4.3 and 4.4). Temperatures in chip chambers before pulse application were  $24.79 \pm 0.59$  °C. The room temperatures were  $25.17 \pm 0.13$  °C. Voltages were exposed from 12 V<sub>pp</sub> to 20 V<sub>pp</sub>. Conductivity of measuring solution was kept constant at 0.12 S m<sup>-1</sup>.

Figures 4.3(A) shows that the increasing temperatures in EP chip chamber are independent on frequencies in these ranges studied. At longer pulse durations the increasing temperatures were found (figure 4.3(B)). The temperatures also increased with increasing exposure voltages. In ER chip chamber the increasing temperatures as a function of frequency are shown in figure 4.4. These results confirm that the increasing temperatures are independent on frequencies. Moreover, at 100 Hz, bubbles were found during pulse applications. Room temperatures were always constant during pulse applications for all experiments.

However, after pulse application a short temperature increase has been observed with a maximum of 0.9 degrees and 1.5 degrees for EP and ER chambers, respectively. Accordingly, the temperature changes after pulse applications did not affect to the PI permeabilization and non-lysis for both chip chambers. Please note that the peak temperature increase approx. 50 s for EP chamber and 40 s for ER chamber. These results indicate the thermal constant of the chip and the chip carrier. The temperatures decreased to room temperature again after the pulse approx. one more minute.

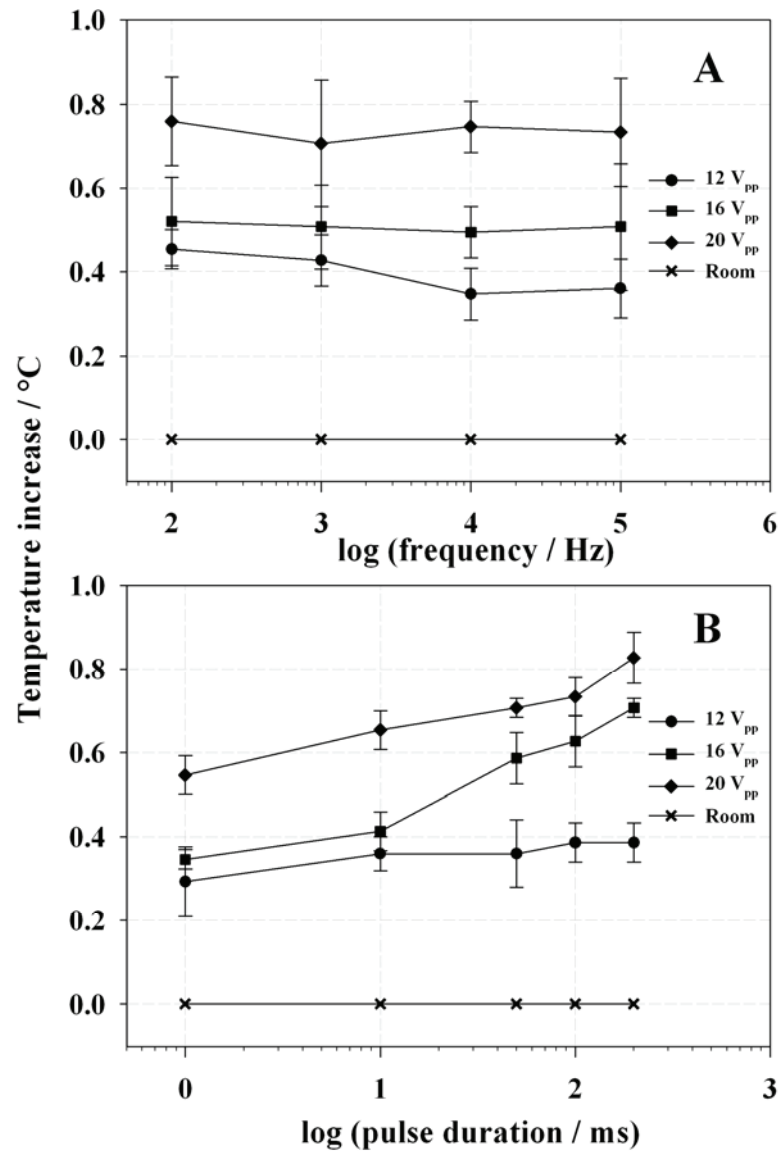


**Figure 4.3** Increasing temperatures after pulse applications in EP chip chamber. (A) frequency dependence of temperatures. Frequencies range from 100 Hz to 100 kHz. Pulse duration was kept constant at 10 ms. (B) comparison of the pulse durations and increasing temperatures. Pulse durations range from 1 ms to 200 ms. The frequency was kept constant at 1 kHz. Each data point was obtained from 3 repeats.

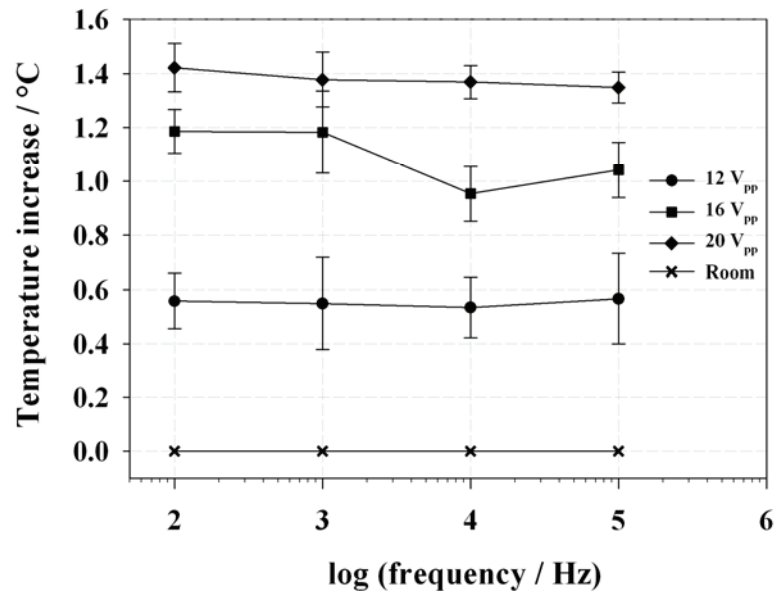


**Figure 4.4** Increasing temperatures after pulse applications in ER chip chamber. A frequency dependence of temperature increase was obtained. Frequencies range from 100 Hz to 100 kHz. Pulse duration was kept constant at 10 ms. Each data point was obtained from 3 repeats.

### 4.3.3 Shape of chicken red blood cells

Nikinmaa (1990) presented that, under no-flow conditions, most of the non-nucleated mammals red cells are biconcave discs. The primitive erythrocytes of other vertebrates are round and flattened, with a central bulge caused by the nucleus. The definitive nucleated red cells are ellipsoidal. The amount of DNA in the nucleus of different vertebrate red cells varies markedly: the chicken (*Gallus domesticus*) nuclei contain approximately 40% of the amount of DNA found in human peripheral leukocyte nuclei. Nucleated red cells also contain other cellular organelles, with a number depending on the vertebrate group and the maturation stage of the erythrocyte.

In this study, the shape of CRBCs suspended in low conductivity solution ( $\sigma_e = 0.12 \text{ S m}^{-1}$ ) was microscopically observed (Olympus IX71, Japan). Photos were

---

recorded on hard disk and monitored by a computer interface using the Cell-P program (Soft Imaging System GmbH, Germany). CRBCs were ellipsoidal in shape with a central bulge caused by the nucleus (figure 4.5). The mean semiaxis lengths of  $a$ ,  $b$ , and  $c$  were  $6.66 \pm 0.19 \mu\text{m}$ ,  $4.17 \pm 0.26 \mu\text{m}$  and  $1.43 \pm 0.08 \mu\text{m}$ , respectively. These results were obtained from 60 cells collected in 3 repeats. Please note that the orientation of cells in their  $a$ - $c$  plane was not stable enough for electropermeabilization experiments. Only cells oriented in the  $a$ - $b$  plane could be used for electropermeabilization experiments (figure 4.5). Microphotographs of CRBCs, obtained via a Scanning Electron Microscope, SEM (DSM 960A, Carl Zeiss, Oserkochen, Germany), are shown in appendix D.



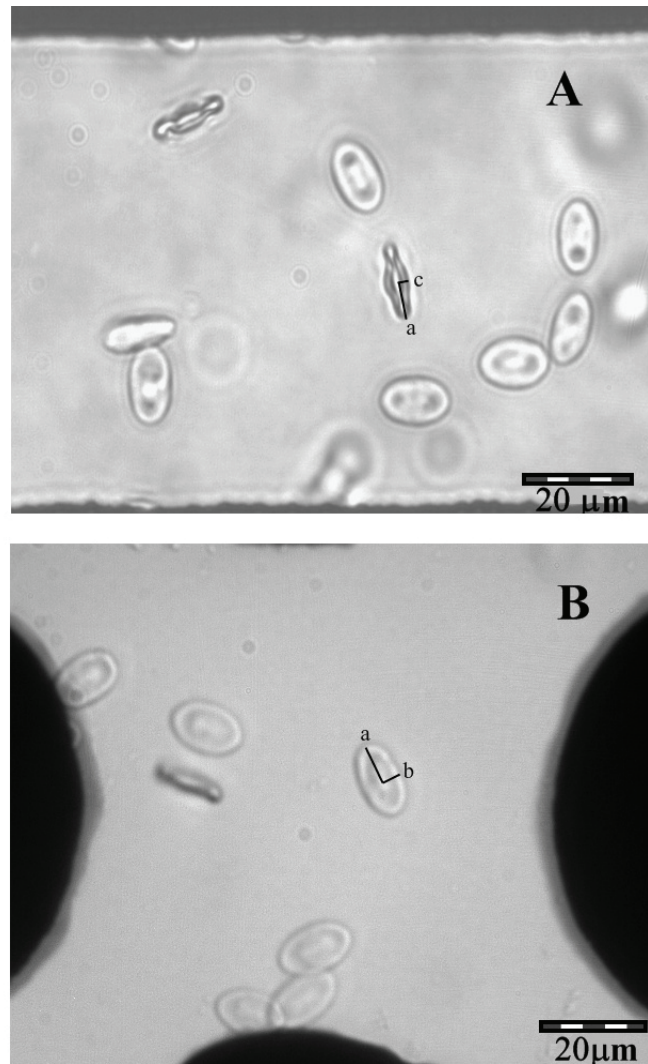


**Figure 4.5** The microscopic image of CRBCs with a magnification of 60X. (A) and (B) show the different orientations of cells on EP and ER chip chambers, respectively. The semi-axis lengths of  $a$ ,  $b$  and  $c$  could be measured using the Cell-P program.

### 4.3.4 Conductivity of cell suspensions

Normally, fresh blood was preserved in Alsever's solution before suspension in the measuring solution. The conductivities of cell solution with washed cells and cell suspensions without washed cells were compared. In the case of washed cell, 1.5 ml of fresh blood was washed thrice in PB solution (Chapter 3) by centrifugation using a centrifuge (Sigma 1-15, Fisher Bioblock Scientific, Osterode, Germany) at 500×g for 5 minutes (Lippert and Gimsa 2002). The sedimented pellet was transferred to the measuring solution. Washed cells suspended in measuring solution were diluted to 10 ml with a hematocrit of 0.03%. For cell suspensions without washing, fresh blood preserved in Alsever's solution was directly diluted in 10 ml of measuring solution with a hematocrit of 0.03% as well. The conductivities of both cell suspensions were measured by the conductometer (inoLab Cond Level 1, WTW GmbH, Weilheim, Germany) and compared to control solution without cells. From three repeats, the conductivities of control, washed cell suspensions and cell suspensions without washing at 20 °C are shown in table 4.1. These results show that the conductivities of both cell suspensions are not significant different from the control solution. Accordingly, cell suspensions without washing were used for electroporabilization experiments.

**Table 4.1** Conductivity of cell suspensions

Cell suspensions	Conductivity (S m <sup>-1</sup> )
Washed cell suspensions	0.1192 ± 0.0002
Cell suspensions without washing	0.1194 ± 0.0003
Control solution without cells	0.1198 ± 0.0002

Moreover, for electroporabilization experiment the cell suspension was combined with 10 μM of PI. Accordingly, the conductivities of cell suspensions containing 10 μM of PI and without PI were compared. The conductivities of cell suspensions containing 10 μM of PI and without PI compared to the control solution are presented in table 4.2. They are

not significant different. These results indicate that PI does not affect to the conductivity of the cell suspensions at a concentration of 10  $\mu\text{M}$ .

**Table 4.2** Conductivity of cell suspensions containing PI and without PI

Cell suspensions	Conductivity ( $\text{S m}^{-1}$ )
Cell suspensions containing 10 $\mu\text{M}$ of PI	$0.1266 \pm 0.0005$
Cell suspensions without PI	$0.1264 \pm 0.0007$
Control solution without cells	$0.1263 \pm 0.0006$

### 4.3.5 Electroporabilization of oriented chicken red blood cells in linear square-wave AC-fields

This study focused at the observation of electroporabilization of CRBCs in linear square-wave AC-fields by fluorescence. The effects of AC electric field strength, field frequency, pulse duration and cell orientation on the electroporabilization and cell lysis were considered (see appendix D for details). These experiments were analyzed in the EP chip chamber. However, some different results from appendix D are shown below.

#### *Dependence of electroporabilization of oriented cells on electric field strength*

Observations of electroporabilization by the fluorescence changes of PI staining the nucleus of CRBCs are shown in figure 4.6. The standard parameters are shown in table 4.3. Within 1-10 s, the dye lightly stained at the nucleus of cells (figure 4.6(B)). After 10 s, the dye increasingly diffused to the nucleus. The brightness became stable within 2-3 min (figures 4.6(D-F)). Accordingly, PI permeabilization of all conditions was considered within 3 min after pulse application.

**Table 4.3** Standard parameters for investigating the dependence of electropermeabilization of oriented cells on electric field strength

Parameter	Value
Conductivity of solution	0.12 S m <sup>-1</sup>
Exposure voltage	16 V <sub>pp</sub>
Field frequency	1 kHz
Pulse duration	10 ms

Within 1-10 s, the dye lightly stained at the nucleus of cells (figure 4.6(B)). After 10 s, the dye increasingly diffused to the nucleus. The brightness became stable within 2-3 min (figures 4.6(D-F)). Accordingly, PI permeabilization of all conditions was considered within 3 min after pulse application.

Moreover, the effect of electric field strength on PI permeabilization was investigated (figure 4.7). In this study, conductivity of solution, exposure voltage, pulse duration and field frequency were kept constant (table 4.3). Angles of cell orientations between electric field  $E$  and semiaxis  $a$  of  $\delta(0^\circ, 45^\circ \text{ and } 90^\circ)$  were used. Figure 4.7 shows the comparison of the PI permeabilization of cells under different field strengths generated by different distances between two parallel electrodes. At the field strengths of 200 kV m<sup>-1</sup> and 160 kV m<sup>-1</sup>, the nucleus of cells could be stained by PI, whereas at 107 kV m<sup>-1</sup> only one cell was stained. These results show that the percentage of PI permeabilization increases with increasing field strength (Lebar and Miklavcic 2001, Müller *et al.* 2001, Puc *et al.* 2003, Rols and Teissié 1990, 1998 and Wolf *et al.* 1994). Please note that the angle of cell orientation before and after pulse application of some cells changed (number 1 in figures 4.7(A) and (B)) because of cell movements over ground before the pulse. Whereas in the case of immotile cells, the angle of cell orientation did not change (number 3 in figures 4.7(A) and (B)).

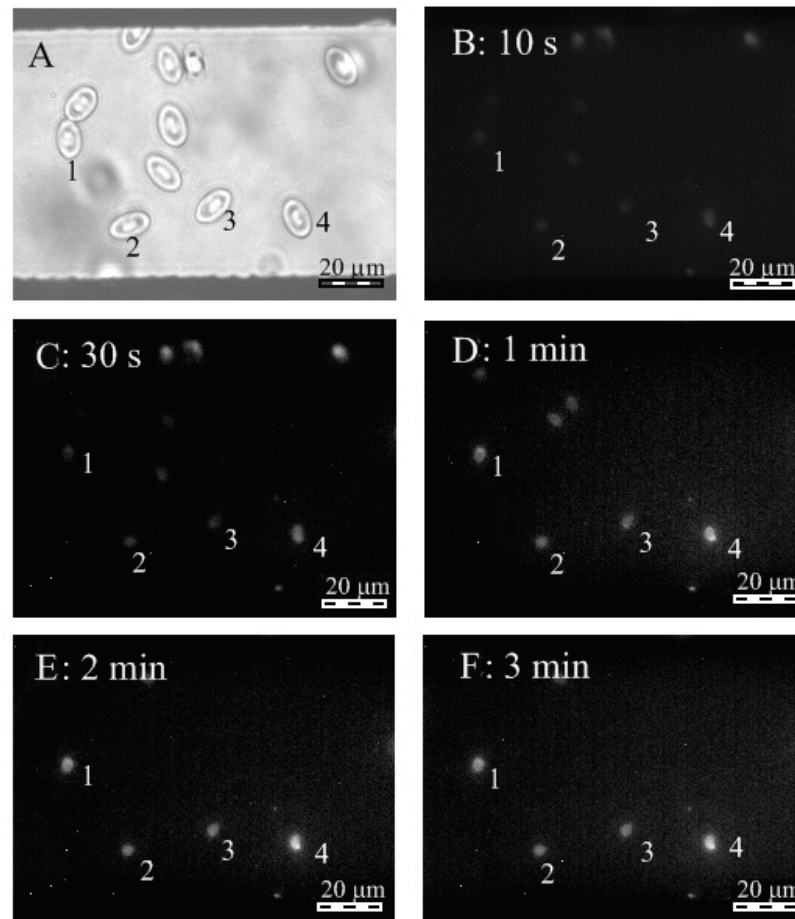


**Figure 4.6** Fluorescence changes of PI staining of CRBCs-nuclei after pulse application. The distance between two parallel electrodes was 80 μm. (A) cells were immediately observed under phase contrast after immediate pulse application. Other figures (B, C, D, E and F): cells were examined under fluorescence after pulse application within 10 s, 30 s, 1 min, 2 min and 3 min, respectively. Numbers indicate PI permeabilized cells.

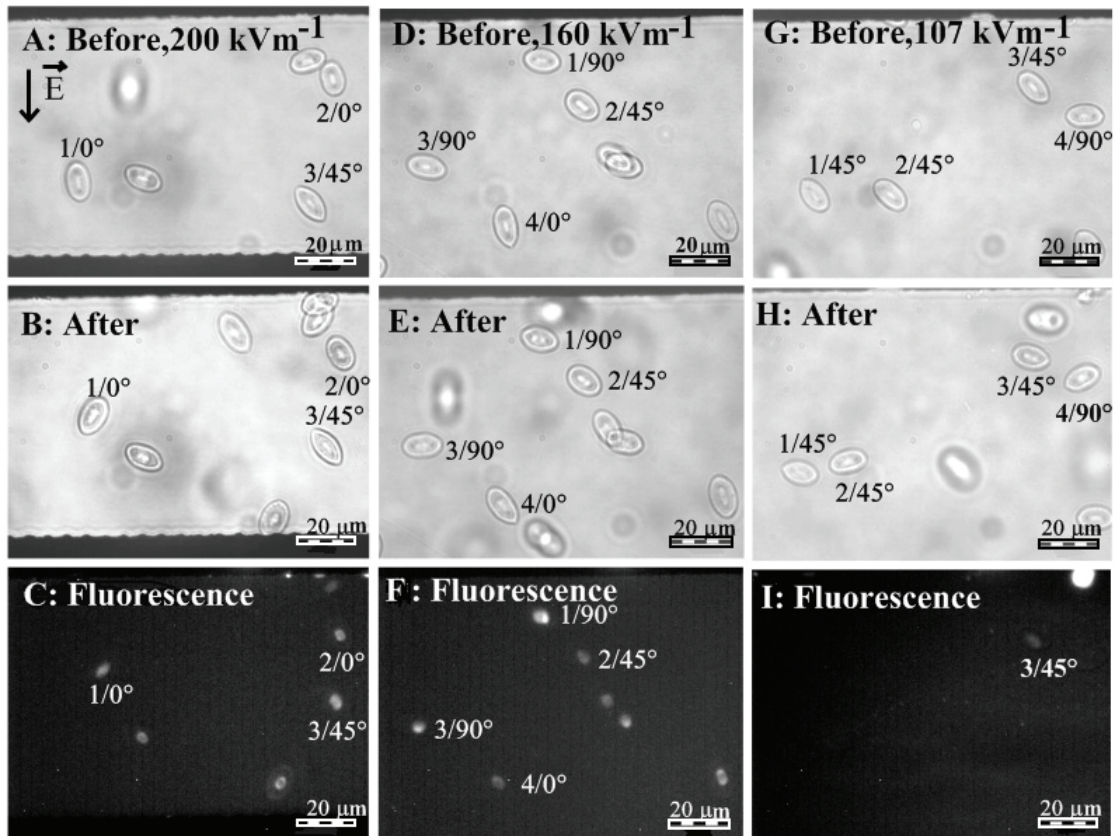


**Figure 4.7** Electropermeabilization of oriented CRBCs in different field strengths. The distance between two parallel electrodes was  $80\ \mu\text{m}$  (*A-C*),  $100\ \mu\text{m}$  (*D-F*) and  $150\ \mu\text{m}$  (*G-I*). *A*, *B*, *D*, *E*, *G* and *H*: cells were observed under phase contrast before and after pulse application. *C*, *F* and *I*: cells were examined under fluorescence 3 min after pulse application. Numbers and orientation angles of their semiaxes  $a$  with respect to the field are marked.

### ***Dependence of PI permeabilization and cell lysis on field frequency***

The percentages of PI permeabilization and non-lysis (survival) were analyzed for various cell orientations ( $\delta = 0^\circ, 45^\circ$  and  $90^\circ$ ) and at different frequencies (table 4.4).

**Table 4.4** Parameters for investigating the PI permeabilization and non-lysis depending on field frequency

Parameter	Value
Conductivity of solution	$0.12 \text{ S m}^{-1}$
Pulse duration	10 ms
Frequency variations	100 Hz, 1 kHz, 10 kHz, 100 kHz, 150 kHz
Electric field strength variations	$93.33\text{-}250 \text{ kV m}^{-1}$

Results indicated that the PI permeabilization at low frequency was higher than at high frequency, whereas the non-lysis of cells was higher at high frequency (appendix D and compare to Gimsa and Wachner 1998).

Figure 4.8 presents the examples of PI permeabilization under different frequencies. At 1 kHz and 10 kHz, all cells of all orientations were permeabilized (figure 4.8(C) and figure 4.8(F)). At 150 kHz, only two PI permeabilized cells out of five cells were found (numbers 2 and 3 in figure 4.8(I)). These results confirm that PI permeabilization of cells decreases with increasing frequency (see appendix D for details).

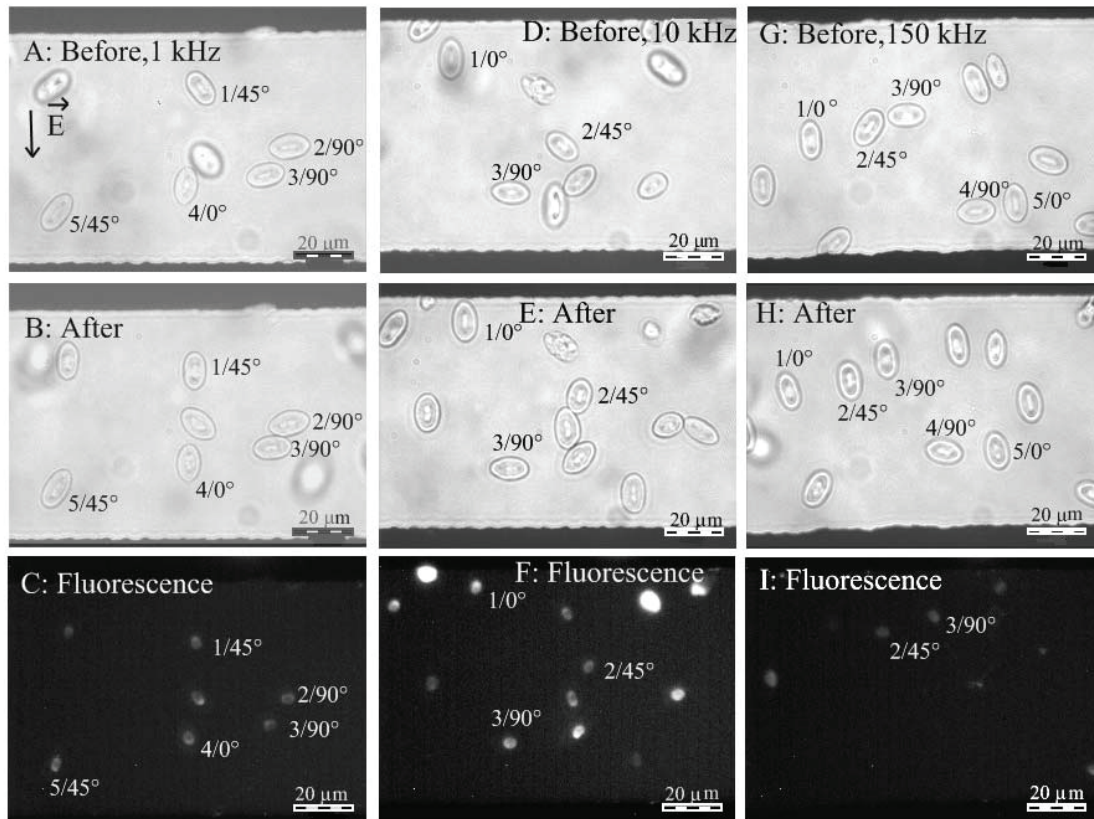


**Figure 4.8** Electroporation of oriented CRBCs for frequency variations. The distance between two parallel electrodes was 80  $\mu\text{m}$ . Cells were exposed to 16  $V_{pp}$  ( $E = 200 \text{ kV m}^{-1}$ ). The frequency variations were 1 kHz (A-C), 10 kHz (D-F) and 150 kHz (G-I).



### ***Dependence of PI permeabilization and cell lysis on pulse duration***

Parameters presented in table 4.5 were used for consideration of the effect of pulse duration on PI permeabilization and non-lysis.

**Table 4.5** Parameters for investigating the PI permeabilization and non-lysis depending on pulse duration

Parameter	Value
Conductivity of solution	0.12 S m <sup>-1</sup>
Frequency	1 kHz
Pulse duration	1 ms, 10 ms, 50 ms, 100 ms and 200 ms
Electric field strength variations	80-250 kV m <sup>-1</sup>

The results show that at shorter pulse duration required higher field strength for increasing PI permeabilization, whereas at longer pulse duration the PI permeabilization required lower field strength. Nevertheless, at longer pulse duration, the decreasing non-lysis were found (appendix D and compare to Rols and Teissié 1990 and 1998). Furthermore, the PI permeabilization and cell lysis also depend on orientation angle of semiaxis  $a$  with respect to the field ( $\delta$ ). At  $\delta = 0^\circ$ , the PI permeabilization was higher than at  $\delta = 45^\circ$  and  $90^\circ$ , respectively. In contrast, the non-lysis of cells were lower for any conditions (see appendix D and compare to Valic *et al.* 2003).

The examples of pulse duration dependence under fluorescence light were shown in figure 4.9. The results show that at 1 ms of pulse duration, the percentage of PI permeabilization is lower than at the longer pulse durations. However, at 200 ms only lysed cells were found (numbers 1 and 2 in figure 4.9(I)). Cells located near electrodes are more easily stained and lysed because of the stronger electric field strength (number 4, figure 4.9(C)).

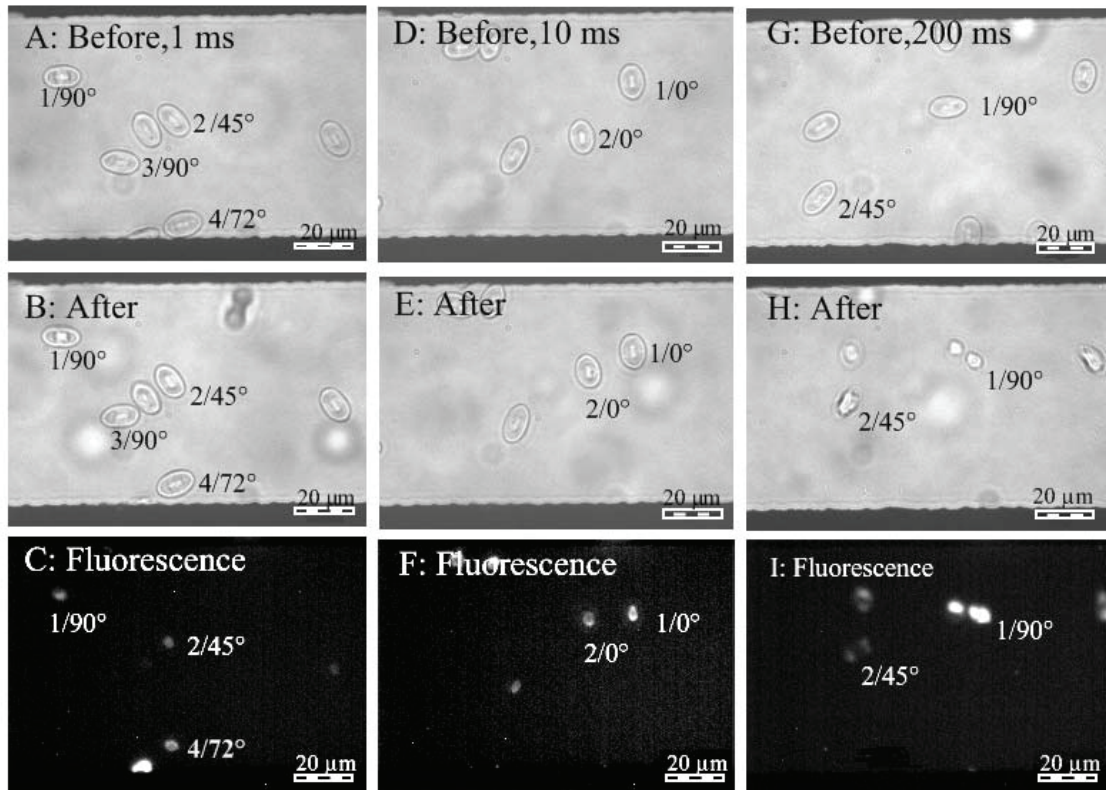


**Figure 4.9** Electroporation of oriented CRBCs in different pulse durations. The distance between two parallel electrodes was  $80\ \mu\text{m}$ . Cells were exposed to  $16\ \text{V}_{\text{pp}}$  ( $E = 200\ \text{kV m}^{-1}$ ). The variations of pulse duration were 1 ms (A-C), 10 ms (D-F) and 200 ms (G-I).

### 4.3.6 Electroporation of chicken red blood cells in square-wave rotating electric fields

The electroporation of CRBCs in square-wave rotating fields were also studied for comparison with electroporation in linear square-wave AC-fields. The rotating fields were generated in the ER chamber by four  $90^\circ$ -phase shifted signal (see Chapter 2). Effects of field strength and field frequency were considered for PI-permeabilization and non-lysis of cells. An ER chip with rounded-tip electrodes was

used (see Chapter 3). The  $\Delta\phi_{crit}$  was also estimated. Table 4.6 shows the parameters for these experiments.

**Table 4.6** Parameters for observations of electroporation of CRBCs in rotating fields

Parameter	Value
Conductivity of solution	0.12 S m <sup>-1</sup>
Pulse duration	10 ms
Frequency variations	1 kHz, 10 kHz, 50 kHz, 100 kHz, 150 kHz
Electric field strength variations	74-186 kV m <sup>-1</sup>

### ***Dependence of PI permeabilization and cell lysis on electric field strength and frequency***

Rotating fields effects are shown in figure 4.10. Frequencies of 1 kHz, 10 kHz and 150 kHz were compared. At 1 kHz and 10 kHz, the percentage of PI permeabilization is higher than at 150 kHz (figures 4.10(A-C) and figures 4.10(D-F) compare to figures 4.10(G-I)). These results confirm that the PI permeabilization of cells decreases with increasing frequency (compare to figure 4.8). Please note that in the vicinity of the electrodes, lysed cells easily occurred (number 2 in figure 4.10(C) and see also Chapter 2). The percentages of PI permeabilization and non-lysis of cells of CRBCs in rotating fields with different frequencies are shown in figure 4.11. These results are corresponding to the case of PI permeabilization in linear AC-fields measured in EP chip chamber.

Figure 4.11 shows that the percentage of PI permeabilization increases, whereas the percentage of non-lysis of cells decreases with increasing electric field strength. Sigmoidal curves were fitted to the data points to analyze the  $E_{crit}$  of PI permeabilization and  $E_{crit}$  of non-lysis (compare to appendix D). Only cells in the central region were observed because of the homogeneous field (Chapter 2).

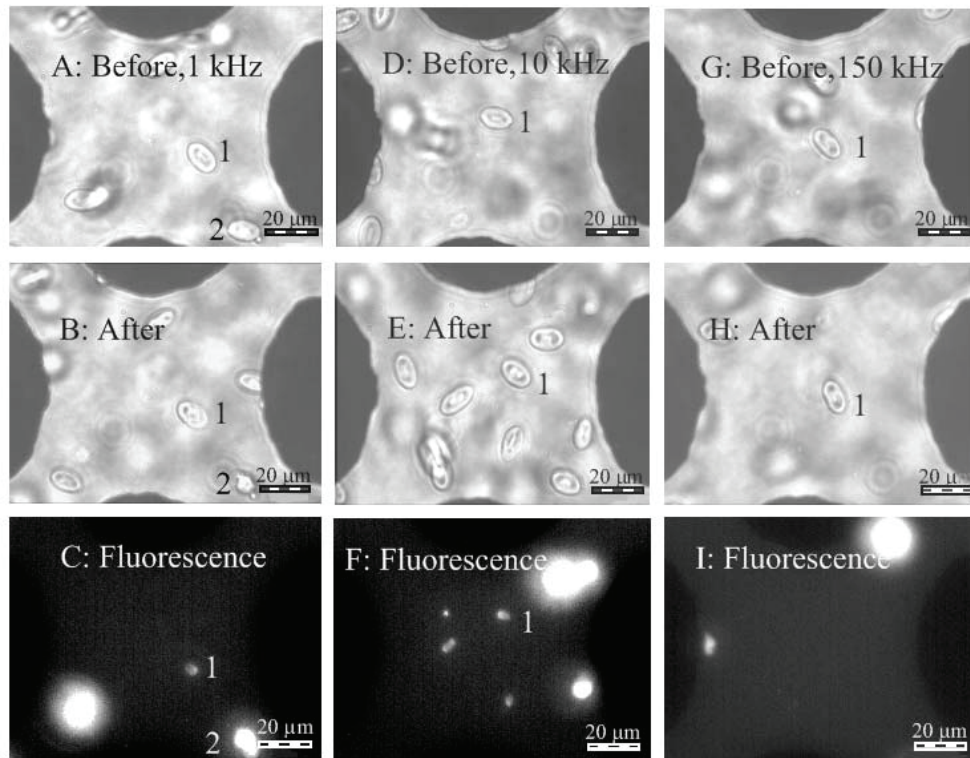


**Figure 4.10** Electroporation of oriented CRBCs in rotating field. The distance between two opposed electrodes is 75  $\mu\text{m}$ . Cells were exposed to 11  $V_{\text{pp}}$  ( $E = 116 \text{ kV m}^{-1}$ ). The frequency variations were 1 kHz (A-C), 10 kHz (D-F) and 150 kHz (G-I). Numbers are marked for observations.

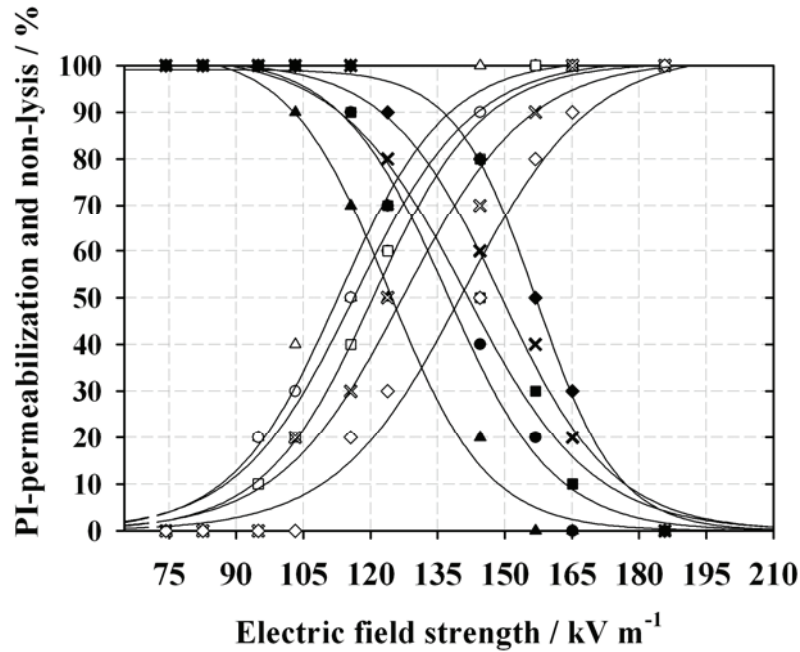


**Figure 4.11** Effect of field frequency on the percentage of PI permeabilization and non-lysis in square-wave rotating fields. Solid lines denote the fitted sigmoidal curves. Frequencies variations: 1 kHz ( $\Delta$ ), 10 kHz (o), 50 kHz ( $\square$ ), 100 kHz ( $\times$ ) and 150 kHz ( $\diamond$ ). Hollow and filled symbols indicate PI permeabilization and non-lysis, respectively.

### *Dependence of the critical electric field strength of cells on field frequency*

Figure 4.12 shows the effect of frequency on the  $E_{crit}$  of PI permeabilization and  $E_{crit}$  of non-lysis. In this frequency range (table 4.6), the  $E_{crit}$  of PI permeabilization was always lower than the  $E_{crit}$  of non-lysis (compare to the results of the EP chamber in appendix D). Figure 4.12 also indicates that the  $E_{crit}$  of non-lysed cells increases with increasing frequency.

For consideration of  $E_{crit}$  of PI permeabilization, it is constant at low frequencies (1 – 50 kHz) and increasing at higher frequencies (100 - 150 kHz) (see also appendix D). However, the PI permeabilization in rotating fields is not dependent on the angle.

Gimsa *et al.* (1992) presented that the PI permeabilization of non-spherical cell in rotating fields occurred in the membrane areas closed to its longest axis. Accordingly, the theoretical curve was calculated using cell parameters of CRBCs and orientation angle of  $\delta=0^\circ$  compared to experimental data points of  $E_{crit}$  of PI permeabilization (compare to appendix D). The  $\Delta\phi_{crit}$  was 0.79 V for PI permeabilization in rotating fields. This value is lower than the  $\Delta\phi_{crit}$  at  $\delta=0^\circ$  in the EP chamber (appendix D). This suggests that the  $\Delta\phi_{crit}$  induced in rotating fields is lower than in linear AC-fields.

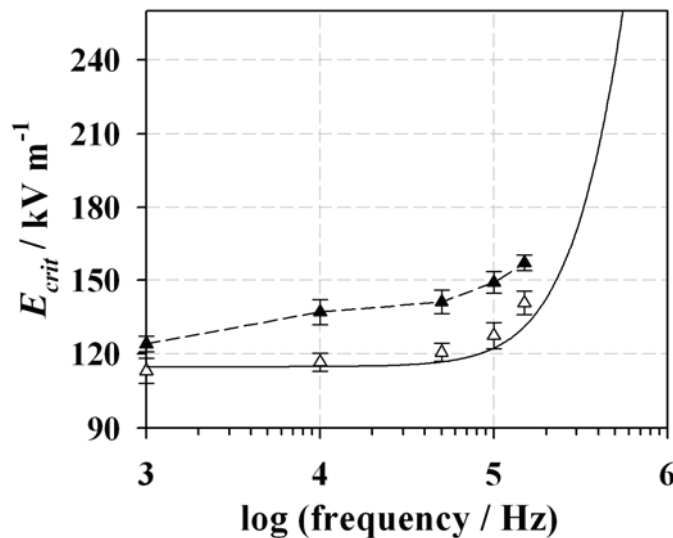


**Figure 4.12** Comparison of the critical electric field strength for PI permeabilized and non-lysed cells as function of field frequency. Data points of  $E_{crit}$  of non-lysis (filled-triangle) and  $E_{crit}$  of PI permeabilization (hollow-triangle) were obtained from the fitted sigmoidal curves shown in figure 4.11. Solid line shows the theoretical curve using parameters of CRBCs (see text).

## Chapter 5

# Simplifications of dielectrophoretic force

### 5.1 Introduction

Gimsa (2001) presented that the dielectrophoretic force acting on ellipsoidal particles is given by:

$$\langle \vec{F}_x \rangle = \varepsilon_e \varepsilon_0 V \text{CMF}_a^{\text{Re}} E_0^2 \frac{\gamma}{2} \hat{i} \quad (5.1)$$

when the semiaxis  $a$  oriented in parallel to the field. Equation (5.1) shows that the frequency dependence of the dielectrophoretic force is described by the real part of  $\text{CMF}_a$  ( $\text{CMF}_a^{\text{Re}}$ ) along the semiaxis  $a$  oriented in parallel to the field. Orientation of the ellipsoidal particle along the other two axes would change the index of  $\text{CMF}$ .  $V$  and  $E_0$  stand for particle volume and the amplitude of the electric field. Parameter  $\gamma$  describes the small field gradient. In case of the semiaxis  $a$  being oriented in parallel to the field in  $x$ -direction, the  $\text{CMF}_a$  is given by (Gimsa 2001):

$$\text{CMF}_a = \frac{1}{n_a} \left( \frac{\phi_{e,a} - \phi_{loc,a}}{\phi_{e,a}} \right) \quad (5.2)$$

$$\text{CMF}_a = \frac{a_{\text{infl}}}{a_{\text{infl}} - a} \left( 1 - \frac{Z_{i,a}^* + Z_m^*}{Z_{i,a}^* + Z_m^* + Z_{e,a}^*} \frac{a_{\text{infl}}}{a} \right) \quad (5.3)$$

with

$$\frac{a_{\text{infl}}}{a} = \frac{1}{1 - n_a} \quad (5.4)$$

and

$$\frac{Z_{i,a}^* + Z_m^*}{Z_{i,a}^* + Z_m^* + Z_{e,a}^*} = \frac{\frac{a}{\sigma_i + j\omega\epsilon_e\epsilon_0} + \frac{d}{\sigma_m + j\omega\epsilon_m\epsilon_0}}{\frac{a}{\sigma_i + j\omega\epsilon_e\epsilon_0} + \frac{d}{\sigma_m + j\omega\epsilon_m\epsilon_0} + \frac{a_{\text{infl}} - a}{\sigma_e + j\omega\epsilon_e\epsilon_0}} \quad (5.5)$$

Please note that equation (5.3) is valid for the case of a single-shell object. The influential radius,  $a_{\text{infl}}$  can be expressed by the depolarizing factor,  $n_a$  (equation (5.4) and Gimsa 2001). Analogous expressions hold along the other two semiaxes. To consider the dielectrophoretic force (equation (5.1)), simplifications of CMF for spheroidal cells are considered in the following.

## 5.2 Simplifications of dielectrophoretic force for spheroidal cells

Introduction of simplified equations of  $a_{\text{infl}}$  and  $c_{\text{infl}}$  (appendix C) into equation (5.3), the CMF along semiaxes  $a$  and  $c$  become:

$$\text{CMF}_a = \frac{a+2c}{c} \left( 1 - \frac{Z_{i,a}^* + Z_m^*}{Z_{i,a}^* + Z_m^* + Z_{e,a}^*} \left( \frac{a+2c}{a+c} \right) \right) \quad (5.6)$$

$$\text{CMF}_c = \frac{a+2c}{a} \left( 1 - \frac{Z_{i,c}^* + Z_m^*}{Z_{i,c}^* + Z_m^* + Z_{e,c}^*} \left( \frac{a+2c}{2c} \right) \right) \quad (5.7)$$

When semiaxes  $a$  and  $c$  are oriented in parallel to the field, dielectrophoretic forces can be expressed by the real part of  $\text{CMF}_a$  and  $\text{CMF}_c$ , respectively (figure 5.1).

For analysis the equatorial radius was kept constant ( $a = 3.5 \mu\text{m}$ ). The semiaxes ratios of  $c:a=1:3.5$ ,  $1:5$ ,  $1:10$  (oblate),  $c:a=1:1$  (sphere) and  $c:a=2:1$ ,  $5:1$ ,  $10:1$  (prolate) were considered. Cell parameters were given in table 5.1.



Figure 5.1 shows the real part of CMF resulting in the dielectrophoretic force. All cases indicate that the first and the second plateaus ( $F_1$  and  $F_2$ ) depend on the axis ratios, whereas the third plateau ( $F_3$ ) is not significantly different. In case of the semiaxis  $a$  being oriented in parallel to the electric field,  $F_1$  of the real part of  $\text{CMF}_a$  is lower for prolate spheroids than for spheres and oblate spheroids (figures 5.1(A), (B) and (C)). In contrast,  $F_2$  of the prolate is higher than for spheres and oblate spheroids.

In the case of semiaxis  $c$  being oriented in parallel to the electric field,  $F_1$  and  $F_2$  of the real part of  $\text{CMF}_c$  are higher for prolate spheroids than for spheres and oblate spheroids (figures 5.1(D), (E) and (F)). Errors of simplified equations (equations (5.6) and (5.7)) were also considered for the real part of  $\text{CMF}_a$  and  $\text{CMF}_c$ . The errors of the real part of  $\text{CMF}_a$  are always smaller than 4% in dependent of shape (dotted lines in figure 5.1).

Large errors of  $F_1$  are found for oblate spheroids (<16%, figure 5.1(D), (E) and (F)) for the real part of  $\text{CMF}_c$  as well as for  $F_2$  for the long prolate shape with an axis ratio of 10:1 (40%, figure 5.1(F)), respectively. This suggests that the errors of  $F_1$  and  $F_2$  for the real part of  $\text{CMF}_c$  will be larger for very thin disk and long cylinder, respectively. However, the errors of  $F_3$  for all cases are always smaller than 2%.

**Table 5.1** Cell parameters of spheroid for model calculations (Gimsa and Wachner 1999)

<b>Parameter</b>	<b>Value</b>
Semiaxes lengths of $a$ and $b$	3.5 $\mu\text{m}$
Semiaxis $c$	0.35 $\mu\text{m}$ – 35 $\mu\text{m}$
Membrane thickness ( $d$ )	8 nm
Conductivities / relative permittivities	
- Internal; $\sigma_i$	0.53 S $\text{m}^{-1}$
- Membrane; $\sigma_m$	1 $\mu\text{S m}^{-1}$
- External; $\sigma_e$	0.12 S $\text{m}^{-1}$
Area specific membrane conductance ( $g_m$ )	125 S $\text{m}^{-2}$
Area specific membrane capacitance ( $C_m$ )	0.01 F $\text{m}^{-2}$
Relative permittivities	
- Internal; $\varepsilon_i$	50
- Membrane; $\varepsilon_m$	9.04
- External; $\varepsilon_e$	80

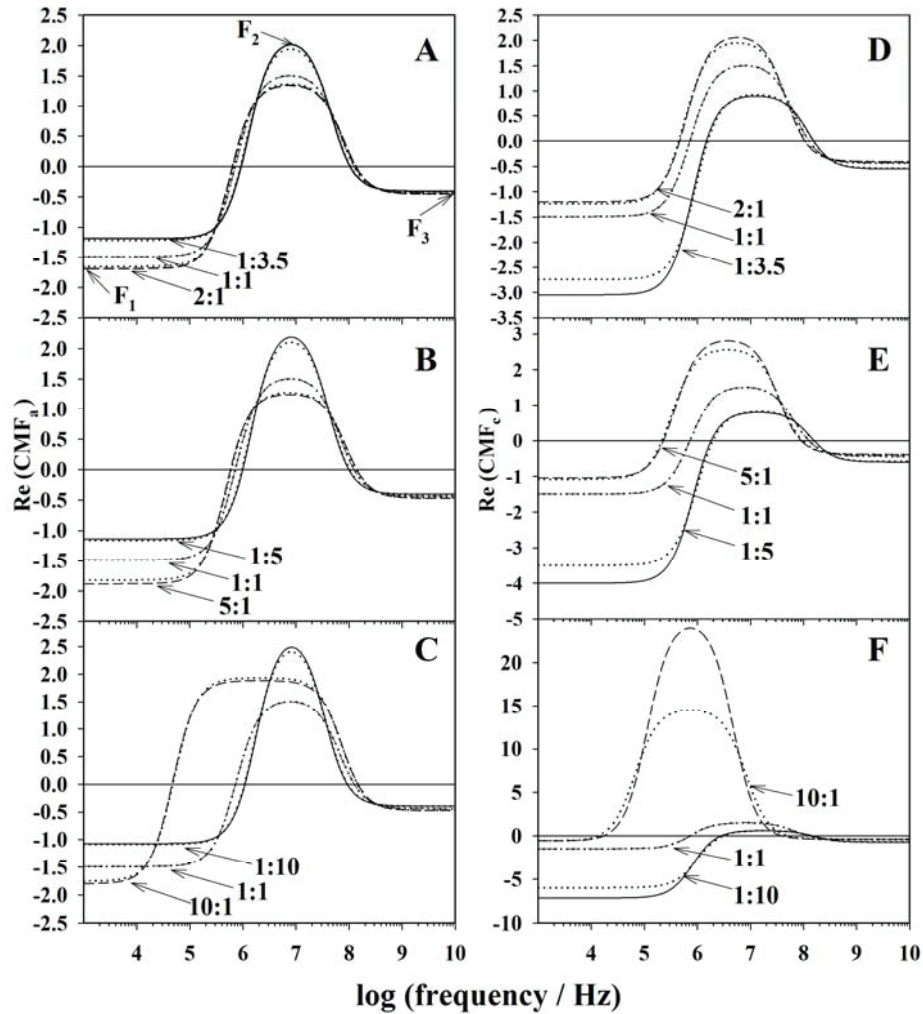


**Figure 5.1** Real part of the CMF of the spheroidal single shell model as a function of frequency. (A), (B) and (C): real part of CMF when the semiaxis  $a$  being oriented in parallel to the electric field. (D), (E) and (F): real part of CMF when the semiaxis  $c$  oriented in parallel to the electric field. Cell parameters were given in table 5.1. The curves for the full model (equation (5.3)) were compared for the axis ratios of 1:3.5, 1:5, 1:10 (oblate, solid lines), 1:1 (sphere, dashed-dotted lines) and 2:1, 5:1, 10:1 (prolate, dashed lines). Dotted lines stand for the curves calculated by simplified equations (equations (5.6) and (5.7)). For the DP, characteristic force plateaus ( $F_1$ ,  $F_2$ ,  $F_3$ ) were marked.

The characteristic force plateaus of  $F_1$ ,  $F_2$  and  $F_3$  (figure 5.1) derived by simplified schemes are given by (Gimsa and Wachner 1999):

$$F_1 = \left( \frac{a_{\text{infl}}}{a} \right) \frac{a g_m (\sigma_i - \sigma_e) - \sigma_i \sigma_e}{g_m ((a_{\text{infl}} - a) \sigma_i + a \sigma_e) + \sigma_i \sigma_e} \quad (5.8)$$

$$F_2 = \frac{a_{\text{infl}} (\sigma_i - \sigma_e)}{(a_{\text{infl}} - a) \sigma_i + a \sigma_e} \quad (5.9)$$

$$F_3 = \frac{a_{\text{infl}} (\varepsilon_i - \varepsilon_e)}{(a_{\text{infl}} - a) \varepsilon_i + a \varepsilon_e} \quad (5.10)$$

These equations are complicate because of the complex expressions of  $a_{\text{infl}}$  relating to the depolarizing factors (Gimsa and Wachner 1999). Accordingly, simplified equations of the characteristic force plateaus were obtained by introducing the simplified equations for  $a_{\text{infl}}$  and  $c_{\text{infl}}$  (appendix C). The characteristic force plateaus for the real part of  $\text{CMF}_a$  ( $F_{1,a}$ ,  $F_{2,a}$  and  $F_{3,a}$ ) are simplified to:

$$F_{1,a} = \frac{(a + 2c)(a g_m (\sigma_i - \sigma_e) - \sigma_i \sigma_e)}{a g_m (c \sigma_i + (a + c) \sigma_e) + (a + c) \sigma_i \sigma_e} \quad (5.11)$$

$$F_{2,a} = \frac{(a + 2c)(\sigma_i - \sigma_e)}{c \sigma_i + (a + c) \sigma_e} \quad (5.12)$$

$$F_{3,a} = \frac{(a + 2c)(\varepsilon_i - \varepsilon_e)}{c \varepsilon_i + (a + c) \varepsilon_e} \quad (5.13)$$

For the real part of  $\text{CMF}_c$ , the characteristic force plateaus ( $F_{1,c}$ ,  $F_{2,c}$  and  $F_{3,c}$ ) are given by:

$$F_{1,c} = \frac{(a + 2c)(c g_m (\sigma_i - \sigma_e) - \sigma_i \sigma_e)}{c g_m (a \sigma_i + 2c \sigma_e) + 2c \sigma_i \sigma_e} \quad (5.14)$$

$$F_{2,c} = \frac{(a+2c)(\sigma_i - \sigma_e)}{a\sigma_i + 2c\sigma_e} \quad (5.15)$$

$$F_{3,c} = \frac{(a+2c)(\varepsilon_i - \varepsilon_e)}{a\varepsilon_i + 2c\varepsilon_e} \quad (5.16)$$

These simplifications indicate that the characteristic force plateaus can be easily calculated if the length of each semiaxis is known.

### 5.3 Simplifications for zero membrane conductance

At low frequencies the first plateaus,  $F_{1,a}$  and  $F_{1,c}$  (equations (5.11) and (5.14)) reduce to:

$$F_{1,a} = -\left(\frac{a+2c}{a+c}\right) \quad (5.17)$$

$$F_{1,c} = -\left(\frac{a+2c}{2c}\right) \quad (5.18)$$

for the case of zero membrane conductance. Equations (5.17) and (5.18) represent the negative influential radii of  $a_{\text{infl}}/a$  and  $c_{\text{infl}}/c$ , respectively (see appendix C and compare to Gimsa and Wachner 1999). These simplified equations show that the first plateau depends only on the lengths of semiaxes  $a$  and  $c$  for spheroidal cells with zero membrane conductance.

## 5.4 Simplifications for the cytoplasmic conductivity infinitely higher than the external conductivity

In the medium frequency range, the second plateaus of  $F_{2,a}$  and  $F_{2,c}$  given in equations (5.12) and (5.15) can be simplified to:

$$F_{2,a} = \frac{a + 2c}{c} \quad (5.19)$$

$$F_{2,c} = \frac{a + 2c}{a} \quad (5.20)$$

for a cytoplasmic conductivity infinitely higher than an external conductivity ( $\sigma_i \gg \sigma_e$ ). For a thin disk,  $F_{2,a}$  and  $F_{2,c}$  approach infinity and 1, respectively, whereas  $F_2$  approaches 3 for the spherical shape (Gimsa and Wachner 1999). For a long cylinder,  $F_{2,a}$  and  $F_{2,c}$  approach 2 and infinity, respectively.

## Chapter 6

### Conclusions

Electric field distributions in chip chambers were first analyzed using the finite element programs. The two-dimensional electric field distributions in ER chips using the QuickField were compared to results with the FEMLAB 3.1 finite element program. The results of FEMLAB 3.1 are more precise than QuickField results. Moreover, the FEMLAB 3.1 program can also be applied for complicate structures. Accordingly, the results analyzed by the FEMLAB 3.1 program were selected for optimizing the electrode shape for four-electrode rotation chambers. Torque correction factors provide a basis for characterizing and comparing chips with various electrode shapes. These considerations could specify the electrode-chips with the largest areas of a torque deviation below 10% amongst all considered designs. Amongst the various designs a rounded tip pyramidal electrode was favored. This approach can be a useful tool for other planar designs of central symmetry, like 3, 6, or 8-electrode chambers. Furthermore, three-dimensional electric field distributions in EP and ER chip-chambers were compared using COMSOL 3.3A Multiphysics program. In EP chip-chamber, the electric field strengths near the vicinity of the electrodes and the chamber bottom were inhomogeneous. For ER chip-chamber, homogeneous electric fields were found in the central regions, whereas fields were inhomogeneous near the electrodes.

Simplified equations for influential radii ( $a_{infl}$  and  $c_{infl}$ ) of spheroidal cells avoiding the complicated description by the depolarizing factors were derived. These simplifications apply to the  $\Delta\phi$  induced at the poles of spheroidal cells as well as for the characteristic frequency of membrane polarization,  $f_c$ . The simplified equations can be considered generalized Schwan equations, describing the  $\Delta\phi$  dependence on size and axis ratio for spheroidal cells.

The errors of the simplified equations are a function of cell shape, size, and orientation. The errors also depend on the electric cell properties such as  $\sigma_i$ ,  $\sigma_e$ , but not on  $g_m$  and  $C_m$ . The new equations can also be used to derive simplified equations for the AC-electrokinetic behavior of cells. Furthermore, simplifications for dielectrophoretic force expression were considered for spheroidal cells using the simplified equations of influential radii. The simplified equations of real parts of CMF could also avoid the complicated expressions by the depolarizing factors. The new simple equations for  $F_1$ ,  $F_2$  and  $F_3$  could be analyzed for the limiting shapes of thin disk and long cylinder.

The effects of cell orientation and electric field on the transmembrane potential induced in ellipsoidal cells were also analyzed. Theoretically, the location of the  $\Delta\phi^{\max}$  membrane surface points ( $\alpha$  and  $\beta$ ) depends on cell shape, cell orientations, cell parameters and frequency at this field orientation. It is the first investigation of ellipsoidal cells exposed to an EP field with an orientation of  $45^\circ$ . Theoretical results were confirmed in electroporation experiments. For experimental study, CRBCs were used for comparison of  $\Delta\phi$  of ellipsoidal cells with the theoretical analysis. Electroporation and cell lysis of CRBCs in linear square-wave AC-fields (EP chip chamber) and square-wave rotating fields (ER chip chamber) were studied. Experimental results from both chip chambers showed that PI permeabilization and cell lysis of CRBCs depended on cell orientation, electric field strength, pulse duration and field frequency. Estimations of the critical transmembrane potential  $\Delta\phi_{crit}$  for PI permeabilization were obtained 0.99 V, 0.94 V and 0.89 V in linear fields for different orientation angles of  $\delta = 0^\circ$ ,  $\delta = 45^\circ$  and  $\delta = 90^\circ$ . Whereas,  $\Delta\phi_{crit}$  in rotating fields was 0.79 V. These results indicate rotating fields can easily induce permeabilization. The permeabilization is independent of cell orientation in rotating fields, since these fields scan the membrane surface. The probability of poration of randomly oriented ellipsoidal cells is increased by scanning (Gimsa *et al.* 1992).

Both chip chambers avoid increasing temperatures after pulse application. Furthermore, EP chip chambers can generate different electric fields in one voltage application and can also be used for many cells at a time. In ER chip chambers can



generate only a single field strength in a single voltage application. Only 1-2 cells can be observed in the central area of the ER chip chambers.

In the future, new chips may be developed for electromanipulation of cells or particles in combination with fluidic pump systems as well as for nanotechnology applications.

# Appendix

## Appendix A

### Paper 1:

Maswiwat K, Holtappels M and Gimsa J 2006 On the field distribution in electrorotation chambers-influence of electrode shape. *Electrochimica Acta* **51** 5215-20

Available online at [www.sciencedirect.com](http://www.sciencedirect.com)

SCIENCE @ DIRECT®

Electrochimica Acta 51 (2006) 5215–5220

ELECTROCHIMICA  
*Acta*[www.elsevier.com/locate/electacta](http://www.elsevier.com/locate/electacta)

## On the field distribution in electrorotation chambers—Influence of electrode shape

Kanokkan Maswivat, Moritz Holtappels, Jan Gimsa\*

*University of Rostock, Institute of Biology, Chair of Biophysics, Gertrudenstr. 11A, D-18057 Rostock, Germany*

Received 2 June 2005

Available online 3 May 2006

### Abstract

The electrorotation method can be applied to characterize the passive electric properties of individual cells or particles. For this, their frequency-dependent speed of rotation is registered microscopically. Commonly, object rotation is induced in harmonic rotating fields which are generated in four electrode chambers. The rotation speed of the objects is proportional to the square of the field strength. In this study, we calculated the two-dimensional electric field distribution in electrorotation chips using the FEMLAB finite element program (Comsol, Sweden). For reasons of symmetry, a perfectly circular field is generated at the centers of the four electrode chambers. Nevertheless, the field strength is reduced with respect to the quotient of electrode voltage and distance for any electrode shape. Distant from the center, the field polarization is elliptical with an eccentricity increasing with the distance to the center. For optimizing the electrode shape, the deviations in torques for given distances from the center have been calculated. These deviations have been compared for various electrode shapes in order to find an optimal chip design. Another criterion was a large electrode distance in the corners of the electrode arrangement in order to avoid field hot spots and to minimize dielectrophoretic particle collection.

© 2006 Elsevier Ltd. All rights reserved.

**Keywords:** AC-electrokinetics; Rotating field; Four electrode chamber; Electrode-chips; Torque-distribution

### 1. Introduction

Electrorotation is a common approach to characterize the dielectric properties of individual biological cells and particles by microscopic observation of their frequency-dependent rotation speed [1]. Rotating fields of frequencies ranging from Hz to GHz are commonly generated by four microelectrodes energized by four potentials that are progressively phase shifted by 90°. The frequency spectrum of rotation at a constant field strength can be analyzed to obtain the dielectric properties of the objects, e.g. cells, cell organelles or viruses. The volume of the electrorotation chamber and its electrode shape are important design considerations. For a variety of electrode configurations the field distribution was analyzed by potential measurements in a trough [2] or computer simulations [3–5]. The torque is proportional to the square of the rotating field strength [1,3,5–8]. Refs. [2] and [3] introduced a correction factor for the field strength in

chambers of different electrode designs. Ref. [5] considered the influence of the phase difference between the  $x$  and  $y$  components of the electric field on the torque. The torque depends on the position within the chamber and the electrode geometry [4,5]. This has been demonstrated in experiments with polynomial electrodes [9].

In this study, the distribution of a sinusoidally rotating electric field was calculated for a two-dimensional model using a finite element program. Correction factors were calculated for the electric field strength and the object-torque. Based on these calculations, torques acting on a spherical object at the center and at distant sites within the electrode chamber have been analyzed. The site dependent deviation of the torque from the torque in the center has been compared for various electrode designs in order to find an optimal chip design.

### 2. Method and theory

A rotating electric field generated by two pairs of electrodes orientated perpendicular to each other in the  $x$ - $y$  plane may force polarizable objects, like biological cells, to rotate with the axis

\* Corresponding author. Tel.: +49 381 494 2037; fax: +49 381 494 2039.  
E-mail address: [jan.gimsa@uni-rostock.de](mailto:jan.gimsa@uni-rostock.de) (J. Gimsa).

5216

K. Maswiwat et al. / Electrochimica Acta 51 (2006) 5215–5220

of rotation pointing in the z-direction. The field strength between two opposite electrodes is always influenced by the neighboring electrodes forming the perpendicularly oriented electrode pair. This influence results in a reduced field strength ( $E_0$ ) in the center of the chamber.  $E_0$  is always lower than the field strength calculated for a single pair of plane-parallel electrodes ( $E'_0 = V/d > E_0$ ). The correction factor of the circular field in the center is given by:

$$r = \frac{E_0}{E'_0} \tag{1}$$

Additionally, the rotating field is changing from circular to elliptical outside the center. Generally, the eccentricity of the elliptical field increases with the distance from the center. Especially near the electrodes the field is strongly eccentric. To describe the elliptical fields we used the following simplifying approach. Due to its radial symmetry the chamber can be divided into four pairs of mirror symmetrical slices of which only one has to be examined. The boundaries of these slices are given by four lines crossing the center (Fig. 1A): Two of the lines connecting the electrodes ( $L_c$ ) and two diagonals dividing the inter-electrode gaps ( $L_d$ ). The assumption is made that at a given radius the elliptical fields at the lines  $L_c$  and  $L_d$  provide the limiting cases for the field deviations, i.e. the limits for the range in eccentricity and orientation of the field at any intermediate site of the same radius. Accordingly, the analytical effort

can be reduced to the calculation of the elliptical field along  $L_c$  and  $L_d$ . Further, it is sufficient to calculate the static electric field distributions for two phase angles,  $0^\circ$  and  $45^\circ$ .

For numerical simulation we used FEMLAB (Comsol, Sweden) assuming a sinusoidal driving potentials of  $10 V_{pp}$ . At  $0^\circ$  the field strength was analyzed along the lines  $L_c$  (Fig. 1B). These lines are orientated parallel ( $L_{c||}$ , connecting the positive and negative electrode) and perpendicular ( $L_{c\perp}$ , connecting the electrodes with zero potential) to the field, respectively. The eccentricity of an elliptic field can be derived from the maximum and minimum field strengths  $E_{max}$  and  $E_{min}$  that are orientated perpendicular to one another. To describe the elliptic fields along the  $L_c$  lines at a given distance from the center,  $E_{max}$  and  $E_{min}$  values were combined from the  $L_{c||}$  and the  $L_{c\perp}$  lines, respectively. Analogously, the fields have been analyzed at a phase angle of  $45^\circ$  (Fig. 1C):  $E_{max}$  and  $E_{min}$  have been derived from values taken from the diagonal lines  $L_{d||}$  and  $L_{d\perp}$ , respectively. The relation between the amplitudes of the components of the elliptic and the circular center fields can be described by:

$$E_{max} = \frac{a}{r} E_0 \tag{2}$$

and

$$E_{min} = \frac{b}{r} E_0 \tag{3}$$

(see Fig. 1).

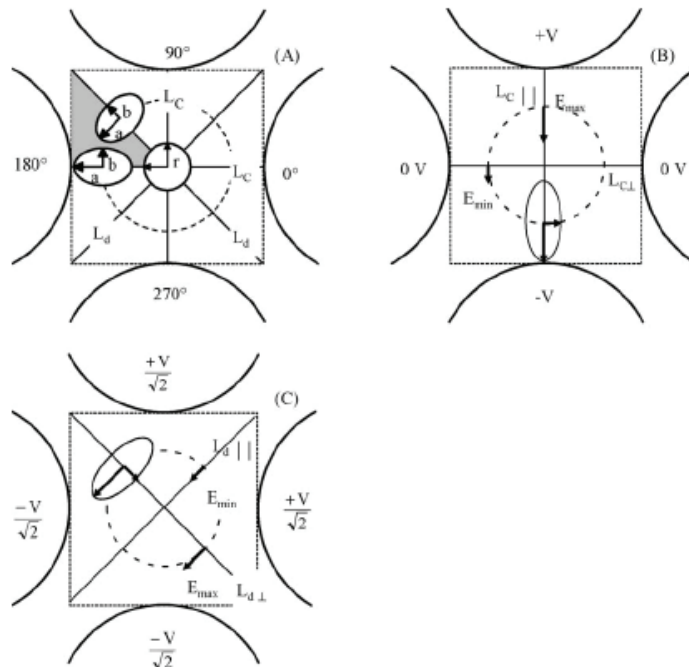


Fig. 1. Scheme of a round tip electrode chip-chamber demonstrating our approach. (A) The rotating field was analyzed along the boundaries  $L_c$  and  $L_d$  of one slice (gray) only. The circular field in the center is described by the correction factor  $r$ . The elliptic fields out of the center are described by the factors  $a$  and  $b$ . With respect to the radius the orientation of the elliptic field is shifted by  $90^\circ$  at two consecutive boundaries of  $L_c$  or  $L_d$ . (B and C) Examples for  $E_{max}$  and  $E_{min}$  at  $0^\circ$ - (B) and  $45^\circ$ -phase (C). Field magnitudes were derived for equal radii (dashed circle).  $E_{max}$  and  $E_{min}$  values were derived along lines  $L_{||}$  and  $L_{\perp}$ .

Table 1  
Parameters of the electrode designs

Shape	Design	Width $D$ ( $\mu\text{m}$ )	Radius $R$ ( $\mu\text{m}$ )
Square	S1	10	–
	S2	75	–
	S3	150	–
	S4	240	–
	S5	300	–
Round	R1	150	75
	R2	240	120
	R3	300	150
	R4	300	240
	R5	300	300
Pointed-pyramidal	P1	–	–
Rounded tip-pyramidal	P2	–	–
Parabolic	P3	–	–

In all cases the tip to tip distance of opposing electrodes was 300  $\mu\text{m}$ .

The eccentricity  $\text{ecc}$  of the field can be calculated from  $a$  and  $b$ :

$$\text{ecc} = \sqrt{1 - \left(\frac{b}{a}\right)^2} \quad (4)$$

The magnitude of the torque  $N_0$  in the circular center field is given by (for details see Appendix A):

$$N_0 = E_0^2 \mathfrak{J}(\alpha) = r^2 E_0^2 \mathfrak{J}(\alpha) \quad (5)$$

where  $r^2$  stands for the torque correction factor and  $\mathfrak{J}(\alpha)$  for the imaginary part of the polarizability of a spherical object with  $\mathfrak{J}(\alpha) = \varepsilon_e \varepsilon_0 V \mathfrak{J}(\text{CMF})$  [1].  $\varepsilon_e$ ,  $\varepsilon_0$ ,  $V$  and  $\text{CMF}$  are external permittivity, volume and the Clausius–Mossotti factor, respectively [1,10,11]. Distant from the center the elliptic field generates the torque  $N_{\text{ellip}}$  (see Appendix A):

$$N_{\text{ellip}} = ab E_0^2 \mathfrak{J}(\alpha) = E_{\text{max}} E_{\text{min}} \mathfrak{J}(\alpha) \quad (6)$$

with the product  $ab$  being the torque correction. Please note that in the center  $ab = r^2$  for  $N_{\text{ellip}} = N_0$ . The deviation of  $N_{\text{ellip}}$ ,  $\Delta N_{\text{ellip}}$  with respect to the torque in the center  $N_0$  is given by:

$$\Delta N_{\text{ellip}} = \frac{N_{\text{ellip}} - N_0}{N_0} \quad (7)$$

In this study, the field properties of 13 different electrode designs have been analyzed. Both, squared and rounded tip electrodes were considered altering the electrode width  $D$  and the electrode tip radius  $R$  (Table 1). Furthermore, we studied pointed pyramidal, rounded tip pyramidal and parabolic electrodes (see also Fig. 2). In all cases, the spacing  $d$  between opposing electrode tips was kept constant at 300  $\mu\text{m}$  (compare to Ref. [11]).

### 3. Results and discussion

#### 3.1. Electric field distribution in the rotation chamber

The electric field distributions for nine different electrode designs are shown in Fig. 2. The direction and magnitude of the electric field depends very much on the location within the

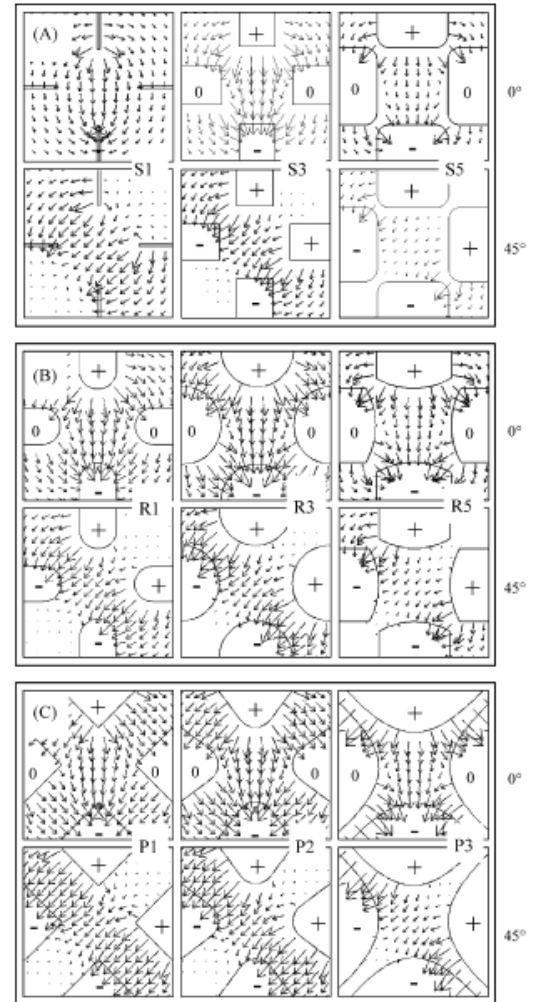


Fig. 2. Electric field strength distribution in the  $x$ - $y$  plane of the electrode chambers at 0°- and 45°-phase, respectively. (A) squared electrodes S1, S3, S5. (B) rounded tip electrode R1, R3, R5. (C) pointed pyramidal, rounded tip pyramidal and parabolic electrodes P1, P2 and P3, respectively. The arrows are electric field strength vectors.

chamber and the electrode design. The field in the central regions is largely homogeneous. In the vicinity of the electrodes the field is highly inhomogeneous.

In Fig. 3, the electric field strength is plotted along the connecting lines  $L_{c\perp}$  and  $L_{c\parallel}$  and along the diagonals  $L_{d\perp}$  and  $L_{d\parallel}$ . From the software the two components of the elliptical field,  $E_{\text{max}}$  and  $E_{\text{min}}$ , can be derived for any radius. At 0°-phase, values of  $E_{\text{max}}$  are found along line  $L_{c\parallel}$ , connecting the positive and negative electrodes. Values of  $E_{\text{min}}$  are found along line  $L_{c\perp}$  connecting the electrodes with zero potential. In contrast, at 45°-phase, maximum and minimum values are found along lines  $L_{d\perp}$  and  $L_{d\parallel}$ , respectively.

5218

K. Maswiwat et al. / Electrochimica Acta 51 (2006) 5215–5220

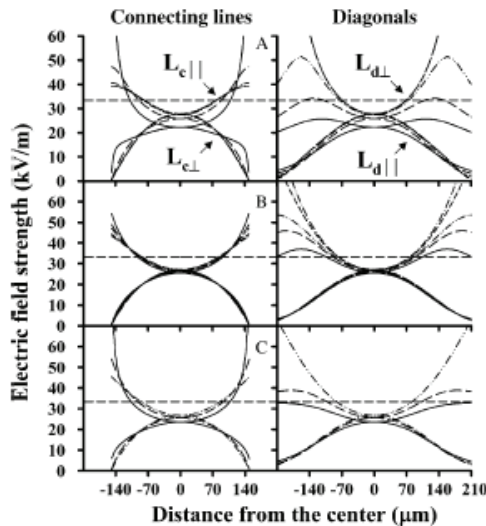


Fig. 3. The electric field strength varies along the connecting lines  $L_{c\perp}$  and  $L_{c\parallel}$  and the two diagonals  $L_{d\perp}$  and  $L_{d\parallel}$  (A) Field strength for the squared electrodes S1 (solid), S2 (long dash), S3 (dash dot-dot), S4 (short dash), and S5 (dash dot). (B) Field strength for the rounded tip electrodes: R1 (solid), R2 (long dash), R3 (dash dot-dot), R4 (short dash) and R5 (dash dot). (C) Field strength for the pointed pyramidal, rounded tip pyramidal and parabolic electrodes: P1 (solid), P2 (long dash) and P3 (dash dot-dot). The field strength of  $E'_0 = V/d = 33.3$  kV/m is marked by the horizontal dashed line.

For most electrode designs the field strength in the center varies between 24 and 28 kV/m, i.e. 72–84% of  $E'_0$ . Only the center field strength of the pin electrode S1 (22 kV/m, 66% of  $E'_0$ ) is noticeably below this value.

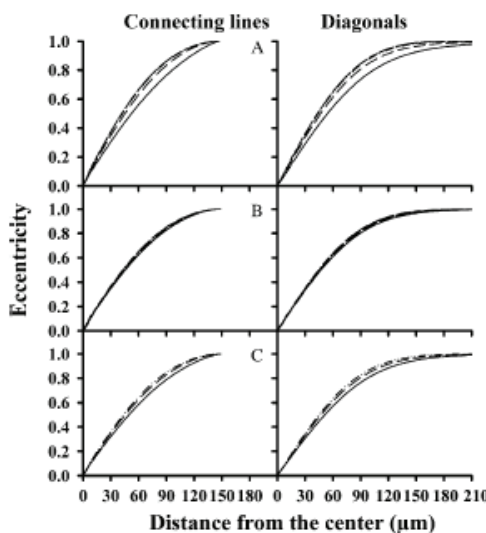


Fig. 4. Field eccentricity as a function of the distance from the center for squared electrodes (A), rounded tip electrodes (B) and pointed pyramidal, rounded tip pyramidal and parabolic electrodes (C). For symbols see Fig. 3.

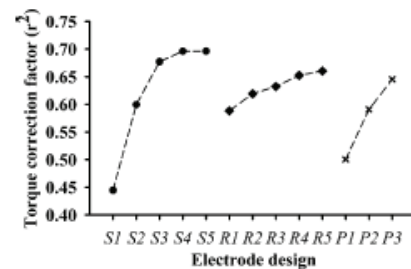


Fig. 5. Torque correction factor  $r^2$  in dependence of the electrode design. Squared electrodes: S1–S5 (●). Rounded tip electrodes R1–R5 (◆). Pointed pyramidal, rounded tip pyramidal and parabolic electrodes: P1, P2 and P3 (×).

For all shapes the field eccentricity increases with the distance from the center (Fig. 4). It varies from 0 (circular field) at the center to about 1 (almost linear AC-field) at the distances of 150 and 210  $\mu\text{m}$  along the connecting and diagonal line, respectively. Nevertheless, especially amongst the rounded-tip electrode designs the eccentricity does not alter significantly.

### 3.2. Torque correction factors

To characterize the circular center field for various designs the torque correction factor  $r^2$  was plotted (Fig. 5). Within the three classes of electrode shapes (S, R and P)  $r^2$  increases clearly with electrode width (see also Table 1 and Fig. 2). In the sequence of the square electrodes (S)  $r^2$  approaches a plateau at about 0.7 that is not matched by any other design.

The torque deviation inside the measuring volume of the chamber is the most important characteristics for the usability

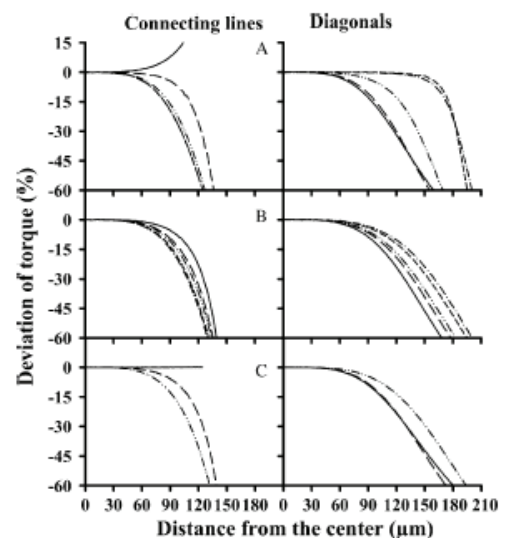


Fig. 6. Deviation of torque along connecting lines and diagonals as a function of distance from the center. (A) squared electrodes. (B) rounded tip electrodes. (C) pointed pyramidal, rounded tip pyramidal and parabolic electrodes. For symbols see Fig. 3.

Table 2  
Torque correction factor  $r^2$  and distance from the center for a torque deviation of 10% ( $S_{10\%}$ ) for different electrode designs

Designs	$r^2$	$S_{10\%}$ ( $\mu\text{m}$ )	
		Connecting lines	Diagonals
S1	0.44	95	84
S2	0.60	104	88
S3	0.68	79	114
S4	0.70	75	171
S5	0.70	75	167
R1	0.59	103	93
R2	0.62	91	100
R3	0.63	88	104
R4	0.65	83	114
R5	0.66	82	119
P1	0.50	147	93
P2	0.59	103	95
P3	0.64	86	110

of a rotation chamber. For a chip chamber the area with comparable torques limits the useable area or the size of larger cells. For comparison purposes we allowed for torque deviations of up to 10%, resulting in the specific radius distance  $S_{10\%}$ . In all cases  $S_{10\%}$  was at least  $75 \mu\text{m}$  (Fig. 6 and Table 2).

A summary of the electrode properties is given in Table 2. At first sight,  $r^2$  as well as  $S_{10\%}$  are similar amongst the rounded tip, rounded tip pyramidal and parabolic electrode designs whereas squared electrodes and pointed pyramidal show higher differences in  $S_{10\%}$  along the connecting and diagonal lines. Although  $S_{10\%}$  along the diagonals for squared electrodes is very high we found these electrodes less appropriate since the low  $S_{10\%}$  along the connecting line is limiting the useable chip area. Additionally, square electrodes generate extremely high field strengths at their sharp edges. This may lead to particle collection at the edges due to dielectrophoretic effects. Amongst all electrodes a maximum area of constant torque is found for the design P2. In this design  $S_{10\%}$  i.e. the radius of the usable area is at least  $95 \mu\text{m}$ .

#### 4. Conclusion

Our study demonstrates that numerical simulations of static electric fields combined with a simple analytical post-processing yields valuable information on the fidelity of rotating fields in electrorotation chip chambers. Torque correction factors provide a basis for characterizing and comparing various electrode shapes. They are vital for the interpretation of experimental data. We found that the maximum torque in the center of four-electrode rotation chambers will never exceed 70% of the torque  $N'_0$  in between a single pair of equiplanar electrodes. Furthermore, we could estimate the torque deviations that would be experienced by a spherical object at different radii from the center of a chip. These deviations depend on the electrode design. Amongst the various designs we favor a rounded tip pyramidal electrode (see P2 in Table 2 and Fig. 2) that introduces a slight improvement in comparison to our earlier design (R3 in Table 2 and Fig. 2; [11]). Nevertheless, there is a number of alternative

designs that have not been considered in this study. Therefore, our approach might be a useful tool in the continuing search for improved electrode designs. It can analogously applied to different electrode arrangements, e.g. 3, 6 or 8 electrode chambers. These electrode arrangements may not only be applied in electrorotation characterization chambers but also in micro-fluidic or lab-on-chip devices.

#### Acknowledgments

K.M. is grateful for a stipend of the Royal Thai government. This study has partly been supported by grant StSch 20020418A of the Bundesamt für Strahlenschutz to J.G. The authors are grateful to the International Postgraduate Programme (IPP) at the University of Rostock supported by DAAD, BMBF and DFG. The authors would like to thank Robert Sleight for his help with the manuscript.

#### Appendix A. Torques acting on objects at different sites of the measuring area

The time-averaged torque  $\langle \vec{N} \rangle$  in circular polarized fields is given by the cross-product of the induced dipole moment ( $\vec{m}$ ) and the conjugated field ( $\vec{E}^*$ ) [1,10]:

$$\langle \vec{N} \rangle = \frac{1}{2} \Re[\vec{m} \times \vec{E}^*] \quad (\text{A.1})$$

In component notation, the elliptical AC field in the  $x$ - $y$  plane can be written as (see Fig. 1A, Eqs. (2) and (3)):

$$\vec{E} = \begin{pmatrix} E_x \\ E_y \\ E_z \end{pmatrix} = \begin{pmatrix} (a/r)E_0 \\ (jb/r)E_0 \\ 0 \end{pmatrix} = \begin{pmatrix} E_{\max} \\ E_{\min} \\ 0 \end{pmatrix} \quad (\text{A.2})$$

Both, the  $x$ - and  $y$ -field components are sinusoidal with a  $90^\circ$ -phase shift. This phase shift is denoted by  $j = \sqrt{-1}$ . With no limitation in generality we assume that the magnitude field component oriented in  $\hat{i}$ -direction is larger than in  $\hat{j}$ -direction. For the elliptic field distant from the center, factors  $a$  and  $b$  were introduced leading to (see Eqs. (2) and (3)):

$$E_{\min} = j \frac{b}{a} E_{\max} \quad (\text{A.3})$$

and the conjugated fields:

$$E_{\min}^* = -j \frac{b}{a} E_{\max}^* \quad (\text{A.4})$$

The induced dipole moment  $\vec{m}$  is proportional to the field. In component notation  $\vec{m}$  is given by [1]:

$$\vec{m} = (m_x \ m_y \ m_z) = (\alpha E_{\max} \ \alpha E_{\min} \ 0) \quad (\text{A.5})$$

No  $z$ -component is induced. Introducing Eqs. (A.2) and (A.5) for the elliptic field the torque (Eq. (A.1)) becomes:

$$\langle \vec{N} \rangle = \frac{1}{2} \Re(\alpha E_{\max} E_{\min}^* - \alpha E_{\min} E_{\max}^*) \hat{k} \quad (\text{A.6})$$

5220

*K. Maswiwat et al. / Electrochimica Acta 51 (2006) 5215–5220*

where  $\hat{k}$  stands for the unit vector pointing in  $z$ -direction. Using Eq. (A.4) we obtain:

$$\langle \vec{N} \rangle = \left( \frac{ab}{r^2} \right) E_0^2 \Re(-j\alpha) \hat{k} = \left( \frac{ab}{r^2} \right) E_0^2 \Im(\alpha) \hat{k} \quad (\text{A.7})$$

Accordingly, the torque in the elliptic field is:

$$\langle \vec{N} \rangle = E_{\max} E_{\min} \Im(\alpha) \hat{k} \quad (\text{A.8})$$

resulting in the well known expression for the torque in a circular field ( $r = a = b$ ):

$$\langle \vec{N} \rangle = E_0^2 \Im(\alpha) \hat{k} \quad (\text{A.9})$$

### References

- [1] J. Gimsa, *Bioelectrochemistry* 54 (2001) 23.
- [2] J. Gimsa, R. Glaser, G. Fuhr, *Studia Biophys.* 125 (1988) 71.
- [3] R. Hölzel, *J. Phys. D: Appl. Phys.* 26 (1993) 2112.
- [4] M.P. Hughes, *Phys. Med. Biol.* 43 (1998) 3639.
- [5] M.P. Hughes, X.-B. Wang, F.F. Becker, P.R.C. Gascoyne, R. Pethig, *J. Phys. D: Appl. Phys.* 27 (1994) 1564.
- [6] J. Gimsa, R. Glaser, G. Fuhr, in: W. Schütt, H. Klinkmann, I. Lamprecht, T. Wilson (Eds.), *Physical Characterization of Biological Cells*, Verlag Gesundheit GmbH, Berlin, 1991, p. 295.
- [7] A. Lampa, *Wiener Berichte* 15 (2a) (1906) 1659.
- [8] H.P. Schwan, *Ferroelectrics* 86 (1988) 205.
- [9] M.P. Hughes, S. Archer, H. Morgan, *J. Phys. D: Appl. Phys.* 32 (1999) 1548.
- [10] T.B. Jones, *Electromechanics of Particles*, Cambridge University Press, USA, 1995.
- [11] J. Sudsiri, D. Wachner, J. Gimsa, *Bioelectrochemistry*, in press.



## **Appendix B**

### **Paper 2:**

Maswiwat K, Holtappels M and Gimsa J 2007a  
Optimizing the electrode shape for four-electrode  
electrorotation chips. *ScienceAsia* **33** 61-7

## RESEARCH ARTICLE

ScienceAsia 33 (2007): 61-67

doi: 10.2306/scienceasia1613-1874.2007.33.061

## Optimizing the Electrode Shape for Four-electrode Electrorotation Chips

Kanokkan Maswiwat<sup>2</sup>, Moritz Holtappels<sup>1</sup> and Jan Gimsa<sup>1\*</sup><sup>1</sup> Institute of Biology, University of Rostock, Gerttudenstr. 11A, 18051 Rostock, Germany.<sup>2</sup> On leave from Department of Physics, Suratthani Rajabhat University, Amphur Muang, Suratthani 84100, Thailand.

\* Corresponding author, E-mail: jan.gimsa@uni-rostock.de

Received 6 Mar 2006

Accepted 26 Jul 2006

**ABSTRACT:** Electrorotation experiments are conducted in harmonic rotating fields to characterize the passive electric properties of cells or particles by their frequency-dependent rotation speed. The torque of the objects is proportional to the square of the field strength. Therefore, a rotating field of constant amplitude is desirable over a large area of the measuring chamber for reproducible measurements. In this study, the field distribution in chip chambers was analyzed using numerical field simulation in combination with analytical post-processing. The electric field distribution was compared for various electrode shapes. For the center, correction factors could be calculated, relating the actual field strength to the quotient of electrode voltage and distance. Apart from the center, the field was elliptically polarized with an eccentricity increasing with the distance from the center. A spherical model object has been assumed to derive a theoretical expression for the torque induced by an elliptical field. This model allowed us to consider the torque deviation for each site with respect to the torque induced by the circular center-field. Various electrode shapes have been checked for minimum deviations of the torque. We found the optimal chip design for electrorotation to feature electrodes with round tips.

**KEYWORDS:** rotating fields, four-electrode chambers, electrode design, torque, cell chip.

### INTRODUCTION

Electrorotation is a common technique to characterize the dielectric properties of individual cells in rotating electric fields <sup>1,4</sup>. Cell properties can be deduced from the microscopic observation of the frequency dependence of the rotation speed induced by a rotating electric field in the frequency range from Hz to GHz. The torque leading to cell rotation is generated by the interaction of the induced cellular dipole moment with the inducing external field. Nevertheless, only the out-of-phase component of the dipole moment will contribute to the torque that is given by the cross product of the dipole moment with the external field. Mathematically, the out-of-phase component of the induced dipole is identical to its imaginary part that is different from zero only at field frequencies where electric dispersions occur. It follows that the method of electrorotation directly and sensitively detects dispersion processes, like structural (Maxwell-Wagner) and molecular (Debye) dispersions <sup>2,3</sup>. The line of arguments suggests that a rotating electric field polarizing a cell translates the temporal phase shift of the induced dipole moment that would be observed in a linear field into a spatial shift leading to

cell rotation.

In classical oscilloscopes, a beam rotation, i.e. a Lissajous-circle, is generated by co-sinusoidal and sinusoidal fields applied to two electrode pairs for the x- and y-deflections. The x- and y-electrode pairs are consecutively arranged to avoid interference. Consecutive electrodes cannot be applied in electrorotation, where the field rotates in the electrode-chip plane. In four-electrode electrorotation chips, two electrode pairs simultaneously generate the two field components. As a consequence, interference has to be taken into account. It is interesting that an analogous problem exists in accelerators where the particle beam is confined by electrostatic quadrupole electrodes that are arranged around the beam-path. Optimization of their design started with complex shapes <sup>7</sup> and led to four rotational rods with their symmetry axes oriented parallel to the path <sup>8</sup>. In the central region of the electrodes the description may be reduced to two dimensions, i.e. a plane oriented perpendicular to the beam where the accelerator-electrodes are mimicking the design of an electrorotation chip.

In electrorotation, four-electrode micro-chambers are common. To generate rotating fields, the electrodes

are driven by four sinusoidal or square-wave signals that are progressively phase-shifted by  $90^\circ$ . In the frequency range used for cell characterization, the electrode properties can be assumed to be linear, i.e. no frequency components other than those applied at the electrodes can evolve in the chamber. As a result, only elliptically polarized fields can be generated. The frequency spectrum of cell rotation at a frequency-independent field strengths can be analyzed to obtain dielectric properties of biological cells. For electrorotation chambers the electrode shape is an important design feature.

For a variety of electrode configurations the field distribution was analyzed by computer simulations<sup>7-10</sup>. The torque is proportional to the square of the rotating field strength<sup>1,8,10,11,12</sup>. Gimsa et al.<sup>7</sup> and Hölzel<sup>8</sup> introduced correction factors for the field strength in chambers of different electrode designs. Hughes et al.<sup>10</sup> considered the influence of the phase difference between the  $x$  and  $y$  components of the electric field on the torque. The torque depends on the position within the electrode chamber and the geometry of the electrodes<sup>9,10,13</sup>.

In this study, we consider a sinusoidally rotating electric field in a two-dimensional chip-model for various electrode shapes using the finite element program QuickField (Tera Analysis Ltd., Denmark). The program is freely available under <http://www.quickfield.com/free.htm>. Correction factors for the various electrodes shapes were calculated for the field strength and the torque experienced by the cells. Based on these calculations; torques, acting on a spherical object at the center of chambers of different electrode designs, have been compared. For each design, the deviations of the torques relative to the distance from the center, have also been analyzed.

## METHODS AND THEORY

A rotating electric field can be generated by two pairs of opposing electrodes orientated perpendicular to each other in the  $x$ - $y$  plane. To generate a monochromatic, circular field the two pairs must be driven by co-sinusoidal and sinusoidal fields, respectively. As a result, the center-field rotates at a constant amplitude (field strength). Nevertheless, its actual amplitude can not directly be derived. Firstly, the amplitude depends on the electrode shapes. Secondly, the field strength between a pair of electrodes is also influenced by the other electrode pair of the four-electrode setup. These effects result in a reduced center field strength ( $E_0$ ) deviating from the field strength calculated for a single pair of plane-parallel electrodes ( $E'_0 = V/d > E_0$ ). We define the correction

factor of the circular field in the center as:

$$r = \frac{E_0}{E'_0} \quad (1)$$

Special cases for the chamber-field can be derived from the temporal behavior of the co-sine- and sine-functions: When one of the functions reaches its positive or negative maximum, the other is at zero amplitude. In these cases, the center field will be aligned with lines connecting ( $L_c$ ) the tips of opposing electrodes, i.e. the center field vector will consecutively point at the tips of the four electrodes during one cycle (compare to Fig. 1A). The center field will be aligned with the two diagonal lines ( $L_d$ ) passing in between the electrodes when the absolute values of the functions are equal (Fig. 1B). The arrow head of the field vector will describe a perfect circle when its origin is located at the center of the four-electrode chamber, for reason of symmetry. In and out of the center, the rotating field is changing from a circular to an elliptical polarization, respectively. Accordingly, the arrow heads of the field vectors will describe ellipses. When the vector-origins are located at the connecting or diagonal lines the orientations of the semi-axes of these ellipses are known: the semi-axes are aligned in parallel and perpendicular to the connecting or diagonal lines. The eccentricity of the elliptical field increases with the distance from the center.

To describe the elliptical fields we used the following simplified approach. The static electric field distributions for two phase angles,  $0^\circ$  and  $45^\circ$ , was calculated by numerical simulation with QuickField (Tera Analysis Ltd., Denmark) assuming a driving potential of 10 Vpp at an electrode tip-to-tip distance of 300  $\mu\text{m}$ . The results were rescaled to 300  $\mu\text{m}$ . At  $0^\circ$  the field strength was analyzed along the electrode tip-connecting lines  $L_c$ . These lines are orientated parallel ( $L_{c\parallel}$ , horizontal line in Fig. 1A connecting the positive and negative electrode) and perpendicular ( $L_{c\perp}$ , vertical line in Fig. 1A connecting the electrodes with zero potential) to the field. The eccentricity of an elliptical field can be derived from the maximum and minimum field strengths  $E_{\max}$  and  $E_{\min}$ , e. g. at the crossing points of  $L_{c\parallel}$  and  $L_{c\perp}$  with the inner circle, respectively (Fig. 1A). Since a  $90^\circ$  rotation of the chamber corresponds to a  $90^\circ$  phase progression of the field both values can be extracted from a single calculation.  $E_{\max}$  and  $E_{\min}$  determine the semi-axes of the ellipses described by the circulating vector arrow head. The analogous procedure was applied to determine  $E_{\max}$  and  $E_{\min}$  at the crossing points of the diagonal lines for a phase angle of  $45^\circ$  (Fig. 1B).  $E_{\max}$  and  $E_{\min}$  have been derived from values taken from the cross-points of the diagonal lines  $L_{d\parallel}$  and  $L_{d\perp}$  with the inner circle. As a result the field is

fully characterized at 8 points of the inner circle (Fig. 1). At the inner circle the  $L_c$ - and  $L_d$ -crossing points correspond to the shortest and the longest distances to the electrodes, respectively. Therefore, it can be assumed that the  $E_{max}$  and  $E_{min}$  values of the elliptical fields at all other points of the circle will be in between the values at these points.

The relationship between an elliptical field and the circular field in the center can be described by:

$$E_{max} = \frac{a}{r} E_0 \quad (2)$$

and

$$E_{min} = \frac{b}{r} E_0 \quad (3)$$

where a and b stand for the correction factors of

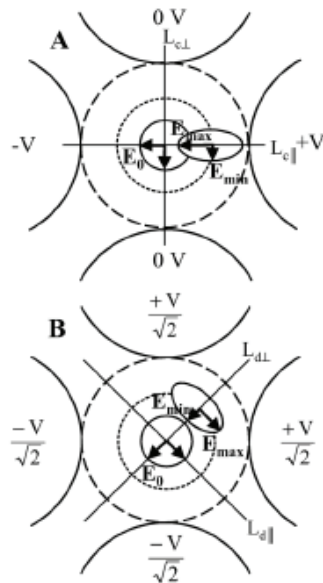


Fig 1. Sketch explaining the method of data acquisition for a chip-chamber with 300 μm electrode spacing. The long-dashed line marks the inner electrode circle with a radius of 150 μm as the reference area (see text and Table 1). The circular field in the center is described by  $E_0$ . The elliptical fields out of the center are described by  $E_{max}$  and  $E_{min}$ . Examples for  $E_{max}$  and  $E_{min}$  at 0°- (A) and 45°-phases (B) are given (please compare to Fig.2). Plotted values were derived for a distance of 100 μm from the center (short-dashed inner circle). A:  $E_{max}$  and  $E_{min}$  values were derived from the crossing points of the horizontal ( $L_c$ ) and vertical electrode tip-connecting lines ( $L_d$ ) with the inner circle (note that  $\parallel$  and  $\perp$  refer to the line orientation with respect to the field). B:  $E_{max}$  and  $E_{min}$  values were derived from the crossing points of diagonals  $L_{d1}$  and  $L_{d2}$ , respectively.

the two components of the elliptical field.

Furthermore, the eccentricity (ecc) of the elliptical field is calculated using the correction factors a and b:

$$ecc = \sqrt{1 - (b/a)^2} \quad (4)$$

Analogous to the field correction factor r it is reasonable to introduce a torque correction factor that relates  $E_0$  to the torque  $\langle N_0 \rangle$  in the center of the chamber (for details see Appendix). Thus, the magnitude of the torque  $\langle N_0 \rangle$  in the circular center field is described by:

$$\langle N_0 \rangle = r^2 E_0^2 \text{Im}(\alpha) \quad (5)$$

where  $r^2$  stands for the torque correction factor and  $\text{Im}(\alpha)$  for the imaginary part of the polarizability of a spherical object with  $\text{Im}(\alpha) = \epsilon \epsilon_0 V \text{Im}(\text{CMF})^0 \cdot \epsilon \epsilon_0$ , V and CMF are external permittivity, volume and the Clausius Mossotti factor, respectively.

Distant from the center we find the torque  $\langle N_{dhp} \rangle$ :

$$\langle N_{dhp} \rangle = ab E_0^2 \text{Im}(\alpha) = E_{max} E_{min} \text{Im}(\alpha) \quad (6)$$

with a torque correction factor of ab. Please note that in the center  $ab = r^2$  for  $\langle N_{dhp} \rangle = \langle N_0 \rangle$ . The deviation of  $\langle N_{dhp} \rangle$ ,  $\Delta N_{dhp}$  referring to the center-torque  $\langle N_0 \rangle$  is given by:

$$\Delta N_{dhp} = \frac{\langle N_{dhp} \rangle - \langle N_0 \rangle}{\langle N_0 \rangle} \quad (7)$$

We analyzed the field properties of 12 different electrode designs with squared and rounded tips by a stepwise change of electrode width D and electrode tip radius R (Table 1). The spacing d between the opposing electrode tips was kept constant at 300 μm.

## RESULTS AND DISCUSSION

### Electric field distribution in the rotation chamber

The field distributions for 6 different electrode designs are shown in Fig. 2. The field properties depend very much on the location within the chamber and electrode design. The field vectors in the central regions are generally homogeneous. From A to B Fig. 1 describes an anticlockwise rotation.

The electric field strength along the connecting lines  $L_{c1}$  and  $L_{c2}$  and along the diagonals  $L_{d1}$  and  $L_{d2}$  is plotted in Fig. 3 (please note, that Figs. 4A and B are zoom-plots of Figs. 3A and C). For any distance from the center the two components of the elliptical field,  $E_{max}$  and  $E_{min}$ , were derived along the  $L_c$  and  $L_d$  lines. At phase 0° values of  $E_{max}$  were found along line  $L_{c1}$ . Values

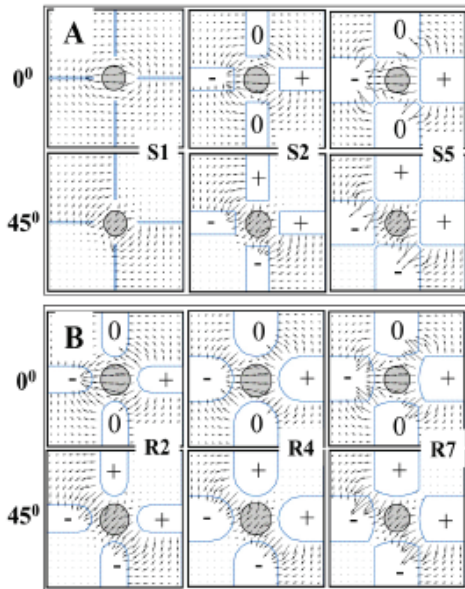


Fig 2. Distribution of the electric field strength in the x-y plane of different electrode chambers (Table 1) driven by 0°- and 45°- phase signals. **A**: squared electrodes S1, S2 and S5. **B**: rounded tip electrodes R2, R4 and R7. The arrows are vectors of the electric field strength. The circular areas with torque deviations below 10% are marked in gray. Their radii were determined from the minima of the  $S_{10\%}$ -values along the connecting and diagonal lines marked by an asterisk in Table 1.

of  $E_{min}$  were found along line  $L_{c1}$ . At phase 45°,  $E_{max}$  and  $E_{min}$  values were found along lines  $L_{d1}$  and  $L_{d2}$ , respectively.

For all electrode designs the field strength in the center varies between 24 and 28 kV/m, i.e. 73% - 84% of  $E_0$ . Distant from the center, the performance of the square- and round-tipped electrodes is qualitatively different. There, the field strength for squared electrodes is either below (at line  $L_{c1}$ ) or above (at line  $L_{d1}$ ) the field strength of the round-tip electrodes. For both shapes the field eccentricity increases with the distance from the center. It varies from 0 (circular field) at the center to about 0.95 (extremely flattened ellipse) at a distance of 120  $\mu\text{m}$  (Fig. 5). The increasing eccentricity seems to be independent from the electrode design. Only square-tipped electrodes (Fig. 5B) show different eccentricities along the diagonal lines  $L_{d1}$ .

**Torque correction factors at the center and at sites distant from the center**

The field strengths at the center of various rotation chambers are related to the torque correction factor  $r^2$  that is presented in relation to the electrode

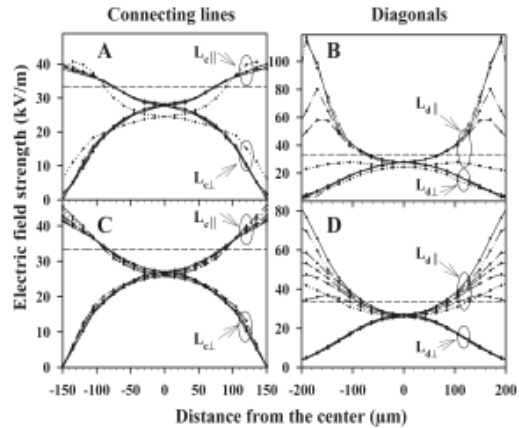


Fig 3. Field strength variation along the connecting lines  $L_{c1}$  and  $L_{c2}$  and the two diagonals  $L_{d1}$  and  $L_{d2}$ . **A** and **B** show the electric field strength for the squared electrodes: S1 (dot), S2 (short dash), S3 (dash dot), S4 (dash dot-dot), and S5 (solid). **C** and **D** show the electric field strength of the rounded tip electrodes: R1 (medium dash), R2 (dot), R3 (long dash), R4 (short dash), R5 (dash dot), R6 (dash dot-dot) and R7 (solid). The straight-dashed line marks the field strength of  $E_0=33.3$  kV/m that would be observed in between a pair of plane parallel electrodes.

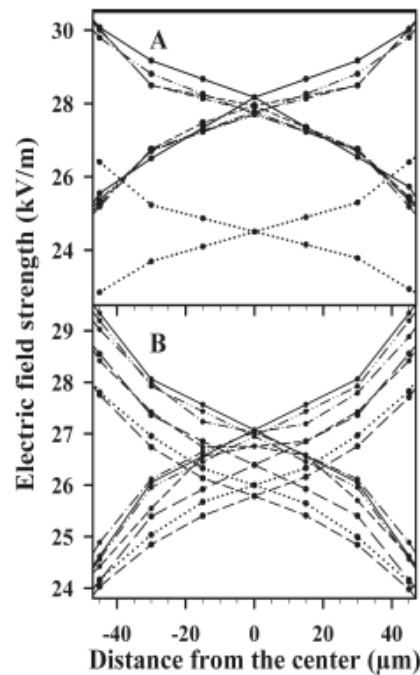


Fig 4. **A**: Zoom of Fig. 3A, **B**: zoom of Fig. 3C. For symbols see Fig. 3.

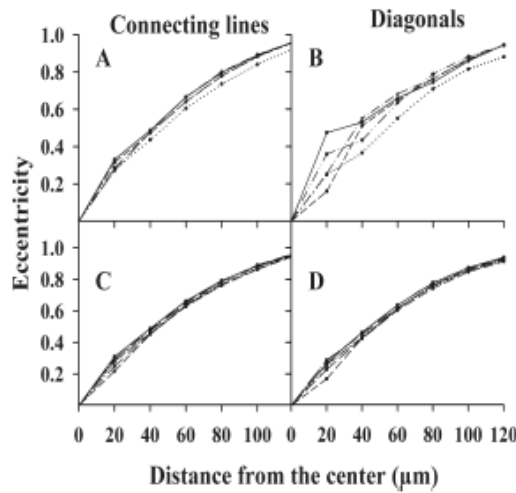


Fig 5. The eccentricity of the electric field as a function of the distance from the center for squared electrodes (A and B) and rounded tip electrodes (C and D). For symbols see Fig. 3.

characteristics  $D/d$  and  $R/d$  in Table 1. For  $r^2$  a maximum in the range from 66% to 71% of  $N'_0$  was found for ratios of  $D/d$  and  $R/d$  above 0.5. Above these ratios  $r^2$  remains fairly constant and a change in electrode width does not further affect the center field whereas  $r^2$  decreases for ratios below 0.5. For the pin electrodes (S1)  $r^2$  is smallest. Comparing the round- and square-tipped electrodes with a ratio above 0.5, the latter show slightly higher values for  $r^2$ .

An important criterion for the usability of an electrorotation chamber is the torque deviation inside the measuring volume of the chamber. In a plane chip this volume is confined to an area with comparable torques. We defined circular areas by allowing for a torque deviation up to 10% with respect to the torque in the center. Along the  $L_c$  and  $L_d$ -lines  $S_{10\%}$ -distances were defined by the points with a torque-deviation of 10%. The radius of the experimentally usable area was

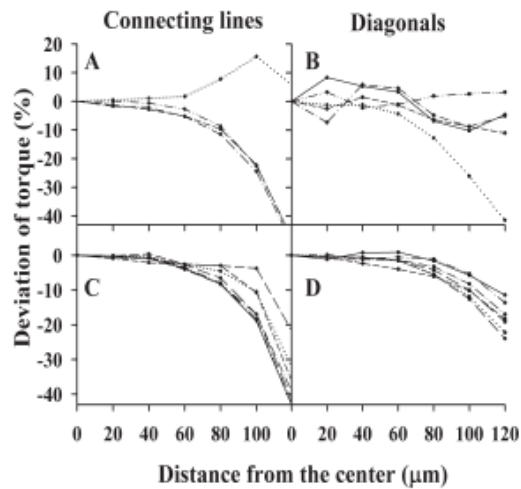


Fig 6. Distance dependence of the torque deviation along connecting lines and diagonals. A and B: squared electrodes. C and D: rounded tip electrodes. For symbols see Fig. 3.

Table 1. Designs of various electrode chambers. For all chambers the spacing  $d$  between the electrode tips was 300 μm. Electrode characteristics  $D/d$  and  $R/d$  ( $D$ ,  $R$  and  $d$  stand for electrode width, electrode tip radius and spacing between electrodes, respectively), torque correction factor  $r^2$  and distance from the center at which the torque reaches a deviation of 10% ( $S_{10\%}$ ) along the connecting and diagonal lines. The last column presents the relative area with respect to the inner electrode circle with a radius of 150 μm (see Fig.1) inside which the torque deviation is below 10%. The circular areas were determined from the minima of the  $S_{10\%}$ -values along the connecting lines ( $L_c$ ) and the diagonals ( $L_d$ ) marked by an asterisk (see Fig. 2).

Shape	Designs	Width D (μm)	Radius R (μm)	D/d(squared electrodes) R/d(rounded tip electrodes)	$r^2$	$S_{10\%}$ in μm		% of usable area
						$L_c$	$L_d$	
Square	S1	10	-	0.03	0.54	84	76*	25.67
	S2	150	-	0.5	0.71	80.5*	110	28.80
	S3	180	-	0.6	0.70	77*	>120	26.35
	S4	240	-	0.8	0.69	82*	>120	29.88
	S5	300	-	1.0	0.71	77.5*	>120	26.69
Round	R1	150	75	0.25	0.60	108	93*	38.44
	R2	180	90	0.3	0.61	99	94*	39.27
	R3	240	120	0.4	0.63	88*	100	34.41
	<b>R4</b>	<b>300</b>	<b>150</b>	<b>0.5</b>	<b>0.65</b>	<b>99*</b>	<b>99*</b>	<b>43.56</b>
	R5	300	180	0.6	0.66	85*	104	32.11
	R6	300	240	0.8	0.65	85*	112	32.11
	R7	300	300	1.0	0.66	84*	115	31.36

calculated from the minimum of the two  $S_{10\%}$ -distances. The results are given in Table 1 and displayed by the grayish circles in Fig. 2. For all electrode designs the minimum of the  $S_{10\%}$ -distances was at least  $75\ \mu\text{m}$  (Fig. 6). With the exception of electrode design S1,  $S_{10\%}$  along the diagonal lines (Figs. 6B and D) was always larger ( $90\text{--}100\ \mu\text{m}$ ) than  $S_{10\%}$  along the connecting lines (around  $80\ \mu\text{m}$ , Figs. 6A and C). Furthermore, the torque for the square-tipped electrodes shows an undulating pattern (Fig. 6B) contrasting the obvious decrease of torque of the round-tipped electrodes (Fig. 6D). Nevertheless, we believe that the undulations result from the limited capacity of the software.

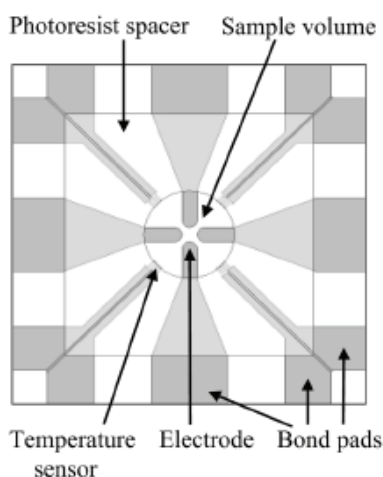


Fig 7. Scheme of our new glass electrorotation chips with platinum electrodes of design R4. The radius of the electrode tip is  $150\ \mu\text{m}$ . The width of the electrode and the spacing are  $300\ \mu\text{m}$ . Temperature sensors have been processed from a platinum meander-structure to follow temperature changes in the chamber. A photoresist structure forms the side walls limiting the sample volume that is confined by a cover slip during measurements.

A summary of the electrode properties is given in Table 1. At first sight,  $r^2$  as well as  $S_{10\%}$  are similar amongst the round-tipped electrode designs, whereas the square-tipped electrodes show higher differences in  $S_{10\%}$  along the connecting and diagonal lines. Although  $S_{10\%}$  along the diagonal lines for the square-tipped electrodes is very high, these electrodes are less appropriate since the low  $S_{10\%}$  along the connecting line is limiting the useable chip area. Additionally, the square-tipped electrodes generate extremely high field strengths at their sharp edges. This may lead to particle collection at the edges due to dielectrophoretic effects. Amongst the round-tipped electrodes, a maximum area of constant torque is found for the design R4. In this

design  $S_{10\%}$  is about  $100\ \mu\text{m}$  along both the connecting and diagonal lines. Therefore, out of 12 analyzed electrode designs, R4 was chosen for use in the new chip designs (Fig. 7, produced by GeSiM GmbH, Grosserkmannsdorf, Germany).

## CONCLUSION

Numerical simulations with a freely available software for electrostatic fields yields valuable information on the quality of rotating fields in electrorotation chip-chambers when combined with a simple analytical post-processing. The field strength and torque correction factors introduced provide a basis for comparing experimental results obtained with chambers of different electrode designs. The maximum field strength in the center of 4-electrode rotation chambers never exceeds 85% of the field strength generated by a single pair of equi-planar electrodes. Furthermore, we could determine the site dependence of the torques experienced by spherical objects within the electrorotation-chips. These considerations allowed us to specify the electrode-chips with the largest areas of a torque deviation below 10% amongst all considered designs. It has a round-tipped electrode with  $R/d = 0.5$ . There are a number of alternative electrode shapes that have not been considered in this study such as pyramidal or hyperbolic shapes. Furthermore, this approach can be a useful tool not only for planar 4-electrode chambers but also for other planar designs of central symmetry, like 3, 6, or 8-electrode chambers. Probably, it can also be applied in 3-dimensional designs like those used in micro-fluidic lab-on-chip devices.

## ACKNOWLEDGMENTS

K.M. is grateful for a stipend from the Royal Thai government. Dr. H.-W. Glock and D. Wachner are acknowledged for helpful discussions. This study has partly been supported by grant StSch 20020418A of the Bundesamt für Strahlenschutz to J.G. The authors are grateful to the International Postgraduate Programmes (IPP) supported by DAAD, BMBF and DFG.

## REFERENCES

1. Gimsa J, Glaser R and Fuhr G (1991) Theory and application of the rotation of biological cells in rotating electric fields (Electrorotation). In: *Physical characterization of biological cells* (Edited by Schütt W, Klinkmann H, Lamprecht I and Wilson T), pp 295-323. Verlag Gesundheit GmbH, Berlin.
2. Gimsa J (2001) A comprehensive approach to electro-orientation, electrodeformation, dielectrophoresis, and electrorotation of ellipsoidal particles and biological cells. *Bioelectrochem* 54, 23-31.

3. Jones TB (1995) *Electromechanics of particles*. Cambridge University Press, USA.
4. Gimsa J, Müller T, Schelle T and Fuhr G (1996) Dielectric spectroscopy of single human erythrocytes at physiological ionic strength: Dispersion of the cytoplasm. *Biophys J* **71**, 495-506.
5. Stokes RH, Crandall KR, Stovall JE and Swenson DA (1979) RF Quadrupole Beam Dynamics. *IEEE Trans Nuc Sci* **NS26**, 3469-79.
6. Junior P, Deitinghoff H, Halfmann KD, Neumann W and Zoubek N (1983) Design Considerations on Peak Electrical Fields and Maximum Beam Currents for Heavy Ion RFQ Linacs. *IEEE Trans Nuc Sci* **NS30**, 2639-41.
7. Gimsa J, Glaser R and Fuhr G (1988) Remarks on the field distribution in four electrode chambers for electrorotational measurements. *Studia biophysica* **125**, 71-6.
8. Hölzel R (1993) Electric field calculation for electrorotation electrodes. *J Phys D: Appl Phys* **26**, 2112-6.
9. Hughes MP (1998) Computer-aided analysis of conditions for optimizing practical electrorotation. *Phys Med Biol* **43**, 3639-48.
10. Hughes MP, Wang X-B, Becker FF, Gascoyne PRC and Pethig R (1994) Computer-aided analyses of electric fields used in electrorotation studies. *J Phys D: Appl Phys* **27**, 1564-70.
11. Lampa A (1906) Über Rotation im elektrostatischen Drehfelde. *Wiener Berichte* **115**, 1659-90.
12. Schwan HP (1988) Dielectric spectroscopy and electrorotation of biological cells. *Ferroelectrics* **86**, 205-23.
13. Hughes MP, Archer S and Morgan H (1999) Mapping the electrorotational torque in planar microelectrodes. *J Phys D: Appl Phys* **32**, 1548-52.

## APPENDIX

### Torques acting on objects at different sites of the measuring area

The time average torque in circularly polarized fields,

$$\langle \vec{N} \rangle = \frac{1}{2} \text{Re} \{ \vec{m} \times \vec{E}^* \} \quad (\text{A1})$$

is given by the cross-product of the induced dipole moment ( $\vec{m}$ ) and the conjugated field ( $\vec{E}^*$ )<sup>2,3</sup>. The elliptical AC field in the x-y plane can be written in component notation as (see Fig. 1, Eqs. (2) and (3)):

$$\vec{E} = \begin{pmatrix} E_x \\ E_y \\ E_z \end{pmatrix} = \begin{pmatrix} a/r & E_0 \\ j & b/r & E_0 \\ 0 & & \end{pmatrix} = \begin{pmatrix} E_{\max} \\ E_{\min} \\ 0 \end{pmatrix} \quad (\text{A2})$$

Both, the x- and y-field components are sinusoidal with a 90°-phase shift, denoted by  $j = \sqrt{-1}$ . We assume that the magnitude of the field component oriented in  $\hat{i}_1$ -direction is larger than in  $\hat{j}$ -direction with no limitation in generality. For the elliptic field apart from the center,

factors a and b were introduced leading to:

$$E_{\min} = j \frac{b}{a} E_{\max} \quad (\text{A3})$$

and the conjugated fields:

$$E_{\min}^* = -j \frac{b}{a} E_{\max}^* \quad (\text{A4})$$

(see Eqs. (2) and (3)). The induced dipole moment  $\vec{m}$  is proportional to the field. In component notation  $\vec{m}$  is given by<sup>9</sup>:

$$\vec{m} = (m_x \quad m_y \quad m_z) = (\alpha E_{\max} \quad \alpha E_{\min} \quad 0) \quad (\text{A5})$$

Introducing Eqs. (A2) and (A5) the torque of Eq. (A1) becomes:

$$\langle \vec{N} \rangle = \frac{1}{2} \text{Re} \left( \alpha E_{\max} E_{\min}^* - \alpha E_{\min} E_{\max}^* \right) \hat{k} \quad (\text{A6})$$

where  $\hat{k}$  stands for the unit vector pointing in z-direction. Introducing Eq. (A4) we get:

$$\langle \vec{N} \rangle = \frac{1}{2} \text{Re} \left( \alpha \left( E_{\max} \left( -j \frac{b}{a} \right) E_{\max}^* - E_{\min} \left( j \frac{a}{b} \right) E_{\min}^* \right) \right) \hat{k} \quad (\text{A7})$$

Eq. (A7) can re-written as:

$$\langle \vec{N} \rangle = \frac{1}{2} \text{Im} \left( -j \alpha \left( E_{\max}^2 \left( \frac{b}{a} \right) + E_{\min}^2 \left( \frac{a}{b} \right) \right) \right) \hat{k} \quad (\text{A8})$$

Introducing Eqs. (2) and (3) for  $E_{\max}$  and  $E_{\min}$  we obtain:

$$\langle \vec{N} \rangle = \left( \frac{ab}{r^2} \right) E_0^2 \text{Re}(-j\alpha) \hat{k} \quad (\text{A9})$$

which can be simplified to:

$$\langle \vec{N} \rangle = \left( \frac{ab}{r^2} \right) E_0^2 \text{Im}(\alpha) \hat{k} \quad (\text{A10})$$

Accordingly, the torque in an elliptical field is:

$$\langle \vec{N} \rangle = E_{\max} E_{\min} \text{Im}(\alpha) \hat{k} \quad (\text{A11})$$

and reduces to:

$$\langle \vec{N} \rangle = E_0^2 \text{Im}(\alpha) \hat{k} \quad (\text{A12})$$

in a circular field with  $r = a = b$ .



## Appendix C

### Paper 3:

Maswiwat K, Wachner D, Warnke R and Gimsa J  
2007b Simplified equations for the transmembrane  
potential induced in ellipsoidal cells of rotational  
symmetry. *J. Phys. D: Appl. Phys.* **40** 914-23

# Simplified equations for the transmembrane potential induced in ellipsoidal cells of rotational symmetry

K Maswivat, D Wachner, R Warnke and J Gimsa

Institute of Biology, Chair of Biophysics, University of Rostock, D-18051 Rostock, Germany

E-mail: [jan.gimsa@uni-rostock.de](mailto:jan.gimsa@uni-rostock.de)

Received 26 September 2006, in final form 17 November 2006

Published 19 January 2007

Online at [stacks.iop.org/JPhysD/40/914](http://stacks.iop.org/JPhysD/40/914)

## Abstract

The induction of transmembrane potentials ( $\Delta\phi$ ) by an external field is the basis of numerous applications in biotechnology, cell-technology and medicine. We have developed new, simplified analytical equations that avoid the complicated description by the depolarizing factors. The equations apply to the  $\Delta\phi$  induced in cells resembling ellipsoids of rotation, i.e. spheroids by homogeneous dc or ac fields. They will be especially useful for experimental scientists. The equations describe the dependence of the  $\Delta\phi$  on the electric media properties, the field frequency and the axis ratio for oblate and prolate spheroids for which the symmetry semiaxis ( $c$ ) is shorter and longer than the other two semiaxes ( $a$  and  $b$ , with  $a = b$ ), respectively. According to the Schwan equation, an electric field  $E$  may induce a maximum  $\Delta\phi$  of  $1.5aE$  at the poles of a spherical cell. For the poles of spheroidal cells, the maxima can be easily described by  $\Delta\phi = (a + 2c)E/2$  and  $\Delta\phi = a(a + 2c)E/(a + c)$  for fields oriented along and perpendicular to the symmetry axis, respectively. For practically important shapes the error in the magnitude of  $\Delta\phi$  is smaller than 5% except along the  $c$ -axis for axis ratios larger than 2. Nevertheless, the errors vanish for the three limiting shapes of infinitely thin disc, sphere and cylinder.

## 1. Introduction

A huge body of literature exists on applications of the induced transmembrane potential ( $\Delta\phi$ ) in cell technology (Chang *et al* 1992, Neumann *et al* 1989, Tsong 1991, Zimmermann *et al* 2000). It is known that the application of fields inducing a  $\Delta\phi$  of the order of 1 V may lead to a destabilization of the membrane structure and subsequent membrane poration (Chang *et al* 1992, Neumann *et al* 1989, Tsong 1991). Nevertheless, a closer look at the phenomenon reveals that it is not justified to refer to a critical  $\Delta\phi$ . It can be shown that the 'critical voltage'-phenomenon results from the strongly nonlinear processes in pore formation (Glaser *et al* 1988). The effect can be applied for cell hybridization in the production of monoclonal antibodies, cell transfection and other cell technology applications. More recent developments apply electric membrane poration for electro-chemo and electro-gene therapy (Gothelf *et al* 2003, Mir *et al* 1998, Neumann *et al* 1998, Smith *et al* 2004). Lower electric fields applied to

cell suspensions or tissues may induce the  $\Delta\phi$  that can trigger the firing of electrically active cells, such as neurons or heart muscle cells.

In ac fields, the  $\Delta\phi$  of spherical cells depends on field frequency, electric media properties and size (Gimsa and Wachner 1999, DeBruin and Krassowska 1999, Grosse and Schwan 1992). Examples of a spherical shape are vesicles, protoplasts, murine myeloma cells (Gimsa *et al* 1999, Marszalek *et al* 1990), neurospora slime cells (Gimsa *et al* 1991) and some bacteria, e.g. *Streptococcus* (Batzing 2002, Gunsalus and Stanier 1960).

For non-spherical cells shape and orientation also play a role. Many cells deviating from the spherical shape exhibit a rotational symmetry resembling spheroids. Spheroids may have a symmetry axis that is shorter (oblate spheroids) or longer (prolate spheroids) than their equatorial radius. Shapes similar to oblate spheroids can be observed in many mammalian red blood cells (Gimsa and Wachner 1998), whereas retina photoreceptor cells (Blanks 1989,

Radu *et al* 2005), bacteria such as *Bacillus subtilis*, *E. coli*, *Pseudomonas* (Batzing 2002, Gunsalus and Stanier 1960) and yeasts such as *Schizosaccharomyces pombe* (Asencor *et al* 1993) are examples of the prolate shape.

As early as 1953, Fricke presented the (dc) steady state  $\Delta\phi$  induced at the poles of an oriented cell of a general ellipsoidal shape with negligible membrane conductance, in its most general form (Fricke (1953), see also Bernhardt and Pauly (1973)):

$$\Delta\phi_a = \frac{1}{1 - n_a} a E_x, \quad (1)$$

where  $E_x$ ,  $a$  and  $n_a$  stand for the field strength (in the  $a$ -direction), the semiaxis oriented in the field direction and the depolarizing factor along semiaxis  $a$  (appendix A), respectively. Depending on the axis ratio of the ellipsoid  $n_a$  ranges from 0 to 1 (Stratton 1941, Stille 1944, Gimsa and Wachner 1999). For a sphere of radius  $r$  with no preferred orientation  $n_a = n_b = n_c = 1/3$  and equation (1) reduces to the well-known expression:

$$\Delta\phi = 1.5 r E. \quad (2)$$

Several attempts have been made to introduce the specific electric properties of the cell and external media, as well as the surface conductance into the equation for spherical (Grosse and Schwan 1992, DeBruin and Krassowska 1999) and spheroidal cells (Bernhardt and Pauly 1973, Jerry *et al* 1996). We were probably the first to derive analytical expressions for both orientations of the symmetry axis of a spheroidal cell, assuming a nonconductive membrane and a highly polarizable cytoplasm (Gimsa and Wachner 1999, 2001a). Later, the deviation was extended to arbitrarily oriented cells of the general ellipsoidal shape including all electrical parameters (Gimsa and Wachner 2001b). Nevertheless, these derivations are based on the depolarizing factors, which are given by quite complex expressions as shown in appendix A.

In this work, we present simplified analytical equations for the influential radii, i.e. the geometry-factors  $1/(1 - n_a)$  (see equation (1)) that avoid the complicated description by the full expressions for the depolarizing factors  $n_a$  and  $n_c$  (appendix A). The equations apply for the  $\Delta\phi$  induced in oblate and prolate cells (or tissue bodies such as abscesses and bruises) by homogeneous dc or ac fields. In practice, there will always be errors arising from the measurement of the geometric cell parameters, as well as deviations of the cell shapes from an idealized spheroidal shape. In any case, our approximations will be superior than the assumption of a spherical shape with a mean or effective radius and the experimental errors will be larger than the discrepancies introduced by our simplifications.

## 2. Theory

### 2.1. The influential radius

Starting from a special finite element model, we introduced the parameter ‘influential radius’ for ellipsoidal objects (Gimsa and Wachner 1999). The influential radius along each semiaxis refers to a certain distance from the symmetry plane that is oriented perpendicular to the semiaxis and located at the centre of the object. The influential radius along semiaxis  $a$ ,  $a_{\text{infl}}$  defines the distance of that equipotential plane in

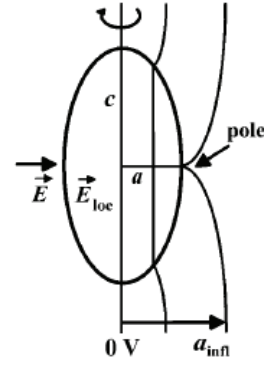


Figure 1. Sketch of the equipotential planes in the surroundings of a cell or a vacuum-body and inside its homogeneous Maxwellian equivalent body. The homogeneous external field  $\vec{E}$  is oriented perpendicular to the symmetry axis  $c$  of the prolate cell model. The maximum potential at pole  $a$  is given by  $\phi_a = a_{\text{infl}} E$ .  $\phi_a$  can be used to calculate the constant local field  $E_{\text{loc}}$  inside the Maxwellian equivalent body of the cell,  $E_{\text{loc}} = \phi_a/a$ .

the external medium that would just touch a body of non-polarizable material (vacuum) of the same shape at the pole of semiaxis  $a$  (figure 1). Thus, it defines the maximum potential at the surface of an ellipsoidal body of a given axis ratio.

The relative influential radius along semiaxis  $a$ ,  $a_{\text{infl}}/a$  is solely dependent on the shape but not on the size of the object. Along an axis the relative influential radius can be determined from the depolarizing factor (appendix A). Along axis  $a$  it is given by

$$\frac{a_{\text{infl}}}{a} = \frac{1}{1 - n_a}. \quad (3)$$

The relative influential radii are identical to the maximum field amplification factors (please compare with the factor of 1.5 for the spherical shape in equation (2)). Since the potential at the centre plane can be assumed to be 0 V, the maximum potential at the pole oriented in the field direction is  $a_{\text{infl}} E$ . For a membrane-covered object with a highly conductive core, this potential will fully drop over the membrane.

### 2.2. The induced transmembrane potential

In the case of an arbitrarily oriented cell of the general ellipsoidal shape the transmembrane potential at the membrane point ( $\Delta\phi_p$ ) is given by

$$\Delta\phi_p = \frac{\Delta\phi_a d_x}{a} + \frac{\Delta\phi_b d_y}{b} + \frac{\Delta\phi_c d_z}{c}, \quad (4)$$

where  $d_x$ ,  $d_y$  and  $d_z$  stand for the distance of the membrane point to the three symmetry planes that are located at the centre of the object and oriented perpendicular to their respective semiaxes (for details see appendix B and Gimsa and Wachner (2001b)). At the pole of semiaxis  $a$  ( $d_x = a$ ,  $d_y = d_z = 0$ ) equation (4) reduces to equation (1). For an external field of arbitrary orientation, the  $\Delta\phi$ -components at the three poles  $a$ ,  $b$  and  $c$  are solely induced by the respective field components ( $E_x$ ,  $E_y$ ,  $E_z$ ) along the semiaxes.

K Maswiwat *et al*

Therefore, an arbitrarily oriented external field is described by components that are parallel to the principal axes of the ellipsoid.

The  $\Delta\phi_a$  at the pole and the characteristic frequency  $f_{c,a}$  along semiaxis  $a$  are given in the general form for an ac field oriented in the direction of semiaxis  $a$  (Gimsa and Wachner 1998, 1999):

$$\Delta\phi_a = \frac{a_{\text{inff}} E}{(1 + ag_m(1/\sigma_i + (a_{\text{inff}} - a)/a\sigma_e))\sqrt{1 + f^2/f_{c,a}^2}}, \quad (5)$$

$$f_{c,a} = \frac{1}{2\pi C_m} \left( \frac{\sigma_e \sigma_i}{a\sigma_e + (a_{\text{inff}} - a)\sigma_i} + g_m \right), \quad (6)$$

where  $E$  is given by  $(E_x, 0, 0)$  and  $f$ ,  $f_{c,a}$ ,  $\sigma_i$  and  $\sigma_e$  stand for the external field frequency, the characteristic frequency of membrane polarization along semiaxis  $a$  and the internal and external conductivities, respectively.  $C_m$ ,  $g_m$  and  $d$  stand for the area specific membrane capacitance in  $\text{F m}^{-2}$ , the area specific membrane conductance in  $\text{S m}^{-2}$  and thickness of membrane, respectively. The area specific membrane capacitance and conductance in the equations can also be expressed as  $C_m = \varepsilon_0 \varepsilon_m / d$  and  $g_m = \sigma_m / d$ .

Capacitive bridging decreases the membrane impedance at higher frequencies. The characteristic frequency of this bridging is identical for the membrane polarization in the poration and in the ac-electrokinetic techniques (Schwan 1983b). For example, it corresponds to the first characteristic frequency, i.e. the 'membrane peak' in electrorotation (Gimsa *et al* 1991).

At  $f_{c,a}$  the  $\Delta\phi$  is decreased by a factor of  $1/\sqrt{2}$  or  $-3$  dB. Analogous expressions for equations (5) and (6) hold along the other two axes. After introduction of equation (6) into equation (5) for the three semiaxes, the latter equations can be introduced into equation (4) to obtain a solution for the general case of a single-shell object of the general ellipsoidal shape. This shape represents the most complex geometry of a closed surface of the second degree for which closed solutions of the Laplace equations can be found (Gimsa and Wachner 2001b).

### 2.3. Simplifications for spheroidal cells

**2.3.1. Shape of the cell model.** In the following we will restrict our considerations to the simplified case of spheroidal cells ( $a = b$ ). Spheroidal models are oblate and prolate when their symmetry axis is shorter ( $c < a = b$ , figure 2(A)) and longer ( $c > a = b$ , figure 2(C)) than the semiaxes  $a$  and  $b$ , respectively. For simplicity, we fixed  $a$  and  $b$  to typical cell values of  $3.5 \mu\text{m}$ , varying  $c$  between  $0.035 \mu\text{m}$  (axis ratio 1:100) and  $350 \mu\text{m}$  (axis ratio 100:1). Figure 2 gives sketches of cells of different shapes with  $m$ ,  $i$  and  $e$  denoting the membrane, cytoplasm and external medium, respectively. Please note that a non-uniform membrane thickness cannot be avoided in the confocal ellipsoidal coordinate system. Gimsa and Wachner (1999) as well as Sekine *et al* (2002) discussed the importance of a correct membrane thickness along the semiaxis in the field direction. In our model, the same membrane thickness is assumed at each pole oriented in the field direction or the directions of the considered field components.

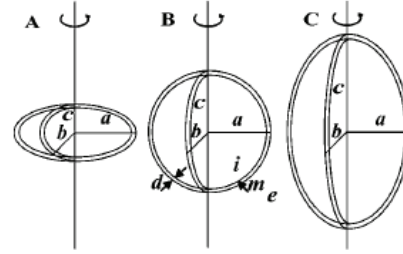


**Figure 2.** The sketch of spheroidal single-shell models of oblate (A), spherical (B), and prolate (C) shape with the same semiaxes  $a = b$ , where  $d$  is the membrane thickness (see text) and  $i$ ,  $m$  and  $e$  denote the cytoplasm, membrane and external medium, respectively. Fields oriented parallel and perpendicular with respect to the symmetry axis will be considered. The general field orientation is a superposition of such field components (see equation (4) and appendix B).

Accordingly, separate consideration of the field components along each semiaxis leads to a very small remaining error. In other words, a spheroidal biological cell is represented by two different spheroidal models with different non-uniform membranes that ensure a correct membrane thickness along either semiaxis  $a$  (and  $b$ ) or  $c$ .

**2.3.2. Approximating the axis ratio dependence of the influential radius.** For spheroids the plot of  $a_{\text{inff}}/a$  (equation (3)) using the depolarizing factor  $n_a$  given in appendix A) over the logarithm of the axis ratio exhibits a sigmoidal shape (figure 3(A)). The limiting values for an infinitely thin disc and an infinitely long cylinder are 1 and 2, respectively. This behaviour can be approximated by (Warnke 2003)

$$\frac{a_{\text{inff}}}{a} = \frac{a + 2c}{a + c} = 2 - \frac{1}{1 + c/a}. \quad (7)$$

The sum of the depolarizing factors ( $n_a + n_b + n_c$ ) along the three principal axes of a general ellipsoid is always unity (Stratton 1941, Stille 1944). It follows that  $a/a_{\text{inff}} + b/b_{\text{inff}} + c/c_{\text{inff}} = 2$  (Gimsa 2001). Therefore, for spheroids along the symmetry axis  $c$ :

$$\frac{c_{\text{inff}}}{c} = \frac{a + 2c}{2c} = 1 + \frac{1}{2c/a}. \quad (8)$$

Equations (7) and (8) can be introduced into equation (4) as well as into equations (5) and (6) as the most general case for spheroidal cells. The new expressions for  $a_{\text{inff}}$  and  $c_{\text{inff}}$  given in equations (7) and (8) avoid the complicated depolarizing factors for spheroidal cells.

**2.3.3. Simplification for zero membrane conductance.** In a first consideration we will restrict ourselves to spheroidal cells with zero membrane conductance. Along semiaxis  $a$  equation (5) yields

$$\Delta\phi_a = \frac{a_{\text{inff}} E}{\sqrt{1 + f^2/f_{c,a}^2}}. \quad (9)$$

Analogous expressions hold along semiaxes  $b$  and  $c$ . Introducing equations (7) and (8) for  $a_{\text{inff}}$  and  $c_{\text{inff}}$  into

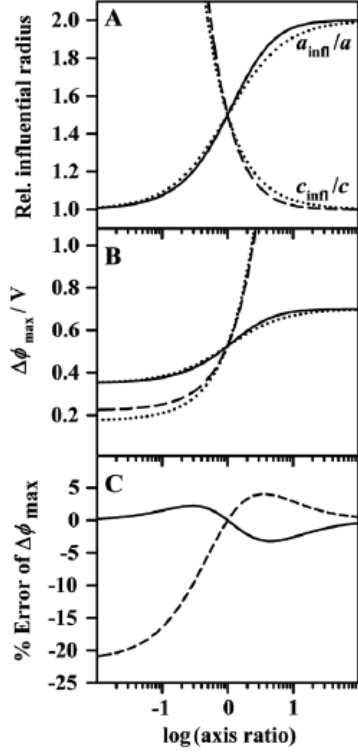


**Figure 3.** Relative influential radius and the maximum  $\Delta\phi$  as functions of the axis ratio. (A) Relative influential radius of spheroids. (B) The maximum  $\Delta\phi$  for a spheroidal cell. (C) Theoretical error of the maximum  $\Delta\phi$  derived from the difference in the full model (equation (1) combined with equations (A.1), and (A.2)) and the simplified model (equation (1) combined with equations (7) and (8)). Solid and dashed lines refer to the  $a$ - and  $c$ -semiaxis, respectively. The dotted lines show results of our simplified equations. Two cell orientations are considered. Negative logarithmic values of the axis ratio denote an oblate, while positive values a prolate shape. Please note that semiaxis  $c$  is of the order of the membrane thickness for the axis ratio of  $10^{-2}$ .  $c_{\text{inf}}/c$  and  $\Delta\phi$  at the pole  $c$  approach infinity for low axis ratios or an infinitely long  $c$ -axis, respectively. For consequences please see section 3.3.

equation (9) yields the following expressions for  $\Delta\phi$  along the semiaxes  $a$  and  $c$ :

$$\Delta\phi_a = \frac{(a+2c)aE}{(a+c)\sqrt{1+f^2/f_{c,a}^2}}, \quad (10)$$

$$\Delta\phi_c = \frac{(a+2c)E}{2\sqrt{1+f^2/f_{c,c}^2}}. \quad (11)$$

Dropping the  $g_m$ -term also from equation (6) yields simplified expressions for the characteristic frequencies along the semiaxes  $a$  and  $c$ . For  $f_{c,a}$  and  $f_{c,c}$  we obtain

$$f_{c,a} = \frac{1}{2\pi a C_m (1/\sigma_1 + c/(a+c)\sigma_e)} \quad (12)$$

and

$$f_{c,c} = \frac{1}{2\pi c C_m (1/\sigma_1 + a/2c\sigma_e)}. \quad (13)$$

For a spherical cell of radius  $r$  with  $a = b = c = r$  equations (12) and (13) become equal to the well-known expression for the characteristic frequency of spherical cells (Marszalek *et al* 1990, Schwan 1983a, 1983b, Zimmermann and Neil 1996). Interesting simplifications of  $\Delta\phi$  are also possible for the limiting shapes, thin disc ( $c \ll a$ ) and long cylinder ( $c \gg a$ ). In these cases one of the axes can be neglected. For the disc shape,  $\Delta\phi$  in equations (10) and (11) can be simplified to

$$\Delta\phi_a = \frac{aE}{\sqrt{1+(2\pi f C_m a/\sigma_1)^2}}, \quad (14)$$

$$\Delta\phi_c = \frac{aE}{2\sqrt{1+(\pi f C_m a/\sigma_e)^2}}. \quad (15)$$

Equation (15) exhibits a relatively large error (figure 3). An additional effect will arise for small axes ratios. The thickness of the considered object will in this case be of the order of the membrane thickness. For very thin disc shapes, the whole oblate object will become capacitively bridged and the simplified description may become better than the full model as could be shown from numerical considerations. A detailed analysis of this effect is still open. Nevertheless, it may be important for thin cellular protrusions such as axons, nanotubes, the nuclear membrane and the Golgi-apparatus.

For the cylindrical shape,  $\Delta\phi$  yields

$$\Delta\phi_a = \frac{2aE}{\sqrt{1+(2\pi f C_m a(1/\sigma_1 + 1/\sigma_e))^2}} \quad (16)$$

$$\Delta\phi_c = \frac{cE}{\sqrt{1+(2\pi f C_m c/\sigma_1)^2}}. \quad (17)$$

**2.3.4. Simplification for the maximum  $\Delta\phi$  at dc or low frequencies.**  $\Delta\phi$  is at maximum in the dc fields and at frequencies below the capacitive membrane bridging. The effective polarizability of the cell is comparable to that of a ‘vacuum body’ (figure 1). The reason is the insulating membrane of cells. The membrane conductivity was assumed to be much lower than the internal and external conductivities ( $\sigma_m \ll \sigma_1, \sigma_e$ ) in the model. For a field oriented in the  $a$ -direction, the maximum potential at the pole is (see figure 1)

$$\phi_a = a_{\text{inf}} E. \quad (18)$$

An analogous expression holds along semiaxis  $c$ . For fields oriented perpendicular to and parallel to the symmetry axis  $c$ , these conditions allow for finding the maximum  $\Delta\phi$  at the poles of the cell.

Using equations (7) and (8),  $a_{\text{inf}}$  and  $c_{\text{inf}}$  can be rewritten as equations for the  $\Delta\phi$ -maxima:

$$\Delta\phi_a = \left(\frac{a+2c}{a+c}\right) aE, \quad (19)$$

$$\Delta\phi_c = \left(\frac{a+2c}{2}\right) E. \quad (20)$$

Equations (19) and (20) hold for the oblate, spherical and prolate shapes.

K Maswiat *et al***Table 1.** Parameters for model calculations (Gimsa and Wachner 1999).

Parameters	Value
Symmetry axis ( $c$ )	0.035–350 $\mu\text{m}$
Equatorial radius ( $a$ )	3.5 $\mu\text{m}$
Membrane thickness ( $d$ )	8 nm
Conductivity	
Internal ( $\sigma_i$ )	0.53 $\text{S m}^{-1}$
External ( $\sigma_e$ )	0.12 $\text{S m}^{-1}$
Membrane ( $\sigma_m$ )	$10^{-6}$ $\text{S m}^{-1}$
Area specific membrane conductance ( $g_m$ )	125 $\text{S m}^{-2}$
Relative permittivity of membrane ( $\epsilon_m$ )	9.04
Area specific membrane capacitance ( $C_m$ )	0.01 $\text{F m}^{-2}$
External field strength ( $E$ )	100 $\text{kV m}^{-1}$

### 3. Results and discussion

#### 3.1. Cell parameters

In the following considerations we will assume electric cell parameters comparable to those of human red blood cells (table 1).

#### 3.2. The dependence of the maximum $\Delta\phi$ on the cell orientation and shape

To compare the full model (equation (18)), using the depolarizing factors from appendix A to equations (19) and (20) we plotted the relative influential radii ( $a_{\text{infl}}/a$  and  $c_{\text{infl}}/c$ ) (figure 3(A)) and the  $\Delta\phi$ -maxima at the poles of spheroidal cells (figure 3(B)) as functions of the axis ratio. The cell parameters used in figure 3(B) are given in table 1. Two cases were considered, field orientation perpendicular to and along the symmetry axes. Generally,  $\Delta\phi$  at a pole oriented in the field direction increases with an increase in the length of the oriented semiaxis. Obviously, the increase in the length overcompensates the decrease in the relative influential radius. The error in  $\Delta\phi_a$  for a field oriented perpendicular to the symmetry axis is always smaller than 5% (figure 3(C)). This also applies to  $\Delta\phi_c$  of the prolate shape and the parallel orientation. A larger error may occur for the oblate case. Nevertheless, for axis ratios below 2, the error is always below 5%. The error arising from the simplified description of the depolarizing factor vanishes again for discs that are unrealistically flat for biological objects.

#### 3.3. Limiting shapes

With our new equations it is simple to consider otherwise complex relations that may be interesting for extreme shapes such as thin-oblate or needle-shaped objects that may appear in colloidal suspensions. For a thin disc ( $c \ll a$ ),  $a_{\text{infl}}/a$  approaches unity and  $c_{\text{infl}}/c$  infinity (figure 3(A)). In this case,  $\Delta\phi$  in equations (19) and (20) can be simplified to (see also figure 3(B))

$$\Delta\phi_a = aE, \quad (21)$$

$$\Delta\phi_c = aE/2. \quad (22)$$

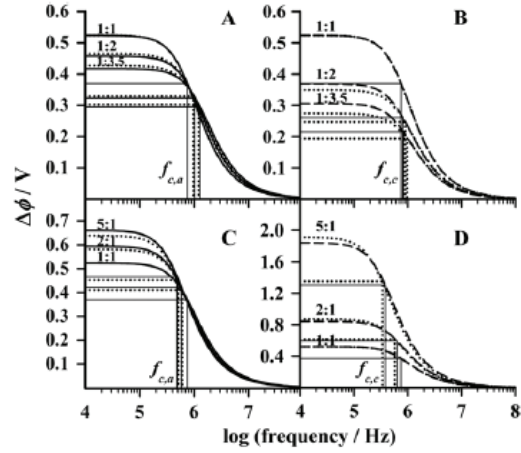


**Figure 4.**  $\Delta\phi$  and the corresponding  $f_c$  as a function of the field frequency. (A) and (B) oblate shapes; (C) and (D) prolate shapes. Field orientation is in the  $a$ - (A) and (C) or the  $c$ -direction (B) and (D). The full model (equation (5) for  $g_m = 0 \text{ S m}^{-2}$  or equation (9) using the depolarizing factors of equations (A.1) and (A.2)) is compared with the simplified equations (10) and (11) (dotted lines). Solid and dashed lines refer to the  $a$ - and  $c$ -semiaxis, respectively.

Equation (22) cannot be easily derived from the full model (equation (1)) with depolarizing factors because in this model semiaxis  $c$  approaches zero whereas  $c_{\text{infl}}/c$  approaches infinity (equation (1)). For an extreme prolate shape ( $c \gg a$ ) the geometry approaches a cylinder;  $a_{\text{infl}}/a$  and  $c_{\text{infl}}/c$  become 2 and 1, respectively (figure 3(A); see also Gimsa and Wachner (1999)).  $\Delta\phi_c$  approaches infinity for an infinitely long semiaxis  $c$  (figure 3(B)). In this case, equations (19) and (20) yield (compare with equations (16) and (17) for  $f = 0 \text{ Hz}$ ; see also figure 3(B))

$$\Delta\phi_a = 2aE, \quad (23)$$

$$\Delta\phi_c = cE. \quad (24)$$

#### 3.4. Frequency dependence of the $\Delta\phi$

Figure 4 shows the frequency dependence of the  $\Delta\phi$ -amplitudes at the poles ( $\Delta\phi_a$  and  $\Delta\phi_c$ ) for two orientations of the spheroid. In the figure equations (10) and (11) are compared with the full model (equation (5) for  $g_m = 0 \text{ S m}^{-2}$ , i.e. equation (9)) using the model parameters from table 1. Starting from a spherical cell (1:1) axes ratios of 1:2 and 1:3.5 for the oblate as well as 2:1 and 5:1 for the prolate shapes are considered. For these axis ratios biological examples can be found: human red blood cells exhibit an oblate shape (axis ratio about 1:3.5; for experimental results see Gimsa and Wachner (1998)). Axes ratios of 2:1 and 5:1 can be found in plated Chinese hamster ovary cells and bacilli, respectively (for experimental results see Valic *et al* (2003)).

For the oblate shape, the low frequency plateaus of  $\Delta\phi_a$  were higher than those for  $\Delta\phi_c$ . For both orientations  $\Delta\phi$  is decreased with respect to the spherical shape (figures 4(A) and (B)). For the prolate shape, the plateau values of  $\Delta\phi_a$  are larger than for the spherical shape but still lower than for  $\Delta\phi_c$  (figures 4(C) and (D)); also please compare with the  $\Delta\phi$ -values

in figure 3(B) for the dc fields).  $\Delta\phi$  approaches zero at high frequencies in the MHz–GHz range. The reason is the constant conductivity contributions of the external and internal bulk media and an impedance of the membrane capacitance that steadily decreases with frequency, i.e. capacitive membrane bridging. In a model where the permittivities of the bulk were not neglected  $\Delta\phi$  would reach a high frequency plateau (Gimsa and Wachner 2001b). The characteristic frequencies  $f_{c,a}$  and  $f_{c,c}$  are presented by a perpendicular drop-line from that point of the  $\Delta\phi$ -curve where the initial  $\Delta\phi$ -magnitude are decreased by  $-3$  dB.

For spherical cells the new equations are exact (no dotted lines). For deviating shapes the errors of  $\Delta\phi_a$  and  $\Delta\phi_c$  are smaller than 5% and 10%, respectively. In any case the error of  $\Delta\phi_a$  is smaller than for  $\Delta\phi_c$ .

### 3.5. Dependence of $f_c$ on cell properties

Figure 5 presents the  $f_c$  dependence on the axes ratio along the semiaxes  $a$  and  $c$  for various electric cell parameters. In the figure results from the full model (equation (6) with depolarizing factors) are compared with the model with a simplified description of the influential radii (equations (7) and (8)). For the iteration of one parameter ( $\sigma_i$ ,  $\sigma_e$ ,  $g_m$  and  $C_m$ ) the other parameters were kept at their standard values (table 1). The semiaxes  $a$  and  $b$  were kept constant at  $a = b = 3.5 \mu\text{m}$ . Generally,  $f_c$  is increased for increased conductivities ( $\sigma_i$ ,  $\sigma_e$ ,  $g_m$ ) and a decreased capacitance ( $C_m$ ) (Gimsa *et al* 1991). As can be seen from the figures, this may result in largely parallel  $f_c$ -functions. In some cases the functions converge or diverge for extreme axis ratios. In these cases, the influence of the considered parameter  $\sigma_i$ ,  $\sigma_e$  or  $g_m$  vanishes or increases. This effect can be explained by the model geometry: for extremely oblate and prolate shapes the internal and external conductivity contributions in the model (conductance) increase such that contributions of the conductivity (conductance) at the other side of the membrane take over completely. The internal conductance is determined by  $\sigma_i$  and the semiaxis length. Analogously the external conductance is determined by  $\sigma_e$  and the difference in the influential radius and semiaxis (for details of the geometry please see Gimsa and Wachner (1999, 2001b)).

Examples for convergence are the dependence of the characteristic frequency on  $\sigma_i$  for thin oblates in the  $c$ -direction (figure 5(A)), the dependence on  $\sigma_e$  for thin oblates in the  $a$ -direction (figure 5(B)) and the dependence on  $\sigma_e$  for long prolates in the  $c$ -direction (figure 5(B)). In the case of divergence the parameter influence increases for extreme axis ratios, such as that of  $g_m$  for long prolates in the  $c$ -direction (figure 5(C)). Consequently, the influence of an increased  $g_m$  on  $f_c$  will be clearest for prolate cells when the field is parallel to semiaxis  $c$ . Nevertheless, in the  $a$ -direction the curves converge for thin oblates (figure 5(C)). At the opposite axis ratio the curves become parallel. Parallel curves may possess a slope (e.g.  $C_m$  in the  $c$ -direction for long prolates) or even reach constant levels (e.g.  $C_m$  in the  $a$ -direction for long prolates).

Interesting cases for  $f_c$  are the limiting shapes of disc and cylinder, respectively. For the disc shape, equation (6) can be

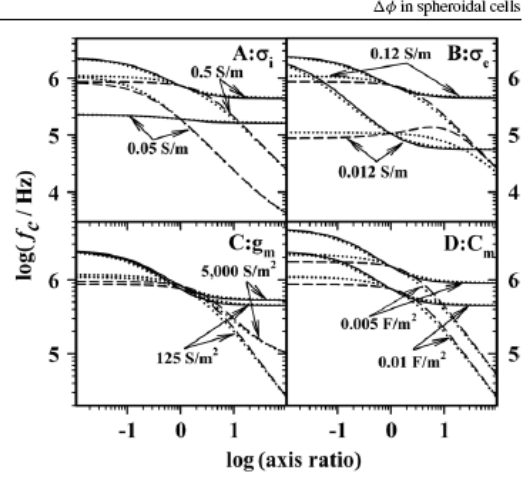


**Figure 5.**  $f_c$  given by the full model and the simplified equations (dotted lines) as functions of the axis ratio for different cell properties (for standard parameters please see table 1). (A) Internal conductivity variation:  $\sigma_{i1} = 0.5 \text{ S m}^{-1}$  and  $\sigma_{i2} = 0.05 \text{ S m}^{-1}$ . (B) External conductivity variation:  $\sigma_{e1} = 0.12 \text{ S m}^{-1}$  and  $\sigma_{e2} = 0.012 \text{ S m}^{-1}$ . (C) Membrane conductance variation:  $g_{m1} = 5000 \text{ S m}^{-2}$  and  $g_{m2} = 125 \text{ S m}^{-2}$ . (D) Area specific membrane capacitance variation:  $C_{m1} = 0.01 \text{ F m}^{-2}$  and  $C_{m2} = 0.005 \text{ F m}^{-2}$ . Solid and dashed lines refer to the  $a$ - and  $c$ -semiaxis, respectively.

simplified to

$$f_{c,a} = \frac{1}{2\pi C_m} \left( \frac{\sigma_i}{a} + g_m \right), \quad (25)$$

$$f_{c,c} = \frac{1}{2\pi C_m} \left( \frac{2\sigma_e}{a} + g_m \right). \quad (26)$$

Thus,  $f_{c,a}$  depends on  $\sigma_i$  and semiaxis  $a$  (equation (25), figures 5(A) and (B)), whereas the influence of  $\sigma_e$  is vanishing. In contrast,  $f_{c,c}$  depends on  $\sigma_e$  and semiaxis  $a$  (equation (26), figure 5(B)). For the cylinder shape equation (6) can be simplified to

$$f_{c,a} = \frac{1}{2\pi C_m} \left( \frac{1}{a/\sigma_i + a/\sigma_e} + g_m \right), \quad (27)$$

$$f_{c,c} = \frac{1}{2\pi C_m} \left( \frac{\sigma_i}{c} + g_m \right). \quad (28)$$

Now  $f_{c,a}$  depends on  $\sigma_e$  and  $\sigma_i$  and semiaxis  $a$  (equation (27), figures 5(A) and (B)). Both conductivities  $\sigma_e$  and  $\sigma_i$  influence  $f_{c,a}$  in the same way, as can be expected for a relative influential radius of 2. In this case both the internal and external media elements span the same distance. In contrast,  $f_{c,c}$  depends only on  $\sigma_i$  and semiaxis  $c$  (equation (28), figure 5(A)).

$f_c$  errors can be calculated from equation (6) using the actual influential radii and our simplified equations (7) and (8). Accordingly there is no error for spherical cells. The errors of  $f_{c,a}$  are generally smaller than for  $f_{c,c}$ . For axis ratios below 2, the errors for  $f_{c,a}$  and  $f_{c,c}$  are always below 10% and 15%, respectively. Moreover, the errors also depend on the electric cell parameters. Whereas their dependence on  $\sigma_i$  and  $\sigma_e$  is noticeable, they are largely independent of  $g_m$  and  $C_m$  for our cell geometry.

K Maswiwat *et al*

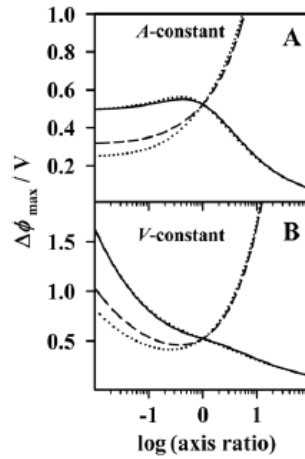


**Figure 6.** The maximum  $\Delta\phi$  as a function of the axis ratio for a cell model with constant membrane surface (A) and constant cell volume (B). Solid and dashed lines refer to the  $a$ - and  $c$ -semiaxis, respectively. The dotted lines show results of our simplified equations.

3.6. Axis ratio dependence of  $\Delta\phi$  and  $f_c$  for cells of constant surface or volume

In biotechnology or basic research applications, electrically polarized cells may undergo deformations induced by mechanical and osmotic load, drug-induced shape changes or cell differentiation. Idealized assumptions are a constant membrane surface area ( $A$ ; Parker and Winlove 1999) and cell volume ( $V$ ; Bryant and Wolfe 1987, Hoffman 1987, Takashima *et al* 1985), respectively. Accordingly, the following conditions must hold during the deformation:

1. for the membrane surface area,  $A$  (Tee 2004):

$$A = \begin{cases} = 2\pi a \left( a + \frac{c^2}{\sqrt{a^2 - c^2}} \operatorname{arcsinh} \frac{\sqrt{a^2 - c^2}}{c} \right) & \text{for } c < a \\ = 4\pi a^2 & \text{for } c = a \\ = 2\pi a \left( a + \frac{c^2}{\sqrt{c^2 - a^2}} \operatorname{arcsin} \frac{\sqrt{c^2 - a^2}}{c} \right) & \text{for } c > a \end{cases} = \text{const}, \quad (29)$$

2. for the cell volume,  $V$ :

$$V = \frac{4}{3}\pi a^2 c = \text{const}. \quad (30)$$

We assumed the electric cell parameters of human red blood cells (table 1) to consider the shape dependence of the maximum  $\Delta\phi$  (equation (5)) and  $f_c$  (equation (6)) for a constant surface area or cell volume. Figures 6(A) and (B) show the shape dependence of the maximum  $\Delta\phi$  for these two conditions. Starting from the same spherical geometry, the dc-maxima of  $\Delta\phi_a$  and  $\Delta\phi_c$  of oblate and prolate cells with a constant surface area are always smaller than for cells with a constant volume. This relation is correctly reflected by our

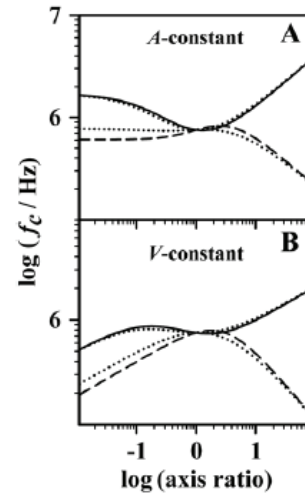


**Figure 7.**  $f_c$  for constant membrane surface (A) and constant cell volume (B) as a function of the axis ratio. Solid and dashed lines refer to the  $a$ - and  $c$ -semiaxis, respectively. The dotted lines show the results of our simplified equations. Please note that a logarithmic scaling is generally used in frequency plots (compare with figures 4 and 5).

equations. The assumption of a membrane conductance of  $g_m = 0.5 \text{ S m}^{-2}$  has a negligible influence on the magnitudes of  $\Delta\phi_a$  and  $\Delta\phi_c$ . The error-curves (dotted lines) of the equations in figure 6 are not given. They are identical to figure 3(C) since the relative error of equations (19) and (20) does not depend on the object size.

Figures 7(A) and (B) show the results for the characteristic frequencies. In both cases, a constant surface area or cell volume, the errors (dotted lines) of  $f_{c,a}$  are generally smaller than for  $f_{c,c}$ . For axis ratios below 2, the errors of  $f_{c,a}$  and  $f_{c,c}$  are always smaller than 5% and 10%, respectively. Errors larger than 10% are only found for axis ratios above 5:1. Please note that frequency dependences in biological systems are usually of the Lorentz-type. When plotted on a log-scale, even a 20% error presents a relatively small deviation in the characteristic frequency (compare with figure 4).

4. Conclusions

We derived simplified equations for the  $\Delta\phi$  induced at the poles of spheroidal cells as well as for the characteristic frequency of membrane polarization,  $f_c$ . For comparison, two orientations of the symmetry axis were considered, these being along and perpendicular to the field. Our equations can be considered generalized Schwann equations, describing the  $\Delta\phi$  dependence on the size and axis ratio for spheroidal cells. We found that for oriented cells the  $\Delta\phi$  increase caused by an increase in the length of the axis pointing in the field direction always overcompensates the reduction in the associated relative influential radius. For cells deforming at a constant volume, the  $\Delta\phi$  is always larger (or equal—in the case of spherical cells) than for cells with a constant surface area. The error of the simplified equations (compared with the full



equations) is a function of the cell shape, size and orientation. The error also depends on the electric cell properties such as  $\sigma_i$ ,  $\sigma_o$ , but not on  $g_m$  and  $C_m$ . For an axis ratio below 2, errors in the magnitude of  $\Delta\phi$  and  $f_c$  are generally smaller than 10% and 15%, respectively. The precision of the equations can be drastically improved by a correcting exponent for the axis ratio (appendix D). Even though our equations are very simple they provide better results than other methods of approximation, e.g. by averaging axes lengths ( $(a+c)/2 = r$ ) for applying the standard Schwan equation ( $\Delta\phi = 1.5rE$ ). The new equations can be combined with the angle dependence given in equation (4) to describe  $\Delta\phi$  at arbitrary membrane points for oriented cells (appendix B; see also Gimsa and Wachner (2001)). Of course, our approach can also be used to derive simplified equations for the ac-electrokinetic behaviour of cells (Gimsa and Wachner 1999, Gimsa 2001, Radu *et al* 2005, Zimmermann *et al* 2000).

### Acknowledgments

KM is grateful for a stipend of the Royal Thai government. This study has partly been supported by grant StSch 20020418A of the Bundesamt für Strahlenschutz to JG. The authors are grateful to the International Postgraduate Programmes (IPP) supported by DAAD, BMBF and DFG. R Sleight is kindly acknowledged for his assistance.

### Appendix A

#### A.1. The depolarizing factors of spheroids

Spheroids are ellipsoids with two equal semiaxes ( $a = b$ ) and symmetry axis  $c$ . Their depolarizing factors  $n$  can be presented in an analytical form. For the oblate case ( $a > c$ )  $n$  along semiaxis  $a$  is given by

$$n_a = \frac{1}{2} \left[ 1 - \frac{1+e^2}{e^3} (e - \arctan e) \right] \quad (A.1)$$

with  $e = \sqrt{\left(\frac{a}{c}\right)^2 - 1}$ ,

and for the prolate case ( $a < c$ ):

$$n_a = \frac{1}{2} \left[ 1 - \frac{1-e^2}{2e^3} \left( \ln \frac{1+e}{1-e} - 2e \right) \right] \quad (A.2)$$

with  $e = \sqrt{1 - \left(\frac{a}{c}\right)^2}$ .

For spheres  $n_a = 1/3$ . Equations (A.1) and (A.2) contain the eccentricity  $e$  (Gimsa and Wachner 1999, Gimsa 2001, Stratton 1941, Stille 1944).

### Appendix B

#### B.1. The general orientation of spheroidal cells

In the case of the general orientation, the constant local ( $\vec{E}_{loc}$ ) and cytoplasmic fields ( $\vec{E}_i$ ) are not usually aligned to a semiaxis or to each other. Accordingly, their 0 V symmetry planes are tilted in a different way around the centre point of the spheroid. The principal semiaxes  $a$ ,  $b$  and  $c$  are used to determine an orthonormal coordinate system,  $x$ ,  $y$  and  $z$  (figure B1).

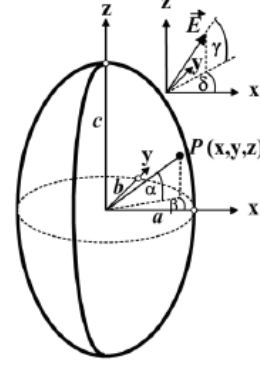


**Figure B1.** The sketch of a prolate spheroidal cell. The principal semiaxes  $a = b$  and  $c$  define the orthonormal coordinate system,  $x$ ,  $y$ ,  $z$ .  $P(x, y, z)$  is a membrane surface point of the cell, defined by angles  $\alpha$  and  $\beta$ . The external electric field  $\vec{E}$  has an arbitrary orientation, determined by the angles  $\gamma$  and  $\delta$ .

The homogeneous external field  $\vec{E}$  is oriented arbitrarily within this coordinate system with the orientation being determined by the angles  $\gamma$  and  $\delta$

$$\vec{E} = \begin{pmatrix} E_x \\ E_y \\ E_z \end{pmatrix} = \begin{pmatrix} \cos \gamma \cos \delta \\ \cos \gamma \sin \delta \\ \sin \gamma \end{pmatrix} |\vec{E}|. \quad (B.1)$$

The local vector  $\vec{P}$  of the membrane point under consideration is determined by the angles  $\alpha$  and  $\beta$

$$\vec{P} = \begin{pmatrix} P_x \\ P_y \\ P_z \end{pmatrix} = \begin{pmatrix} \cos \alpha \cos \beta \\ \cos \alpha \sin \beta \\ \sin \alpha \end{pmatrix} |\vec{P}|. \quad (B.2)$$

For a given membrane point  $P_x$ ,  $P_y$  and  $P_z$  of the spheroid, the following equation holds:

$$\frac{P_x^2}{a^2} + \frac{P_y^2}{a^2} + \frac{P_z^2}{c^2} = 1. \quad (B.3)$$

The combination of equations (B.2) and (B.3) leads to a general expression for the local vector of the membrane point:

$$\vec{P} = \begin{pmatrix} \cos \alpha \cos \beta \\ \cos \alpha \sin \beta \\ \sin \alpha \end{pmatrix} \frac{ac}{\sqrt{c^2 \cos^2 \alpha + a^2 \sin^2 \alpha}}. \quad (B.4)$$

The transmembrane potential induced at any membrane point ( $\Delta\phi_p$ ) can be calculated by (Gimsa and Wachner 2001b)

$$\Delta\phi_p = (\vec{E}_{loc} - \vec{E}_i) \cdot \vec{P}, \quad (B.5)$$

where  $E_{loc}$  stands for the field inside the Maxwellian equivalent body (figure 1) whereas  $E_i$  is the internal, cytoplasmic field. For example, at the pole of semiaxis  $a$  equation (B.5) can be simplified to  $\Delta\phi_a = a(E_{loc} - E_i) = a_{int}E - aE_i$  for

K Maswiat *et al*

a non-polarizable body. The final expression of  $\Delta\phi_p$  is given by

$$\Delta\phi_p = \begin{pmatrix} \frac{a_{\text{infl}} E_x/a}{(1 + ag_m(1/\sigma_1 + (a_{\text{infl}} - a)/a\sigma_e))\sqrt{1 + f^2/f_{c,a}^2}} \\ \frac{a_{\text{infl}} E_y/a}{(1 + ag_m(1/\sigma_1 + (a_{\text{infl}} - a)/a\sigma_e))\sqrt{1 + f^2/f_{c,a}^2}} \\ \frac{a_{\text{infl}} E_z/c}{(1 + cg_m(1/\sigma_1 + (c_{\text{infl}} - c)/c\sigma_e))\sqrt{1 + f^2/f_{c,a}^2}} \end{pmatrix} \vec{P}, \quad (\text{B.6})$$

where the characteristic frequencies of membrane polarization  $f_{c,a}$ , and  $f_{c,c}$  are given by equation (6). The distances  $d$  of a given surface point to the three symmetry planes are given by

$$\begin{aligned} d_x &= |\vec{P}_x|, \\ d_y &= |\vec{P}_y|, \\ d_z &= |\vec{P}_z|. \end{aligned} \quad (\text{B.7})$$

Introducing equation (B.7) into equation (B.6) leads to a simple description of the maximum of the induced  $\Delta\phi_p$  (please compare with equation (4)):

$$\Delta\phi_p = \frac{a_{\text{infl}} E_x d_x}{a} + \frac{a_{\text{infl}} E_y d_y}{a} + \frac{c_{\text{infl}} E_z d_z}{c}. \quad (\text{B.8})$$

## Appendix C

### C.1. Special simplifications

$\Delta\phi$  of spheroidal cells at low frequencies for  $\sigma_1 \gg \sigma_e$ . In the case of low frequencies or dc fields, the frequency-term in equation (5) will be omitted. Equation (5) can be further simplified assuming  $\sigma_1 \gg \sigma_e$ . Introducing equations (7) and (8) for  $a_{\text{infl}}$  and  $c_{\text{infl}}$ , respectively, into equation (5),  $\Delta\phi$  can be rewritten along semiaxes  $a$  and  $c$ :

$$\Delta\phi_a = \frac{(a + 2c)a\sigma_e E}{(a + c)\sigma_e + acg_m}, \quad (\text{C.1})$$

$$\Delta\phi_c = \frac{(a + 2c)\sigma_e E}{2\sigma_e + ag_m}. \quad (\text{C.2})$$

Equations (C.1) and (C.2) do not apply for the limiting shapes, thin disc and long cylinder. For a single-shell sphere of radius  $r$  both equations converge to

$$\Delta\phi = \frac{1.5rE}{1 + 0.5rg_m\sigma_e^{-1}}. \quad (\text{C.3})$$

The characteristic membrane frequencies for zero membrane conductance and  $\sigma_1 \gg \sigma_e$ . Equations (12) and (13) can be

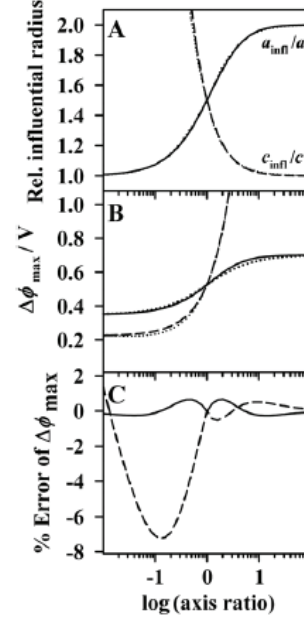


**Figure D1.** Comparison of the full model and the simplified model with improved precision. (A) Relative influential radius calculated according to equation (3) (appendix A) and equations (D.1) and (D.2). (B) Maximum of  $\Delta\phi$ . (C) Theoretical error of equations (D.1) and (D.2) (compare with figure 3). Solid and dashed lines refer to the  $a$ - and  $c$ -semiaxis, respectively. The dotted lines show results of equations (D.1) and (D.2).

further simplified assuming zero membrane conductance and  $\sigma_1 \gg \sigma_e$ :

$$f_{c,a} = \frac{\sigma_e}{2\pi C_m} \left( \frac{1}{a} + \frac{1}{c} \right), \quad (\text{C.4})$$

$$f_{c,c} = \frac{\sigma_e}{\pi a C_m}. \quad (\text{C.5})$$

Please note that these simplifications are not generally possible. Equations (C.4) and (C.5) do not apply for either of the limiting shapes, 'thin oblate' (disc) and 'long prolate' (cylinder). Both equations converge to  $f_c = \sigma_e/(\pi r C_m)$ , for a single shell sphere of radius  $r$ .

## Appendix D

### D.1. Improving the precision of the simplified equations

Despite the satisfactory precision of our simplified equations for experimental purposes it may be desirable to improve the precision without taking into account the full expressions of the depolarizing factors. As can be seen from figure 3(A) a slight compression of the abscissa will improve the approximation of the full equation by our simplified equation. A compression can be achieved by an exponent for the abscissa variable ( $cla$ )

slightly larger than 1. Equations (7) and (8) will get the form

$$\frac{a_{\text{infl}}}{a} = 2 - \frac{1}{1 + (c/a)^\alpha}, \quad (\text{D.1})$$

$$\frac{c_{\text{infl}}}{c} = 1 + \frac{1}{2(c/a)^\alpha}. \quad (\text{D.2})$$

The exponent  $\alpha$  was obtained by fitting equations (D.1) and (D.2) to the equation (3) including equations (A.1) and (A.2). By separate fitting of the oblate and prolate shapes and in the  $a$  and  $c$ -directions, four  $\alpha$ -values were obtained: 1.1 (oblate,  $a$ -direction), 1.33 (prolate,  $a$ -direction), 1.06 (oblate,  $c$ -direction) and 1.29 (oblate,  $c$ -direction). The fitted curves are also given in figure D1. Naturally, the precision can further be improved by fitting  $\alpha$  to a smaller range of the axis ratio according to the experimental requirements.

## References

- Asencor F J, Santamaria C, Iglesias F J and Dominguez A 1993 Dielectric energy of orientation in dead and living cells of *Schizosaccharomyces pombe*: fitting of experimental results to a theoretical model *Biophys. J.* **64** 1626–31
- Batzing B L 2002 *Microbiology: An Introduction* (Pacific Grove, CA: Thomson Learning)
- Bernhardt J and Pauly H 1973 On the generation of potential differences across the membranes of ellipsoidal cells in an alternating electrical field *Biophysik* **10** 89–98
- Blanks J C 1989 Morphology of the retina *Retina* vol 1, ed T E Ogden and A P Schachat (St. Louis, MO: Mosby) pp 37–52
- Bryant G and Wolfe J 1987 Electromechanical stresses produced in the plasma membranes of suspended cells by applied electric fields *J. Membr. Biol.* **96** 129–39
- Chang D C, Chassy B M, Saunders J A and Sowers A E 1992 *Guide to Electroporation and Electrofusion* (San Diego: Academic)
- DeBruin K A and Krassowska W 1999 Modeling electroporation in a single cell II. effects of ionic concentrations *Biophys. J.* **77** 1225–33
- Fricke H 1953 The electric permittivity of a dilute suspension of membrane-covered ellipsoids *J. Appl. Phys.* **24** 644–6
- Gimsa J 2001 A comprehensive approach to electro-orientation, electrodeformation, dielectrophoresis, and electrorotation of ellipsoidal particles and biological cells *Bioelectrochem.* **54** 23–31
- Gimsa J and Wachner D 1998 A unified resistor–capacitor model for impedance, dielectrophoresis, electrorotation, and induced transmembrane potential *Biophys. J.* **75** 1107–16
- Gimsa J and Wachner D 1999 A polarization model overcoming the geometric restrictions of the Laplace solution for spheroidal cells: obtaining new equations for field-induced forces and transmembrane potential *Biophys. J.* **77** 1316–26
- Gimsa J and Wachner D 2001a On the analytical description of transmembrane voltage induced on spheroidal cells with zero membrane conductance *Eur. Biophys. J.* **30** 463–6
- Gimsa J and Wachner D 2001b Analytical description of the transmembrane voltage induced on arbitrarily oriented ellipsoidal and cylindrical cells *Biophys. J.* **81** 1888–96
- Gimsa J, Marszalek P, Loewe U and Tsong T Y 1991 Dielectrophoresis and electrorotation of neurospora slime and murine myeloma cells *Biophys. J.* **60** 749–60
- Glaser R W, Leikin S L, Chemomordik L V, Pastushenko V F and Sokirko A I 1988 Reversible electrical breakdown of lipid bilayers: formation and evolution of pores *Biochim. Biophys. Acta* **940** 275–87
- Gothelf A, Mir L M and Gehl J 2003 Electrochemotherapy: results of cancer treatment using enhanced delivery of bleomycin by electroporation *Canc. Treat. Rev.* **29** 371–87
- Grosse C and Schwan H P 1992 Cellular membrane potentials induced by alternating fields *Biophys. J.* **63** 1632–42
- Gunsalus I C and Stanier R Y 1960 *The Bacteria: A Treatise on Structure and Function* vol 1 (New York: Academic) pp 1–34
- Hoffman J F 1987 On the mechanism and measurement of shape transformations of constant volume of human red blood cells *Blood Cells* **12** 565–86
- Jeny R A, Popel A S and Brownell W E 1996 Potential distribution for a spheroidal cell having a conductive membrane in an electric field *IEEE Trans. Biomed. Eng.* **43** 970–2
- Marszalek P, Liu D-S and Tsong T Y 1990 Schwan equation and transmembrane potential induced by alternating electric field *Biophys. J.* **58** 1053–58
- Mir L M *et al* 1998 Effective treatment of cutaneous and subcutaneous malignant tumours by electrochemotherapy *Br. J. Cancer* **77** 2336–42
- Neumann E, Sowers A E and Jordan C A 1989 *Electroporation and Electrofusion in Cell Biology* (New York: Plenum)
- Neumann E, Toensing K, Kakorin S, Budde P and Frey J 1998 Mechanism of electroporative dye uptake by mouse B cells *Biophys. J.* **74** 98–108
- Parker K H and Winlove C P 1999 The deformation of spherical vesicles with permeable, constant-area membranes: application to the red blood cell *Biophys. J.* **77** 3096–107
- Radu M, Ionescu M, Irimescu N, Iliescu K, Pologea-Moraru R and Kovacs E 2005 Orientation behavior of retinal photoreceptors in alternating electric fields *Biophys. J.* **89** 3548–54
- Schwan H P 1983a Biophysics of the interaction of electromagnetic energy with cells and membranes *Biological Effects and Dosimetry of Nonionizing Radiation* ed M Grandolfo *et al* (New York: Plenum) pp 213–31
- Schwan H P 1983b Dielectric properties of biological tissue and cells at RF- and MW- frequencies *Biological Effects and Dosimetry of Nonionizing Radiation* ed M Grandolfo *et al* (New York: Plenum) pp 195–211
- Sekine K, Torii N, Kuroda C and Asami K 2002 Calculation of dielectric spectra of suspensions of rod-shaped cells using boundary element method *Bioelectrochemistry* **57** 83–7
- Smith K C, Neu J C and Krassowska W 2004 Model of creation and evolution of stable electropores for DNA delivery *Biophys. J.* **86** 2813–26
- Stille U 1944 Der Entmagnetisierungsfaktor und Entelektrisierungsfaktor für Rotationsellipsoide *Archiv Elektrotechnik* **38** 91–101 (in German)
- Stratton J A 1941 *Electromagnetic Theory* (New York: McGraw-Hill)
- Takashima S, Chang S and Asakura T 1985 Shape change of sickled erythrocytes induced by pulsed rf electrical fields *Proc. Natl Acad. Sci. USA* **82** 6860–64
- Tee G J 2004 Surface area and capacity of ellipsoids in  $n$  dimensions, Department of Mathematics, University of Auckland. Available online at: <http://www.citr.auckland.ac.nz/techreports/2004/CITR-TR-139.pdf>
- Tsong T Y 1991 Electroporation of cell membranes *Biophys. J.* **60** 297–306
- Valic B, Golzio M, Pavlin M, Schatz A, Faurie C, Gabriel B, Teisse J, Rols M-P and Miklavcic D 2003 Effect of electric field induced transmembrane potential on spheroidal cells: theory and experiment *Eur. Biophys. J.* **32** 519–28
- Warnke R 2003 Eine Approximationsfunktion zur Berechnung des Feldverstaerkungsfaktors sphaeroider Zellen *Laboratory Report (Forschungspraktikum)* Department of Biology, University of Rostock (in German)
- Zimmermann U and Neil G A 1996 *Electromanipulation of cells* (Boca Raton, FL: CRC Press)
- Zimmermann, U, Friedrich U, Mussauer H, Gessner P, Hämel K and Sukhorukov V 2000 Electromanipulation of mammalian cells: fundamentals and application *IEEE Trans. Plasma Sci.* **28** 72–82

## **Appendix D**

### **Submitted manuscript:**

Maswiwat K, Wachner D and Gimsa J 2007 Effects of cell orientation and electric field frequency on the transmembrane potential induced in ellipsoidal cells.  
(submitted)

---

## **Effects of cell orientation and electric field frequency on the transmembrane potential induced in ellipsoidal cells**

Running title:  $\Delta\phi$  in ellipsoidal cells

Kanokkan Maswiwat<sup>a</sup>, Derk Wachner<sup>b</sup>, and Jan Gimsa<sup>b,\*</sup>

<sup>a</sup>Department of Physics, Faculty of Science and Technology, Suratthani Rajabhat University, 84100, Suratthani, Thailand

<sup>b</sup>Chair of Biophysics, Institute of Biology, University of Rostock, Gertrudenstr. 11a, 18057, Rostock, Germany

\*Corresponding author: Tel: +49-381-498 6020, Fax: +49-381-498 6022

e-mail: [jan.gimsa@uni-rostock.de](mailto:jan.gimsa@uni-rostock.de)

### **Abstract**

The transmembrane potential ( $\Delta\phi$ ) induced by external electric fields is important both in biotech applications and in new medical therapies. We analyzed the effects of AC field frequency and cell orientation for cells of a general ellipsoidal shape. Simplified equations were derived for the membrane surface points where the maximum  $\Delta\phi$  is induced. The theoretical results were confirmed in experiments with three-axial chicken red blood cells (a: b: c=6.66 $\mu$ m: 4.17 $\mu$ m: 1.43 $\mu$ m). Propidium iodide (PI) staining and cell lysis were detected after an AC electropermeabilization (EP) pulse. The critical field strength for both effects increased when the shorter axis of a cell was parallel to the field, as well as at higher field frequency and for shorter pulse durations. Nevertheless, data analysis based on our theoretical description revealed that the  $\Delta\phi$  required is lower for the shorter axis, i.e. for smaller membrane curvatures. The critical  $\Delta\phi$  was independent of the field frequency for a given axis, i.e. the field strength had to be increased with frequency to compensate for the membrane dispersion effect. Comparison of the critical

field strengths of PI staining in a linear field aligned along semi-axis  $a$  ( $142 \text{ kV m}^{-1}$ ) and a field rotating in the  $a$ - $b$  plane ( $115 \text{ kV m}^{-1}$ ) revealed the higher EP efficiency of rotating fields.

**Keywords:** induced transmembrane potential, electroporation, electropermeabilization, lab-on-chip, chicken red blood cells

## 1. Introduction

Membrane electropermeabilization (EP, also referred to as electroporation or dielectric breakdown) is probably the most important technique for the introduction of extracellular molecules, which do not penetrate cell membranes under normal conditions. It is generally assumed that membrane re-conformation and the formation of aqueous pores play a decisive role in the process of penetration [1]. EP is observed when the transmembrane potential ( $\Delta\phi$ ) induced by the external field reaches a “critical voltage” of approximately 1 V [2-4]. Its magnitude depends on the experimental conditions [5, 6]. Nevertheless, thorough investigations have shown that the experimental observation of a “critical voltage” results from the strongly nonlinear auto-regulation processes involved in pore formation [7-9]. One important effect is the voltage drop in the external medium for the current flowing through the pore. This voltage drop increases with pore size, leading to a down-regulation of  $\Delta\phi$ . Nevertheless, the assumption of a “critical voltage” is feasible for practical reasons and we will use the term in the following.

EP of cells depends on several electric parameters, e.g. field strength, pulse duration, number of pulses [6, 10-17] and pulse shape [18-20]. Cell size, shape and orientation, medium conductivity and temperature are also important [6, 21-23].  $\Delta\phi$  is proportional to the length of the axis oriented in the field direction and a shape factor that is related to the depolarizing factors [23-25]. Chang et al. [26] described how AC-fields are more effective in EP than DC fields, and result in an increased cell viability. The frequency dependence of  $\Delta\phi$  in AC-fields depends on medium conductivity [22]. Capacitive membrane bridging causes the  $\Delta\phi$  to decrease with increasing field frequency

[4, 22, 27-34]. Clearly, rotating AC-fields generated by the superposition of two perpendicularly oriented fields are even more effective than the linear AC-fields [28, 35, 36]. New developments focus on EP in microfluidic devices with an EP process controlled at the single cell level [37, 38]. The aims are to achieve high effectiveness in the genetic manipulation of cells [39-43] and effective cell lysis prior to subcellular analysis [44].

Gimsa and Wachner [25, 45] have derived analytical expressions of  $\Delta\phi$  for both orientations of the symmetry axis of spheroidal cells, assuming a low conductive membrane and a highly polarizable cytoplasm. The same ansatz could be extended to arbitrarily oriented cells of the general ellipsoidal shape, including all electrical parameters [30]. Recently, we derived simplified expressions avoiding the complex depolarizing factors for spheroidal cells [46].

In this work, we analyze the  $\Delta\phi$  induced by AC field pulses in arbitrarily oriented ellipsoidal cells. The theoretical description is compared to experimental results obtained from the EP of the roughly ellipsoidal chicken red blood cells (CRBCs). Experiments were conducted in a chip chamber with two comb-shaped electrodes. Each comb had three interdigitating fingers, allowing for five different inter-electrode distances. The EP of the cells was determined from the two criteria, propidium iodide (PI) permeabilization detected by fluorescence-staining of the cell nuclei and cell lysis, respectively. We considered the effects of field strength, pulse field frequency, pulse duration and cell orientation.

## 2. Theory

### 2.1. $\Delta\phi$ for general orientation of ellipsoidal cells

#### *2.1.1. A finite element ansatz for $\Delta\phi$ of the oriented single shell model*

Gimsa and Wachner [30] have presented a simplified finite element ansatz for the  $\Delta\phi$  of a single shell ellipsoidal model. The model consists of the internal, membrane and external media, designated by the indices  $i$ ,  $m$  and  $e$ , respectively. Each medium is presented by a

prismatic element (Fig. 1). The impedance  $Z^*$  of each element is given by the geometry (cross-sectional area  $A$  and length  $l$ ):

$$Z^* = \frac{1}{\sigma^*} \frac{l}{A} \quad \text{with} \quad \sigma^* = \sigma + j \omega \varepsilon \varepsilon_0 \quad (1)$$

$\sigma^*$ ,  $\varepsilon$ ,  $\varepsilon_0$  and  $j$  stand for the complex specific conductivity of the considered medium, relative permittivity, permittivity of vacuum and  $\sqrt{-1}$ , respectively. Equation (1) is equivalent to an resistor capacitor- (RC-) pair (see lump model in Fig. 1). The length  $l$  in equation (1) is given by the dimensions according to Fig. 1. The cross-sectional areas  $A$  of each element are assumed to be equal and infinitely small. Starting from this "finite element model", for an ellipsoidal cell with semiaxis  $a$  oriented in parallel to the field direction  $\Delta\phi$  at pole  $a$  can be expressed by the voltage divider properties of the lump model (Fig. 1; see [30] for details):

$$\begin{aligned} \Delta\phi_a &= aE_{loc,a} - aE_{i,a} \\ &= \frac{(Z_{i,a}^* + Z_m^*) \phi_a^{\max}}{Z_{i,a}^* + Z_m^* + Z_{e,a}^*} - \frac{Z_{i,a}^* \phi_a^{\max}}{Z_{i,a}^* + Z_m^* + Z_{e,a}^*} \\ &= \frac{Z_m^*}{Z_{i,a}^* + Z_m^* + Z_{e,a}^*} a_{\text{infl}} E_x \end{aligned} \quad (2)$$

$E_x$ ,  $E_{loc,a}$  and  $E_{i,a}$  stand for the external field in  $x$ -direction, the effective internal local field of the body and the cytoplasmic field, respectively.  $\phi_a^{\max}$  stands for the maximum of  $\phi_{loc,a}$  determined by the influential radius  $a_{\text{infl}}$  along axis  $a$  (Fig. 1). Index  $a$  refers to the geometry along semiaxis  $a$ . No axis index is required for the membrane impedance because the membrane elements are assumed to possess the same geometry along each principal axis. Please note that the model is largely consistent or even superior over the Laplace-description for reasonable cell properties [30].



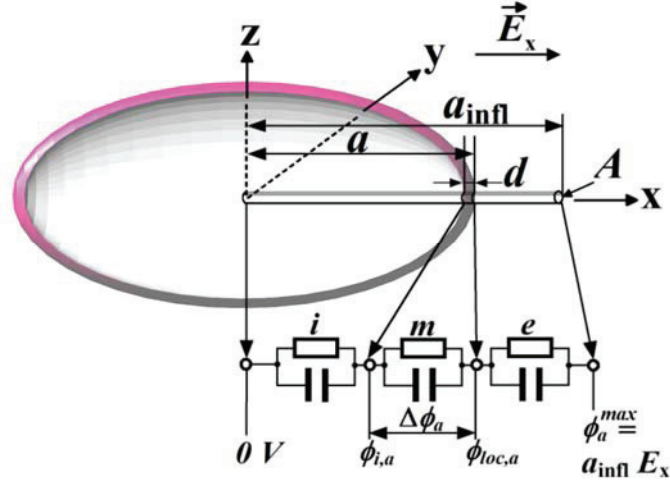


**Fig. 1.** Oriented single-shell model of a general ellipsoidal cell with sketches of the three finite elements and RC-descriptions for cytoplasm ( $i$ ), membrane ( $m$ ) and external medium ( $e$ ), respectively.  $A$ ,  $d$ ,  $a$  and  $a_{\text{infl}}$  stand for cross-sectional area, membrane thickness, the semi-axis length and influential radius along semi-axis  $a$ , respectively.  $E_x$ ,  $\Delta\phi$ ,  $\phi_i$ ,  $\phi_{\text{loc}}$  and  $\phi_{\text{max}}$  denote the external field strength, the induced transmembrane potential, the cytoplasmic pole potential, the actual potential at the surface and the maximum potential at the surface, respectively. A potential of 0 V is assumed at the center for reasons of symmetry.

### 2.1.2. $\Delta\phi$ for arbitrarily oriented cells of the general ellipsoidal shape

The general ellipsoidal model is described by three principal semi-axes  $a$ ,  $b$ , and  $c$  of different length. Special cases are spheroidal models with  $a = b$  and spherical ones with  $a = b = c$ . The semi-axes can be used to determine a Cartesian, orthonormal coordinate system  $x$ ,  $y$ , and  $z$  where  $x$ ,  $y$ , and  $z$  are parallel to  $a$ ,  $b$ , and  $c$ , respectively (Fig. 2). The homogeneous external field  $E$  is oriented arbitrarily within this coordinate system. Its orientation is determined by the angles  $\delta$  and  $\gamma$ . The local vector  $P$  of the membrane point under consideration is determined by the angles  $\alpha$  and  $\beta$ . The induced transmembrane potential ( $\Delta\phi_p$ ) at a membrane point (index  $p$ ) is:

$$\Delta\phi_p = \begin{pmatrix} \frac{Z_m^*}{Z_{i,a}^* + Z_m^* + Z_{e,a}^*} \frac{a_{\text{infl}}}{a} E_x d_x \\ \frac{Z_m^*}{Z_{i,b}^* + Z_m^* + Z_{e,b}^*} \frac{b_{\text{infl}}}{b} E_y d_y \\ \frac{Z_m^*}{Z_{i,c}^* + Z_m^* + Z_{e,c}^*} \frac{c_{\text{infl}}}{c} E_z d_z \end{pmatrix} = \begin{pmatrix} \Delta\phi_a \frac{d_x}{a} \\ \Delta\phi_b \frac{d_y}{b} \\ \Delta\phi_c \frac{d_z}{c} \end{pmatrix} \quad (3)$$

for an arbitrary orientation of the inducing field (see [30] for details).  $a_{\text{infl}}$ ,  $b_{\text{infl}}$  and  $c_{\text{infl}}$  stand for the influential radii of the ellipsoidal cell. The influential radius along each semiaxis refers to a certain distance from the center of the cell [45]. In the center, a symmetry plane can be defined for each semiaxis that is oriented perpendicular to the semiaxis. Field components ( $E_x$ ,  $E_y$ ,  $E_z$ ) parallel to a semiaxis will not change the potential in the respective symmetry plane for symmetry reasons. The  $\Delta\phi$ -components at the three poles  $a$ ,  $b$ , and  $c$  are solely induced by the respective field components ( $E_x$ ,  $E_y$ ,  $E_z$ ) along the semiaxes.  $d_x$ ,  $d_y$ , and  $d_z$  denote the distance of the membrane point to the three symmetry planes (see Fig. 1 and [30] for more details). At the poles  $d_x=a$ ,  $d_y=b$ , and  $d_z=c$ . Neglecting the permittivities of the cytoplasm and the external medium, from equation (3) we obtain [45]:

$$\Delta\phi_p = \frac{a_{\text{infl}} E_x d_x / a}{(1 + a g_m (1/\sigma_i + (a_{\text{infl}} - a)/a\sigma_e))\sqrt{1 + f^2 / f_{c,a}^2}} + \frac{b_{\text{infl}} E_y d_y / b}{(1 + b g_m (1/\sigma_i + (b_{\text{infl}} - b)/b\sigma_e))\sqrt{1 + f^2 / f_{c,b}^2}} + \frac{c_{\text{infl}} E_z d_z / c}{(1 + c g_m (1/\sigma_i + (c_{\text{infl}} - c)/c\sigma_e))\sqrt{1 + f^2 / f_{c,c}^2}} \quad (4)$$

with

$$f_{c,a} = \frac{1}{2\pi C_m} \left( \frac{\sigma_e \sigma_i}{a\sigma_e + (a_{\text{infl}} - a)\sigma_i} + g_m \right) \quad (5)$$

$C_m$  and  $g_m$  stand for the area-specific membrane capacitance in  $\text{Fm}^{-2}$  and the area-specific membrane conductance in  $\text{Sm}^{-2}$ , respectively. They are given by  $C_m = \epsilon_0 \epsilon_m / d$  and  $g_m = \sigma_m / d$  with  $d$  being the membrane thickness.  $f$ ,  $f_{c,a}$ ,  $\sigma_i$ , and  $\sigma_e$  stand for the external field

frequency, the characteristic frequency of membrane polarization along semiaxis  $a$ , and the internal and external conductivities, respectively. Expressions analogous to (5) hold along the other two semiaxes.

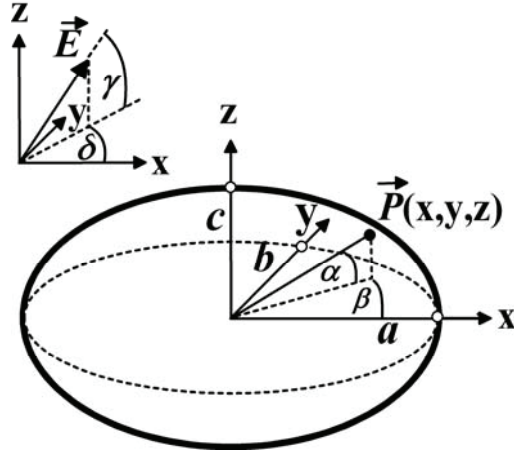


**Fig. 2.** Sketch of a cell of the general ellipsoidal shape. The components of  $\vec{P}$  and  $\vec{E}$  are given in spherical coordinates. The principal semi-axes  $a$ ,  $b$  and  $c$  define the orthonormal coordinate system,  $x$ ,  $y$  and  $z$ .  $\vec{P}(x, y, z)$  is the local vector of a membrane surface point defined by the angles  $\alpha$  and  $\beta$ . The external electric field  $\vec{E}$  has an arbitrary orientation, determined by the angles  $\delta$  and  $\gamma$ .

### 2.1.3. Maximum of $\Delta\phi_p$ for semiaxis $b$ being oriented perpendicular to the external field

The field vector is parallel to the  $x$ - $z$  plane for semiaxis  $b$  being orientated perpendicular to the external field ( $\delta = 0^\circ$ , Fig. 3A). A new analytical expression can be derived from equation (3) for the membrane surface point reaching the maximum  $\Delta\phi$  if only peripheral points in the  $a$ - $c$  plane ( $\beta = 0^\circ$ ) are considered. The angle  $\alpha_{(\Delta\phi_{\max})}$  determining this point can be obtained from the first derivative of equation (3) for  $|E_x|=|E_z|$ :

$$\alpha_{(\Delta\phi_{\max})} = \arctan \left( \frac{|\Delta\phi_c^*| c}{|\Delta\phi_a^*| a} \tan \gamma \right) \quad (6)$$

Introducing  $\alpha_{(\Delta\phi_{\max})}$  into equation (3) leads to the maximum of  $\Delta\phi$ :

$$\Delta\phi^{\max} = \sqrt{|\Delta\phi_a^*|^2 \cos^2 \gamma + |\Delta\phi_c^*|^2 \sin^2 \gamma} \quad (7)$$

Analogous expressions hold for fields oriented in the  $x$ - $y$  and  $y$ - $z$  planes. In these cases, the field orientation and the membrane point under consideration will be defined by the angles  $\delta$  and  $\beta$ , respectively (Fig. 3B). Analogous expressions hold for fields oriented in the  $x$ - $y$  and  $y$ - $z$  planes. In these cases, the field orientation and the membrane point under consideration will be defined by the angles  $\delta$  and  $\beta$ , respectively (Fig. 3B).

## 2.2. DC-limit of $\Delta\phi_p$ for oriented ellipsoidal cells with zero membrane conductance

### 2.2.1. General orientation of a cell of the general ellipsoidal shape

For zero membrane conductance and at very low frequency or DC fields, equation (3) can be reduced to:

$$\Delta\phi_p = \frac{a_{\text{infl}}}{a} E_x d_x + \frac{b_{\text{infl}}}{b} E_y d_y + \frac{c_{\text{infl}}}{c} E_z d_z \quad (8)$$

After introduction of the distances  $d_x$ ,  $d_y$ , and  $d_z$  and field components  $E_x$ ,  $E_y$  and  $E_z$  into equation (3) we obtain the complete form:

$$\Delta\phi_p = \frac{E abc}{\sqrt{(a^2 \sin^2 \beta + b^2 \cos^2 \beta) c^2 \cos^2 \alpha + a^2 b^2 \sin^2 \alpha}} \begin{pmatrix} a_{\text{infl}} \cos \alpha \cos \beta / a \\ b_{\text{infl}} \cos \alpha \sin \beta / b \\ c_{\text{infl}} \sin \alpha / c \end{pmatrix} \begin{pmatrix} \cos \gamma \cos \delta \\ \cos \gamma \sin \delta \\ \sin \gamma \end{pmatrix} \quad (9)$$

### 2.2.2. $\Delta\phi_p$ for a perpendicular orientation of semiaxis $b$ to the external field

For semiaxis  $b$  being oriented perpendicular to the external field, equation (9) can be reduced to:

$$\Delta\phi_p = \frac{E (a_{\text{infl}} c \cos \gamma \cos \alpha + c_{\text{infl}} a \sin \gamma \sin \alpha)}{\sqrt{a^2 \sin^2 \alpha + c^2 \cos^2 \alpha}} \quad (10)$$

considering only peripheral points in the  $a$ - $c$  plane (Fig. 3A). The angle  $\alpha_{(\Delta\phi^{\max})}$  determining  $\Delta\phi^{\max}$  is given by (compare to equation (6)):

$$\alpha_{(\Delta\phi^{\max})} = \arctan \left( \frac{c_{\text{infl}} c}{a_{\text{infl}} a} \tan \gamma \right) \quad (11)$$

and after introducing  $\alpha_{(\Delta\phi^{\max})}$  into equation (10) we obtain (compare to equation (7)):

$$\Delta\phi^{\max} = E\sqrt{a_{\text{infl}}^2 \cos^2 \gamma + c_{\text{infl}}^2 \sin^2 \gamma} \quad (12)$$

Equations (11) and (12) indicate that the  $\Delta\phi^{\max}$  of ellipsoidal cells for the above simplifications depends on field orientation ( $\gamma$ ) and cell shape, i.e. the influential radii along semiaxes  $a$  and  $c$  (Fig. 3A). Analogous expressions hold for the peripheral points of the  $a$ - $b$  (Fig. 3B) and  $b$ - $c$  planes.

### 2.3. DC-limit of $\Delta\phi_p$ for oriented spheroidal cells with zero membrane conductance

#### 2.3.1 General orientation of a spheroidal cell

Spheroidal models are oblate and prolate when their symmetry axes are shorter ( $c < a = b$ ) and longer ( $c > a = b$ ) than the semiaxes  $a$  and  $b$ , respectively. For arbitrarily oriented spheroidal cells  $\Delta\phi_p$  is given by [45]:

$$\Delta\phi_p = \frac{a_{\text{infl}}}{a} (E_x d_x + E_y d_y) + \frac{c_{\text{infl}}}{c} E_z d_z \quad (13)$$

The complete form is (compare to equation (3)):

$$\Delta\phi_p = \frac{E a c}{\sqrt{(a^2 \sin^2 \alpha + c^2 \cos^2 \alpha)}} \begin{pmatrix} a_{\text{infl}} \cos \alpha \cos \beta / a \\ a_{\text{infl}} \cos \alpha \sin \beta / a \\ c_{\text{infl}} \sin \alpha / c \end{pmatrix} \begin{pmatrix} \cos \gamma \cos \delta \\ \cos \gamma \sin \delta \\ \sin \gamma \end{pmatrix} \quad (14)$$

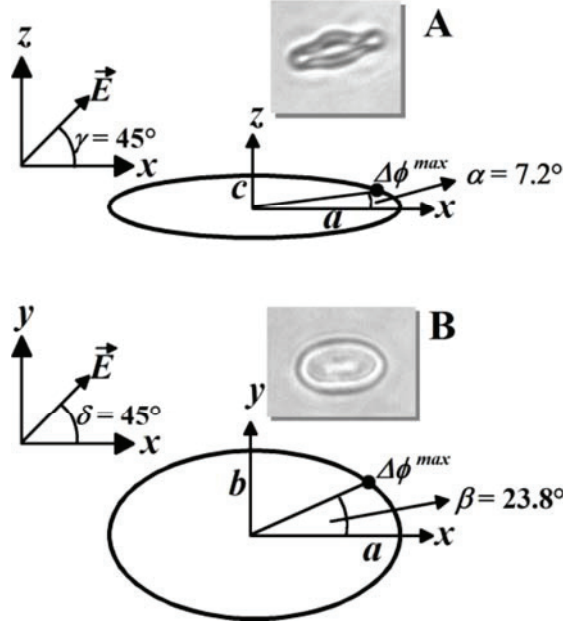


**Fig. 3.** Two-dimensional sketches of the ellipsoidal CRBC model compared to microscopic images of CRBCs in the measuring solution. The sketches resemble a situation of a  $45^\circ$  field orientation in the  $a$ - $c$  (A) and  $a$ - $b$  (B) planes ( $\delta = \gamma = 45^\circ$ ).  $\alpha$  and  $\beta$  determine the theoretical membrane points of  $\Delta\phi^{\max}$ . (A) field orientation perpendicular to semiaxis  $b$  ( $\delta = 0^\circ$ ). (B) experimental standard situation, field orientation perpendicular to the shortest semiaxis  $c$  ( $\gamma = 0^\circ$ , compare to Fig. 13).

### 2.3.2. $\Delta\phi_p$ at peripheral membrane points with a perpendicular orientation of semiaxes $b$ to the external field for a spheroidal cell

For  $\delta = 0^\circ$  the field vector lies in  $x$ - $z$  plane. If we further assume  $\beta = 0^\circ$ ,  $\Delta\phi_p$  in equation (9) can be reduced to equation (10). Nevertheless,  $a_{\text{infl}}$  and  $c_{\text{infl}}$  are based on complex expressions for the depolarizing factors [45]. Recently, we derived simple approximating equations for  $a_{\text{infl}}$  and  $c_{\text{infl}}$  of spheroids (equations (A.1) and (A.2)) avoiding complex expressions. Introducing these expressions into equation (10) leads to:

$$\Delta\phi_p = \left( \frac{a E (a+2c) (2c \cos \gamma \cos \alpha + (a+c) \sin \gamma \sin \alpha)}{2(a+c) \sqrt{a^2 \sin^2 \alpha + c^2 \cos^2 \alpha}} \right) \quad (15)$$

The same expressions can be introduced into equations (11) and (12) to determine the  $\Delta\phi^{\max}$  and the angle  $\alpha_{(\Delta\phi^{\max})}$  under which it occurs. Furthermore, limiting cases of the shape are considered. For a thin disk ( $c \ll a$ ) equation (15) reduces to:

$$\Delta\phi_p = \frac{aE(2c \cos\gamma \cos\alpha + a \sin\gamma \sin\alpha)}{2\sqrt{a^2 \sin^2\alpha + c^2 \cos^2\alpha}} \quad (16)$$

For long cylindrical cells ( $c \gg a$ ),  $\Delta\phi_p$  becomes:

$$\Delta\phi_p = \frac{acE(2 \cos\gamma \cos\alpha + \sin\gamma \sin\alpha)}{\sqrt{a^2 \sin^2\alpha + c^2 \cos^2\alpha}} \quad (17)$$

### 2.3.3. $\Delta\phi_p$ for peripheral membrane points for a perpendicular orientation of symmetry axis $c$ to the field for a spheroidal cell

$\delta$  is equal to  $\beta_{(\Delta\phi^{\max})}$  for any  $\gamma$  because of the axis-symmetry of spheroids. For  $\gamma = 0^\circ$ , the field vector is parallel to the  $x$ - $y$  plane. The peripheral points of spheroids ( $a = b$ ) form circles in this plane, i.e. for  $\alpha = 0^\circ$ ,  $\Delta\phi_a^{\max}$  is always given by  $a_{\text{infl}} E$ . Using equation (A.1) we obtain [46]:

$$\Delta\phi_a^{\max} = aE \left( \frac{a + 2c}{a + c} \right) \quad (18)$$

For the limiting case of a very thin disk ( $c \ll a$ ), equation (18) becomes  $\Delta\phi_a^{\max} = aE$ . For an extreme prolate shape ( $c \gg a$ ), the geometry approaches a cylinder and  $\Delta\phi_c^{\max} = 2aE$ .

## 3. Materials and methods

### 3.1. Theoretical analysis of the model behavior

We used Maple 9.5 (Maplesoft, Waterloo Maple Inc., Canada) for calculations. Curves were plotted with SigmaPlot 9.0 (Systat Software GmbH, Germany). The cells were modeled as general single shell ellipsoids ( $a > b > c$ ), spheres ( $a = b = c$ ) and oblate ( $c < a = b$ ) or prolate ( $c > a = b$ ) spheroids. An electric field strength of  $100 \text{ kV m}^{-1}$  was assumed for theoretical considerations. Electric CRBC parameters are given in Table 1. In experiments, a sufficient number of cells could only be found with the orientation  $\gamma =$

$0^\circ$ ,  $\alpha = 0^\circ$  (Fig. 3B). The orientation  $\delta = 0^\circ$ ,  $\beta = 0^\circ$  was not stable enough for reliable data analysis (Fig. 3A).

**Table 1** CRBC parameters of for model calculations [47]. The influential radii were calculated from the depolarizing factors of general ellipsoids [30]. The quotient of influential radius and semiaxes length is the maximal amplification factor for the induced  $\Delta\phi$ .

Parameter	Value
Infl. radius/semiaxis = max. ampl. factor	
$a_{\text{infl}} / a$	7.49 $\mu\text{m}$ / 6.66 $\mu\text{m}$ = 1.125
$b_{\text{infl}} / b$	5.28 $\mu\text{m}$ / 4.17 $\mu\text{m}$ = 1.266
$c_{\text{infl}} / c$	4.43 $\mu\text{m}$ / 1.43 $\mu\text{m}$ = 3.098
Membrane thickness ( $d$ )	8 nm
Conductivity / relative permittivity	
Internal: $\sigma_i / \varepsilon_i$	0.36 S $\text{m}^{-1}$ / 50
Membrane: $\sigma_m / \varepsilon_m$	28 $\mu\text{S}$ $\text{m}^{-1}$ / 22.59
External: $\sigma_e / \varepsilon_e$	0.12 S $\text{m}^{-1}$ / 78.5
Area specific membrane conductance ( $g_m$ )	3500 S $\text{m}^{-2}$
Area specific membrane capacitance ( $C_m$ )	0.025 F $\text{m}^{-2}$



**Table 2** Shape parameters of a spheroidal model for theoretical considerations

Semiaxes	Influential radii calculated from	
	Depolarizing factors	Simplified equations (appendix)
Spherical model		
$a=b=c=3.5 \mu\text{m}$	$5.25 \mu\text{m}$	$5.25 \mu\text{m}$
Spheroidal model		
$c:a = 1:3.5$ (oblate)		
$a_{\text{infl}}=b_{\text{infl}}$	$4.18 \mu\text{m}$	$4.28 \mu\text{m}$
$c_{\text{infl}}$	$3.06 \mu\text{m}$	$2.75 \mu\text{m}$
$c:a = 2:1$ (prolate)		
$a_{\text{infl}}=b_{\text{infl}}$	$5.96 \mu\text{m}$	$5.83 \mu\text{m}$
$c_{\text{infl}}$	$8.47 \mu\text{m}$	$8.75 \mu\text{m}$

### 3.2. Electropermeabilization (EP) experiments

#### 3.2.1. EP chip chamber and instrumentation

A glass chip with two comb-shaped platinum electrodes with three fingers was used for EP experiments. Our new design allowed for five different inter-electrode gaps of  $80 \mu\text{m}$ ,  $100 \mu\text{m}$ ,  $150 \mu\text{m}$ ,  $300 \mu\text{m}$  and  $450 \mu\text{m}$  generating five electric field strengths from the same supply voltage (Fig. 4). The chips were fabricated by GeSiM GmbH, Grosserkmannsdorf, Germany ([www.gesim.de](http://www.gesim.de)). Only the three shortest distances ( $80 \mu\text{m}$ ,  $100 \mu\text{m}$  and  $150 \mu\text{m}$ ) were used in the CRBC experiments. The AC fields were generated by two  $180^\circ$ -phase shifted square-topped signals with a key ratio of 1:1 from a function generator HP 8130A (Hewlett Packard GmbH, Germany). The parameters of the generator were controlled by a computer program. The output voltage could be amplified up to  $20 V_{\text{pp}}$  at frequencies up to  $60 \text{ MHz}$  by a home made amplifier. A pulse generator HP 8116A (Hewlett Packard GmbH, Germany) was used to generate the gating signal for the HP 8130A function generator. Waveform and amplitude of the AC-fields were

monitored with an oscilloscope HP 54610B (Hewlett Packard GmbH, Germany). The resistances of the on-chip temperature sensors were calibrated for their temperature dependencies and measured before and after pulse application by a multimeter (model 2000, Keithley Instruments Inc., USA).

After the EP pulse, a short temperature increase has been observed with a maximum of 0.9 degrees for the longest pulse duration of 200ms. The temperature peak was observed approx. 50 s after the pulse. The main reason for this behavior was the heat dissipation by the terminating resistors. The temperature approached room temperature approx. one minute after the peak.

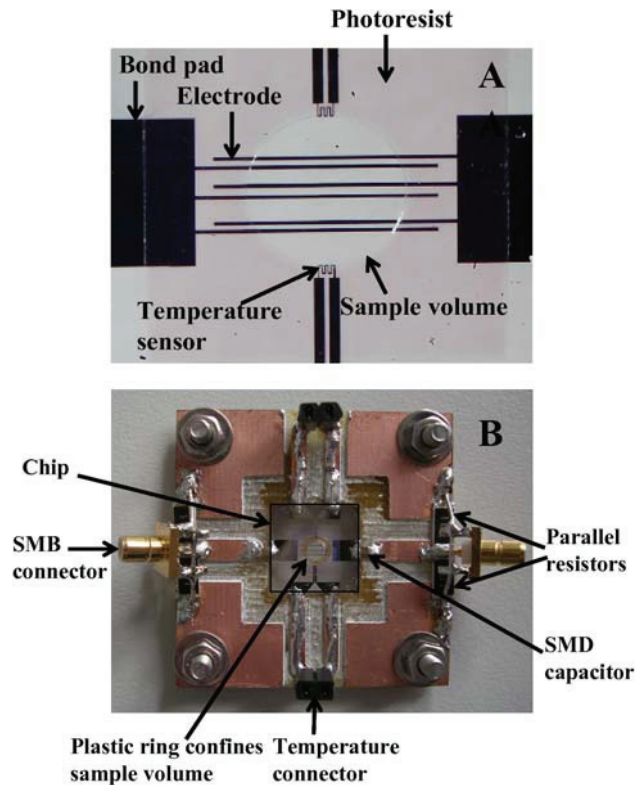


**Fig. 4.** Electrode glass chip (A;  $7 \times 7 \text{ mm}^2$ ) and chip carrier (B) for EP experiments. Two SMD capacitors ( $0.1 \mu\text{F}$ ) were each soldered to two parallel  $100 \Omega$  resistors and the SMB connector (impedance  $50 \Omega$ ). Finally, the SMD capacitors were glued (conductive glue, Conrad Electronic GmbH, Germany) to the bond pads of the chip electrodes. The temperature sensor was a platinum meander-structure. The plastic ring in the center of the chamber was glued to the photoresist to confine the sample volume ( $7 \mu\text{l}$ ). The chamber was sealed by a cover slip during measurements.

### 3.2.2. Electric field in the chamber

The electric field strength ( $E$ ) is given by a Fourier series for a square-wave AC-pulse with a key ratio of 1:1 [36]:

$$E = \frac{4V_{ss}}{\pi d} [\exp(j\omega t) - \exp(-j3\omega t)/3 + \exp(j5\omega t)/5 - \dots + \dots] \quad (19)$$

$d$ ,  $V_{ss}$ ,  $j$ ,  $\omega$  and  $t$  stand for the distance of a pair of plane-parallel electrodes, the voltage difference between the electrodes,  $\sqrt{-1}$ , the circular frequency, and time, respectively. The Fourier series contains only odd harmonics. The effective field of the full series is  $V_{ss}/d$ , the effective field generated by the sinusoidal first harmonic is  $2\sqrt{2} V_{ss}/(\pi d)$  leaving a missing 9.94% contribution for all other harmonics of the series. The missing contribution decreases to 5.05% and 3.36% when the third and fifth harmonics are included in the series. These considerations may be interesting in the frequency range of membrane dispersion when capacitive membrane bridging reduces the induced transmembrane potential with increasing frequency, i.e. membrane dispersion leads to a relatively stronger decrease in the contributions of the higher harmonics.

### 3.2.3. Cells and sample preparations

CRBCs were chosen because of their 3-axial ellipsoidal shape. Fig. 5 presents micrographs of the cells (Scanning Electron Microscope, DSM 960A, Carl Zeiss, Oberkochen, Germany). The cells were obtained from the BfR (Bundesinstitut für Risikobewertung, Berlin, Germany). Fresh blood samples taken from the wing vein of Italian cocks were preserved at a 1:1 dilution in Alsever's solution (18.66 g dextrose, 4.18 g NaCl and 8.0 g tri-Na-citrate-2-hydrate dissolved in 1 liter distilled water, pH 6.1) as an anticoagulant. This suspension had a cell concentration of approx. 19% v/v. It was stored no longer than three days. Cells were suspended in a mixture of a sucrose and a NaCl solution for experiments. Both solutions had an osmolarity of 300 mOsm and contained 1 mM phosphate buffer solution, pH 6.8. The mixture was adjusted to a medium conductivity of 0.12 S/m. The conductivity was controlled by a conductometer

(inoLab, WTW GmbH, Weilheim, Germany) in the temperature compensation mode (20°C).

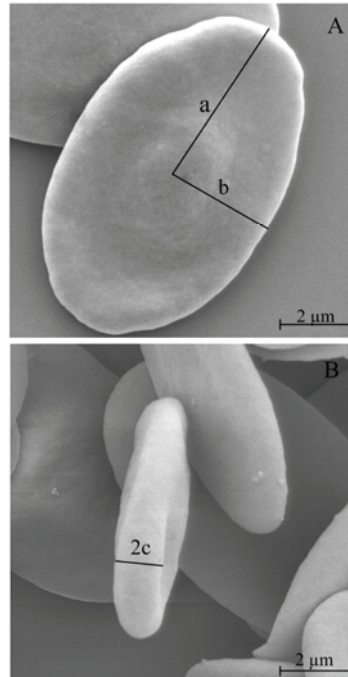


**Fig. 5.** SEM-micrographs of slightly shrunken CRBCs, magnification 10 000 x. (A) and (B) show different orientations of the cells. The semi-axes are denoted.

#### **3.2.4. EP experiments**

PI (Fluka, Switzerland, molecular weight 668.39) binds to DNA and is used as a fluorescence marker of cell nuclei [48]. Cells were suspended in 5 ml measuring solution containing 10 μM PI [36]. 7 μl of this suspension with a cell concentration of 0.03% v/v were transferred to the measuring chamber that was sealed by a cover slip. EP experiments were conducted with sedimented cells a few minutes after transfer. The uptake of PI by single cells was observed with a fluorescence microscope (Olympus IX71, Japan). The images were recorded on hard disk and monitored by a computer interface using the Cell-P program of our imaging system (Soft Imaging System GmbH, Germany). Cells already stained before pulse application were excluded from interpretation. EP was judged 3 min after pulse application. Non-lysed cells did not lose

their hemoglobin content. PI permeabilized cells detected by fluorescence-staining of their nuclei and non-permeabilized cells were distinguished amongst the non-lysed cells. Data were obtained for 10-15 cells collected in 4-5 repeats for each experimental condition.

## 4. Results and Discussions

### 4.1. Theoretical analysis

#### 4.1.1. DC-limit of $\Delta\phi_p$ for cells of the general ellipsoidal shape with zero membrane conductance

The following analysis is based on the theoretical descriptions introduced above. Table 1 presents the CRBC parameters used. In the experiments, cells were oriented with semiaxes  $b$  or  $c$  perpendicular to the external field (Figs. 3A and B). For the first orientation,  $\delta = 0^\circ$  and  $\beta = 0^\circ$  for peripheral points in the  $a$ - $c$  plane (see Figs. 2 and 3A). The  $\Delta\phi_p$  of any point depends on the field angle  $\gamma$ . Maxima at the poles are special cases of equation (3) and given for a parallel orientation of the field and semiaxes  $a$  ( $\Delta\phi_a^{\max} = a_{\text{infl}} E$ ) and  $c$  ( $\Delta\phi_c^{\max} = c_{\text{infl}} E$ ), respectively. At a field angle of  $\gamma = 45^\circ$  (Fig. 3A) equation (12) becomes:

$$\Delta\phi_{a,c}^{\max} = (\sqrt{2}/2) E \sqrt{(a_{\text{infl}}^2 + c_{\text{infl}}^2)} \quad (20)$$

Analogous expressions are obtained for cell orientations in the  $a$ - $b$  and  $b$ - $c$  planes. It can be shown that the equation holds for cell models with a very thin membrane, zero membrane conductance, and a highly conductive cytoplasm at low frequencies. Under these conditions, the membrane point of  $\Delta\phi^{\max}$  is solely determined by the object geometry. We therefore designated the angle of this membrane point “geometry-determined limiting angle”.  $\alpha_{(\Delta\phi_{a,c}^{\max})} = 7.2^\circ$  is obtained for the geometric parameters of Table 1 (Fig. 6A).  $\beta_{(\Delta\phi_{a,b}^{\max})}$  is  $23.78^\circ$  in the  $a$ - $b$  plane (Fig. 6B).

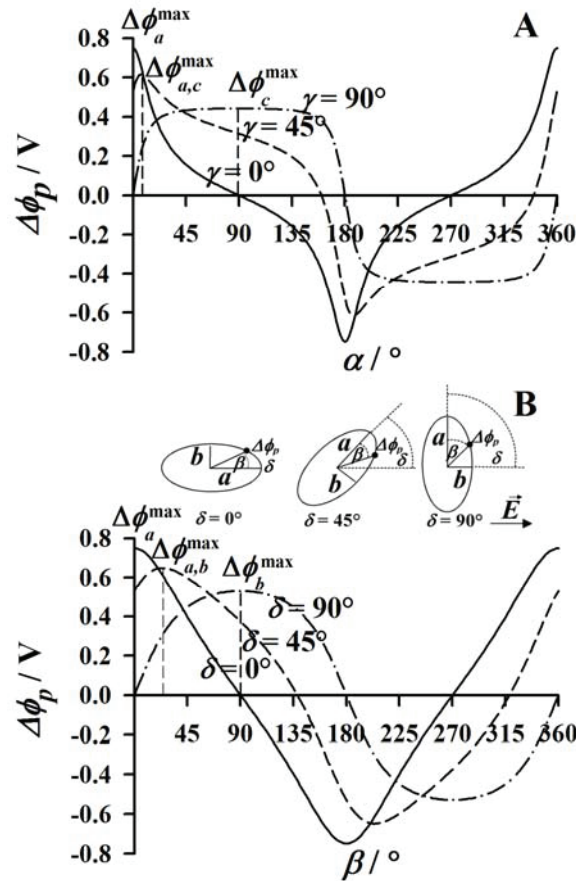


**Fig. 6.** Angle dependence of  $\Delta\phi_p$  for the CRBC model with zero membrane conductance (DC-limit). (A) dependence of  $\alpha$  for peripheral points ( $\beta = 0^\circ$ ) for a field orientation perpendicular to semiaxis  $b$  ( $\delta = 0^\circ$ ). Three field orientations ( $\gamma = 0^\circ$ ,  $\gamma = 45^\circ$  and  $\gamma = 90^\circ$ ) are considered in the  $a$ - $c$  plane. (B) dependence of  $\beta$  for peripheral points ( $\alpha = 0^\circ$ ) for a field orientation perpendicular to semiaxis  $c$  ( $\gamma = 0^\circ$ ). Three field orientations ( $\delta = 0^\circ$ ,  $\delta = 45^\circ$  and  $\delta = 90^\circ$ ) are considered in the  $a$ - $b$  plane.

#### 4.1.2. DC-limit of $\Delta\phi_p$ of oriented spheroidal cells with zero membrane conductance

We consider the spheroidal shape in the following for the sake of completeness. Semiaxes  $a$  and  $b$  were fixed to a typical cell value of  $3.5 \mu\text{m}$ . Semiaxis  $c$  was varied. Three axes ratios were considered,  $c:a = 1:1$  (spherical),  $c:a = 1:3.5$  (oblate), and  $c:a = 2:1$  (prolate). A field orientation perpendicular to semiaxis  $b$  ( $\delta = 0^\circ$ ) can be assumed

without limitation in generality.  $\Delta\phi_p$  of the peripheral membrane points ( $\beta=0^\circ$ ) was calculated either by the full model (equation (10)) using exact influential radii (Table 2) or by the simplified equation (15) (Fig. 7). The  $\Delta\phi^{\max}$  values were found at the poles of semiaxis  $a$  ( $\alpha=0^\circ$ ) and  $c$  ( $\alpha=90^\circ$ ) for field orientations in parallel ( $\gamma=0^\circ$ , Fig. 7A) and perpendicular ( $\gamma=90^\circ$ , Fig. 7C) to semiaxis  $a$ . For  $\gamma=45^\circ$ ,  $\Delta\phi^{\max}$  can be expressed in analogy to equation (20) (Fig. 7B). For a field orientation perpendicular to semiaxis  $c$  ( $\gamma=0^\circ$ ),  $\Delta\phi^{\max}=a_{\text{infl}}E$  for all angles in the  $a$ - $b$  plane (Fig. 7D). The errors of the simplified equations for prolate and oblate shapes are usually much smaller than 10% compared to the full model (Fig. 7).

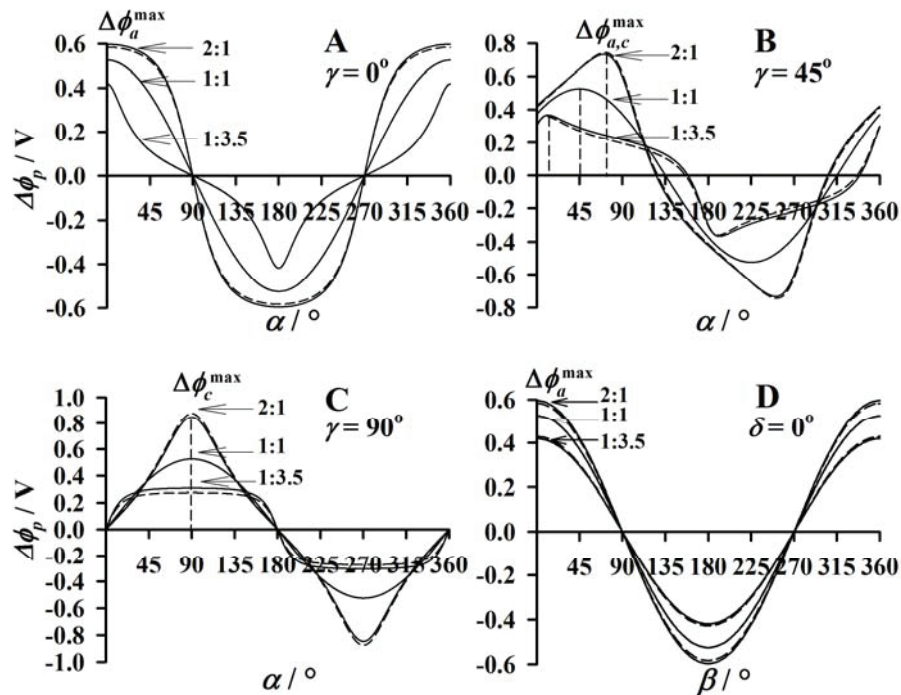


**Fig. 7.** Comparison of the DC-limits of  $\Delta\phi_p$  for the full (equation (10), solid lines) and simplified (equation (15), dashed lines) spheroidal models. Zero membrane conductance was assumed. (A-C):  $\Delta\phi_p$  dependence on  $\alpha$  for peripheral membrane points in  $a$ - $c$  plane ( $\beta=0^\circ$ ) for semiaxis  $b$  perpendicular to the field ( $\delta=0^\circ$ ). The field orientations is  $\gamma=0^\circ$  (A),  $\gamma=45^\circ$  (B) and  $\gamma=90^\circ$  (C). (D): trivial case of a field orientation perpendicular to the symmetry axis  $c$  ( $\gamma=0^\circ$ ,  $\delta=0^\circ$ ). The  $\Delta\phi_p$  dependence on  $\beta$  is a cosine function for peripheral membrane points in the  $a$ - $b$  plane ( $\alpha=0^\circ$ ). The  $\Delta\phi_p$  magnitude is higher for prolate than for oblate cells.

### ***4.1.3. Dependence of the angle of $\Delta\phi^{\max}$ on cell parameters and frequency for tilted cells of the general ellipsoidal shape***

The site of  $\Delta\phi^{\max}$  depends on cell and medium parameters when the object is exposed to the field under a certain angle. For a qualitative consideration we used two different field orientations  $\delta=45^\circ$  ( $\gamma=0^\circ$ : field in  $a$ - $b$  plane), as well as  $\gamma=45^\circ$  ( $\delta=0^\circ$ : field in  $a$ - $c$  plane). The effect of cell parameters on the location of  $\Delta\phi^{\max}$  is considered a function of frequency in Figs. 8 and 9.  $\alpha$  and  $\beta$  of the  $\Delta\phi^{\max}$  membrane points were calculated by equation (6). For the iteration of one parameter ( $\sigma_e$ ,  $\sigma_i$ ,  $g_m$  or  $C_m$ ), all other parameters were kept at their standard values (Table 1). As expected, the angles robustly approaches the geometry-determined limiting angles of  $7.2^\circ$  ( $a$ - $c$  plane, Fig. 8) and  $23.78^\circ$  ( $a$ - $b$  plane, Fig. 9) at low frequencies for a low membrane conductance.

Generally, three frequency plateaus are obtained for the angles. The first and second plateaus occur at frequencies from  $0$ - $10^4$  Hz and  $10^5$ - $10^7$  Hz, respectively. While deviations of the first plateau from the geometry-determined limiting angle depend on membrane conductance, especially at low external conductivities, the third (permittivity) plateau is largely independent from the cell parameter variations considered. Only membrane permittivity variations have a slight effect (Figs. 8D and 9D). In contrast, the second plateaus of  $\alpha$  and  $\beta$  are strongly affected by the cell parameters. It is interesting, that  $\alpha$  and  $\beta$  may increase as well as decrease compared to the geometry-determined limiting angle. The reason is that the polarizability balance along the two semiaxes in the field plane may be deflected either to the shorter or the longer semiaxis, i.e. the shorter or the longer semiaxis may be higher polarizable [49]. The plateau levels of  $\alpha$  and  $\beta$  are independent of  $C_m$  variations. Nevertheless, higher  $C_m$  values shift the transition frequency from the first to the second plateaus toward lower frequencies (Figs. 8D and 9D). Please note that the assumption of cell properties varying along the three axis, e.g. of different cytoplasmic permittivities, results in a more complex behavior of the angle of  $\Delta\phi^{\max}$ . Additional transitions and frequency plateaus are obtained for such assumptions



(data not shown). Nevertheless, such a situation is realistic for biological cells with non-confocal membranes [47].

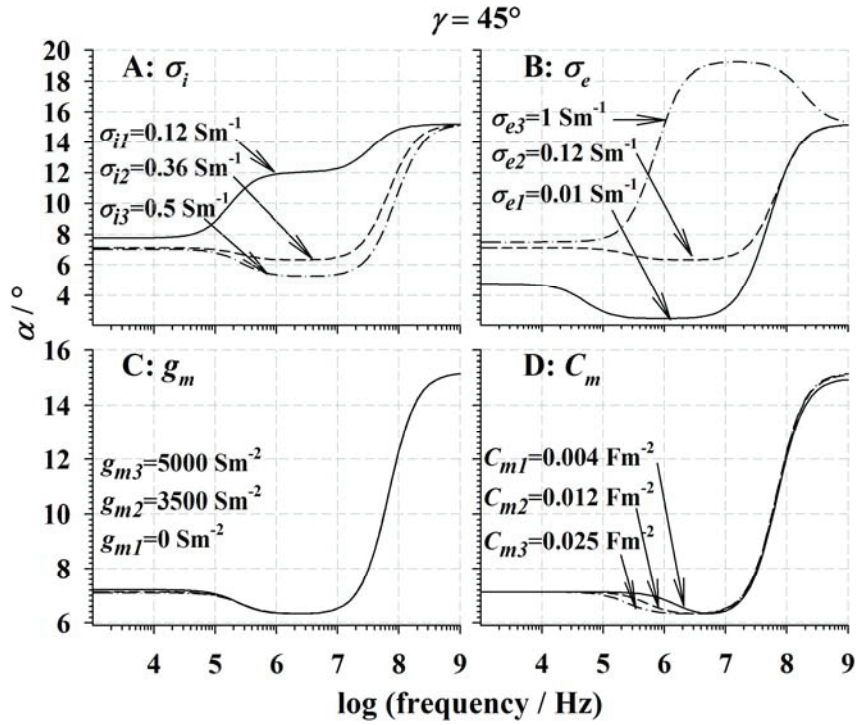


**Fig. 8.** Frequency dependence of the angle  $\alpha$  of the  $\Delta\phi^{\max}$  membrane point on cell parameters for a field orientation of  $\gamma = 45^\circ$  in the  $a$ - $c$  plane. (A) internal conductivity,  $\sigma_i$ ; (B) external conductivity,  $\sigma_e$ ; (C) membrane conductance,  $g_m$ ; (D) area specific membrane capacitance,  $C_m$ .

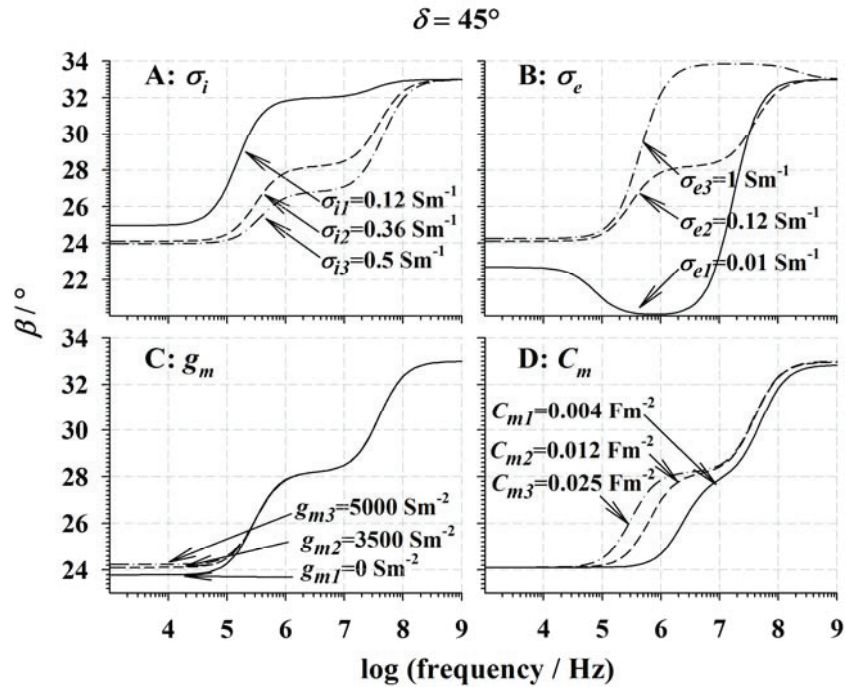


**Fig. 9.** Frequency dependence of the angle  $\beta$  of the  $\Delta\phi^{\max}$  membrane point on cell parameters for a field orientation of  $\delta = 45^\circ$  in the  $a$ - $b$  plane. (A) internal conductivity,  $\sigma_i$ ; (B) external conductivity,  $\sigma_e$ ; (C) membrane conductance,  $g_m$ ; (D) area specific membrane capacitance,  $C_m$ .

The  $\Delta\phi$  balance along the three semiaxes is plotted in Fig. 10 to consider the physical background of the angle transitions in Figs. 8 and 9. Fig. 10A shows that the frequency dependence of  $\Delta\phi$  is qualitatively very similar along the three semiaxis. At low frequency ( $<10^5$  Hz) the amplitude of  $\Delta\phi$  is frequency independent. The amplitude of  $\Delta\phi$  is highest for the longest semiaxis ( $\Delta\phi_a > \Delta\phi_b > \Delta\phi_c$ , Fig. 10A). Transitions of the relative values occur at frequencies above 100 kHz (Fig. 10A). Above 100 MHz the sequence of the magnitudes even reverses ( $\Delta\phi_c > \Delta\phi_b > \Delta\phi_a$ ; Fig. 10A insert, Fig. 10B). The transitions in the relative magnitudes are identical to the transitions of  $\alpha$  (compare dashed lines in Fig. 10B to dashed line in Fig. 8) and  $\beta$  (compare dotted lines in Fig. 10B to dashed line in Fig. 9).

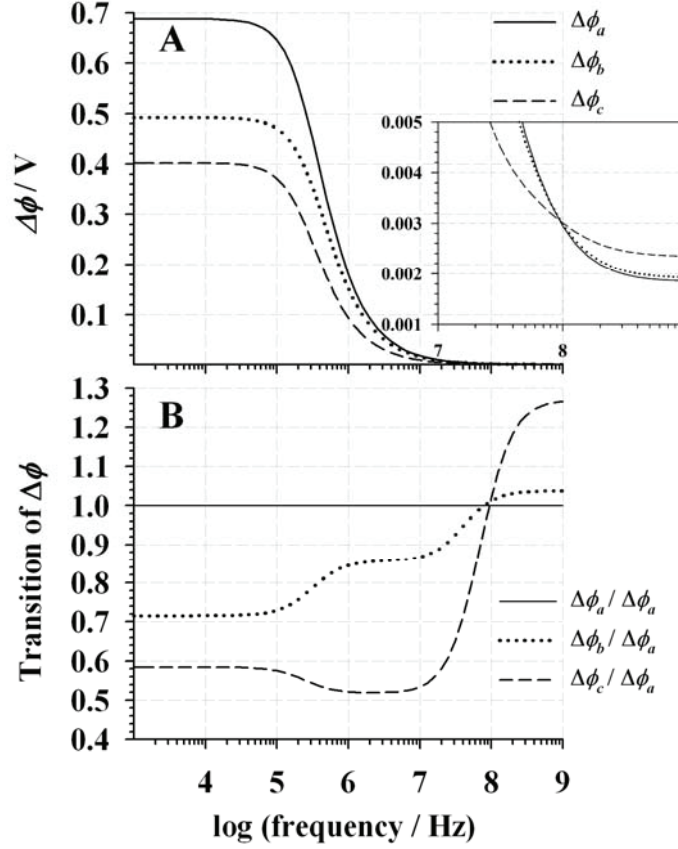


**Fig. 10.** Frequency dependence of the absolute values of  $\Delta\phi$  according to the full model (equation (2), Table 1). (A) frequency dependence of  $\Delta\phi$  at the poles for a field orientation along the of semi-axes  $a$ ,  $b$  and  $c$ , respectively. Insert: curves cross one another at around 100 MHz. (B) amplitudes of  $\Delta\phi$  at the poles relative to  $\Delta\phi_a$ . Please compare to the transitions of  $\alpha_{(\Delta\phi^{\max})}$  and  $\beta_{(\Delta\phi^{\max})}$  in Figs. 8 and 9, respectively.

#### 4.1.4. Electric field distribution in the EP chamber

We used COMSOL 3.3A Multiphysics program (Comsol AB, Stockholm, Sweden) to consider the three-dimensional electric field distribution in the inter-electrode space of the chip chamber (Fig. 11). Driving potentials of +/-10 V were assumed for example at a length of 50  $\mu\text{m}$  ( $y$ -direction in Fig. 11). The parallel electrodes **E1** and **E2** had a distance

of  $80\ \mu\text{m}$  (Fig. 4,  $x$ -direction in Fig. 11) and a height of  $100\ \text{nm}$ , determined by the thickness of the platinum layer ( $z$ -direction in Fig. 11). Aqueous solution was assumed to cover both electrodes by  $5\ \mu\text{m}$ , the approximate filling height in the EP experiments. The arrowheads and arrow lengths present the directions and magnitudes of the electric field, respectively. Inhomogeneous fields were found at the electrode edges.

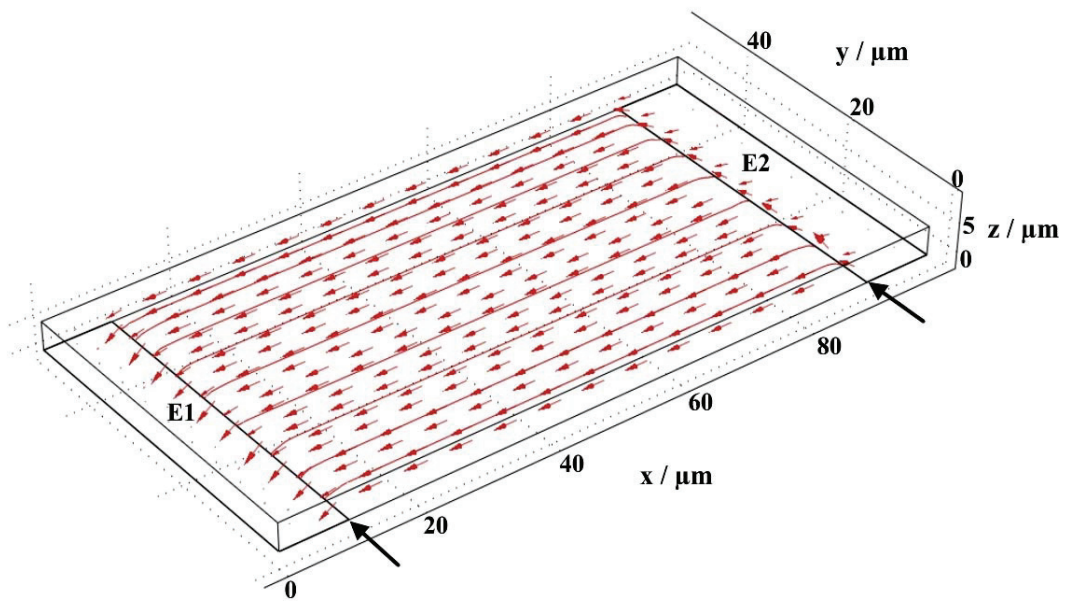


**Fig. 11.** Three-dimensional electric field distributions in the EP chamber in between the two plane-parallel electrodes E1 and E2. The electrode distance is  $80\ \mu\text{m}$ . The width, length and thickness of each electrode are  $10\ \mu\text{m}$ ,  $50\ \mu\text{m}$  and  $100\ \text{nm}$ , respectively.  $5\ \mu\text{m}$  filling height were assumed for the aqueous measuring solution.

Figure 12 presents the electric field strength in  $x$ -direction at different heights along lines in the center of the model ( $y = 25\ \mu\text{m}$ ). The constant center field strength is altered at distances of the electrodes lower than  $10\ \mu\text{m}$ . While the field strength is increased along lines close to the chamber bottom ( $z < 1\ \mu\text{m}$ ) it is decreased for higher lines ( $z = 3\ \mu\text{m}$  and  $z = 5\ \mu\text{m}$ ). Please note that the discontinuity of the  $1\ \mu\text{m}$  line is generated by meshing problems due to the limited resources of the computer.

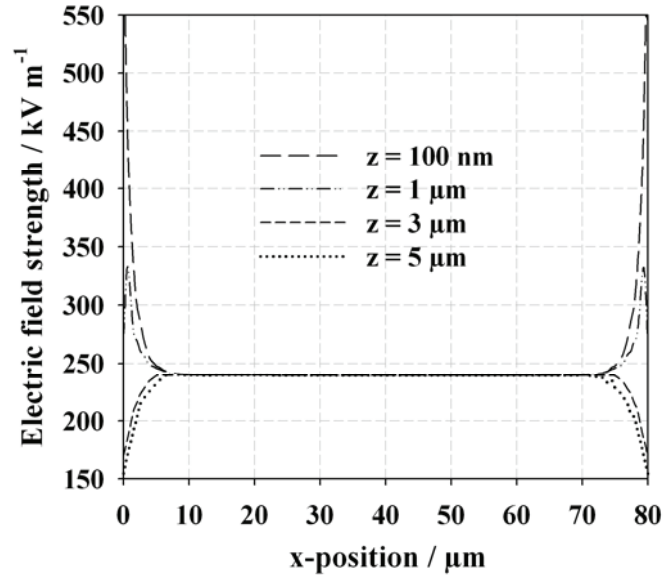


**Fig. 12.** Electric field strengths along lines in  $x$ -direction at different heights  $z$ .

## 4.2. EP results

### 4.2.1. Dependence of PI permeabilization and cell lysis of oriented CRBCs on electric field strength, frequency and pulse duration

CRBCs are nucleated and have a three-axial ellipsoidal shape. The nuclei are clearly visible (Figs. 5 and 13). The semiaxes measures obtained from 60 cells were  $a : b : c = 6.66 \pm 0.19 \mu\text{m} : 4.17 \pm 0.26 \mu\text{m} : 1.43 \pm 0.08 \mu\text{m}$ . Experimental considerations were restricted to the case of semiaxis  $c$  being perpendicularly oriented to the external field  $E$  ( $\gamma = \alpha = 0^\circ$ ; see also Fig. 3B). Fig. 13 presents examples of phase-contrast and fluorescence micrographs of CRBCs immediately and 3 min after the pulse. Three angle-classes of cell orientation were considered as indicated in Fig. 13 ( $\delta = 0^\circ, 45^\circ$  and  $90^\circ$ ).

The pulse duration was kept constant at 10 ms to consider the frequency dependence of EP. Examples are shown in Figs. 13A - D. Cells of all orientations were permeabilized for PI at 1 kHz (Figs. 13A and B). Only cells oriented parallel to the field

(cells 1 and 2) were permeabilized for PI at 150 kHz, while cells oriented at 45° and 90° (cells 5 and 6) were not permeabilized (Figs. 13C and D). Detailed results on the frequency dependence are given in Fig. 14.

The frequency was kept constant at 1 kHz to consider the pulse duration dependence. Examples are shown in Figs. 13E – H. Four out of six cells were permeabilized for PI at 1 ms (Figs. 13E and F). All cells were permeabilized for PI by the longer 100 ms pulse. Two cells even lysed (cells 3 and 4 in Figs. 13G and H). Lysed cells lost their hemoglobin content after pulse application, their nuclei swelled. An example is cell number 6 in Fig. 13E. For its location close to the electrode it is the only lysed cell, even though it is oriented at 72° (see also Figs. 11 and 12). Detailed results of the pulse duration dependence are given in Fig. 15.

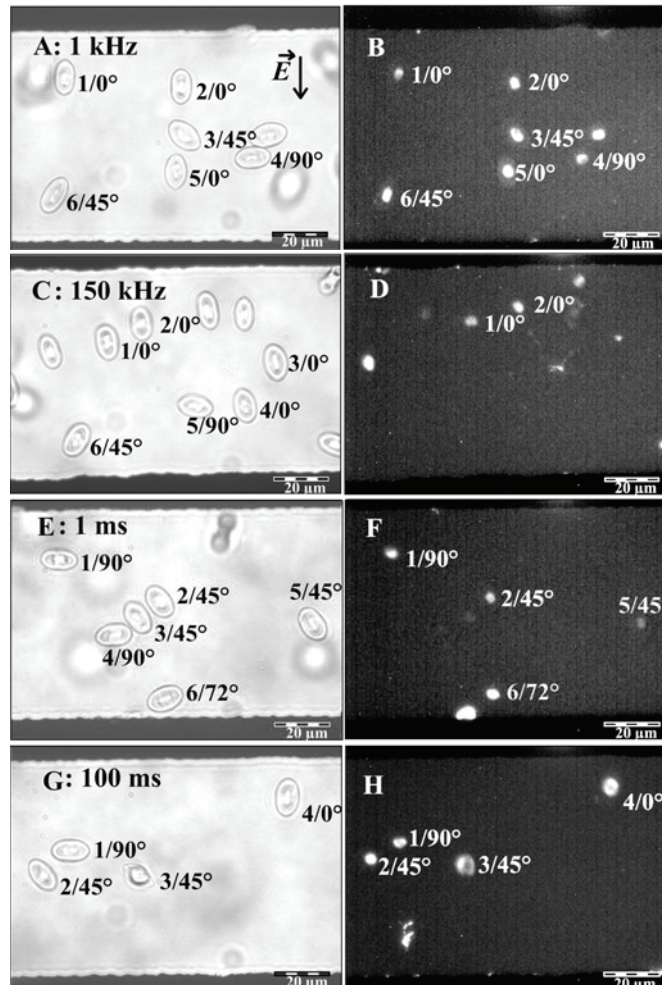


**Fig. 13.** EP of oriented CRBCs suspended in 10  $\mu\text{M}$  PI solution ( $\sigma_e = 0.12 \text{ Sm}^{-1}$ ). Left column (A, C, E and G): phase contrast micrographs immediately after the pulse. Right column (B, D, F and H): fluorescence micrographs 3 minutes after pulses of  $E = 200 \text{ kVm}^{-1}$  ( $16 V_{pp}$ , electrode distance 80  $\mu\text{m}$ ). Different pulse durations of 1 ms (E), 10 ms (A and C) and 100 ms (G) as well as different field frequencies of 1 kHz (A, E and G) and 150 kHz (C) were used. Cell numbers and the orientation angles of their semiaxes  $a$  with respect to the field are indicated. PI permeabilized (small fluorescent spots, normal nucleus size) and lyzed (E: number 6, G: numbers 3 and 4, swelled nuclei) cells were distinguished from the appearance of their nuclei.

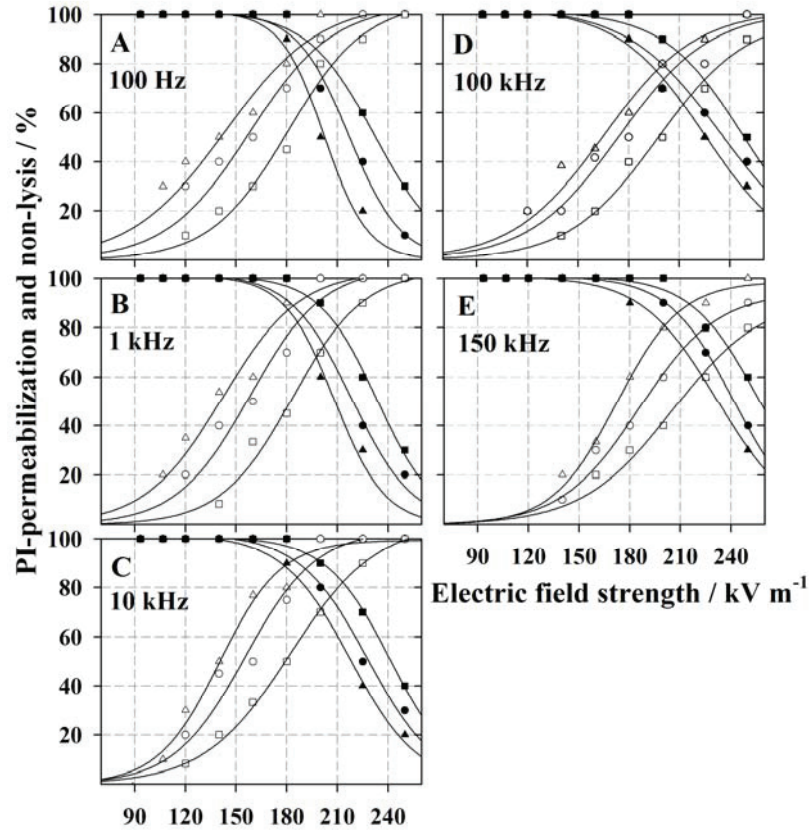
The percentages of PI permeabilized and non-lysed cells were plotted over field strength for different pulse durations and field frequencies to analyze the electroporation properties of CRBCs. Sigmoidal curves were fitted to the experimental data (Figs. 14 and 15):

$$y = \frac{a}{1 + \exp((E_{50\%} - E)/b)} \quad (21)$$

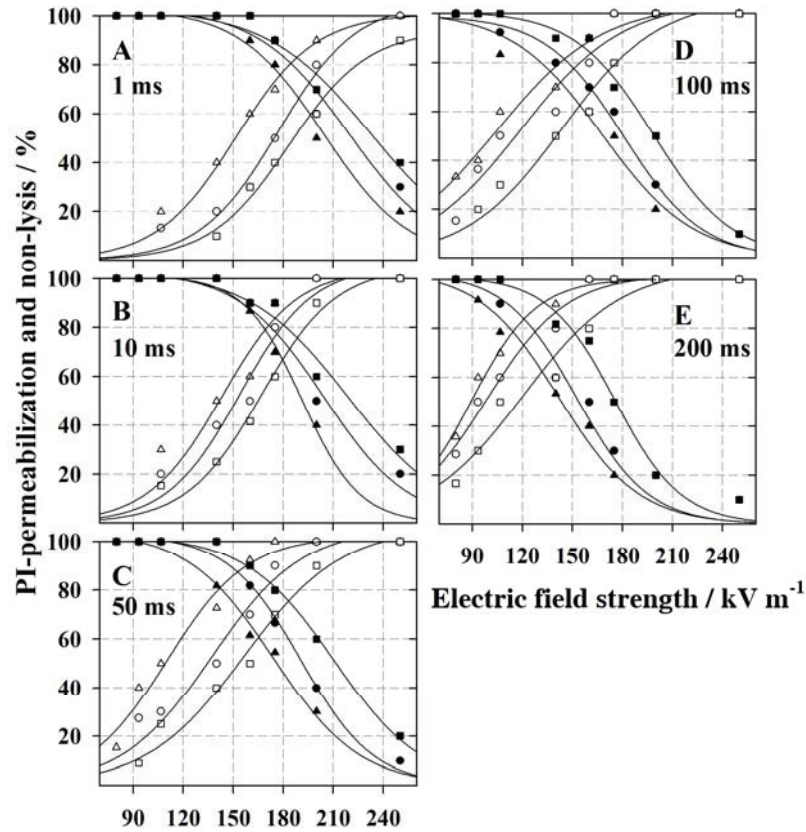
Where  $y$ ,  $a$ , and  $b$  denote the percentages of cells complying with one of the two criteria (PI permeabilization or non-lysis), the final ( $b$  negative) or starting ( $b$  positive) percentage of cells for zero-field strength and the slope of the sigmoidal curve.  $E$  is the electric field strength of a data point and  $E_{50\%}$  determines the electric field strength corresponding to the 50% criterion [13,50]. All curves were fitted using a nonlinear least-square regression program (SigmaPlot 9.5). Figs. 14 and 15 show results of the frequency, pulse length, field strength and orientation dependencies for the two criteria [11-15,17]. Figure 14 presents the frequency dependence for a constant pulse duration of 10 ms. The figure shows a higher EP efficiency at lower frequencies (compare to Gimsa and Wachner [29]).

Fig. 15 presents the effect of pulse duration for a constant frequency of 1 kHz. This frequency is low enough to be still in the plateau range of the DC-limit (Figs. 10 and 17) and high enough to avoid electrode effects. Higher field strengths are required for an effective EP at shorter pulse durations and higher numbers of lysed cells are found at longer pulse durations [14,15]. Clearly, EP efficiency is higher at a cell orientation of  $\delta = 0^\circ$  than at  $\delta = 45^\circ$  and  $90^\circ$  [23].





**Fig. 14.** Field strength dependence of PI permeabilization and survival (non-lysis) of CRBCs for different field frequencies at  $\sigma_e = 0.12 \text{ S m}^{-1}$ . Pulse duration was 10 ms. Cell orientations of  $\delta = 0^\circ$  (triangle),  $45^\circ$  (circle), and  $90^\circ$  (square) were considered. Hollow and filled symbols indicate the percentages of PI permeabilization and non-lysis, respectively. Sigmoidal curves (equation (21)) were fitted to the measuring points.



**Fig. 15.** Field strength dependence of PI permeabilization and non-lysis of CRBCs for different pulse durations at  $\sigma_e = 0.12 \text{ S m}^{-1}$ . Field frequency was 1 kHz. Cell orientations of  $\delta = 0^\circ$  (triangle),  $45^\circ$  (circle), and  $90^\circ$  (square) were considered. Hollow and filled symbols indicate the percentages of PI permeabilization and non-lysis, respectively. Sigmoidal curves were fitted (equation (21)) to the measuring points.

#### 4.2.2. Critical field strength for oriented cells in dependence of field frequency and pulse duration

We defined critical field strengths  $E_{crit}$  for PI permeabilization and cell lysis from the 50%-values of the fitted curves in Figs. 14 and 15, i.e. 50% of the cells comply with one of the criteria at  $E_{crit}$  [1]. The  $E_{crit}$  for PI permeabilization was always lower than for cell lysis independent of cell orientation.

Figure 16 presents the frequency and pulse duration dependence of the two  $E_{crit}$  parameters. The parameters increase for higher frequencies (Fig. 16A) and shorter pulses (Fig. 16B). Below 100 kHz the  $E_{crit}$  for PI permeabilization was independent of frequency, whereas it is increasing at higher frequencies [22]. This behavior is in accordance with equations 4 and 5. Nevertheless,  $E_{crit}$  for cell non-lysis increases linearly with frequency also below 100 kHz (Fig. 16A). The reason may be that the nonlinear processes related to the formation of large aqueous pores, membrane rupture, and cell lysis are much stronger than those resulting in PI permeabilization [7-9]. Further, the different relative  $E_{crit}$  values (Table 3) for PI permeabilization and cell non-lysis at the different angles of cell orientation are most probably resulting from these properties. Therefore, our model cannot describe the frequency dependence involved. For these reasons, no  $\Delta\phi_{crit}$  values were derived from the cell lysis data.

A field frequency of 10 kHz was chosen to search for the optimal pulse duration. This frequency is high enough to exclude electrode processes and at the same time still below the membrane dispersion. Averaging over all cell orientations led to mean values of  $E_{crit}$  for the two parameters PI permeabilization and cell lysis in dependence on frequency (dashed lines in Fig. 16B). The criterion for the optimal pulse duration was high PI permeabilization at low cell lysis. The distances between the average lines are frequency dependent, suggesting an optimal differentiation of the two criteria at a pulse duration of 10 ms (dotted vertical line in Fig. 16B). The field oscillates 100 times at this relatively short pulse duration.

$\Delta\phi_{crit}$  values could be obtained from  $E_{crit}$  by fitting the respective summands of equation (4) using the parameters of Table 1 (Fig. 17; see also Marszalek et al. [22]). Field orientations of  $\delta=0^\circ$  (first summand of equation (4) for  $d_x=a$ ),  $45^\circ$ , and  $90^\circ$  (second summand of equation (4),  $d_y=b$ ) were considered. While the angles of  $\Delta\phi^{max}$  are frequency independent for  $\delta=0^\circ$  and  $90^\circ$  ( $\beta$  equal to  $\delta$ ),  $\Delta\phi^{max}$  shows a complex behavior for  $\delta=45^\circ$  (Fig. 9). Nevertheless, this complex behavior appears beyond our experimental frequency range (Fig. 17). For this reason, we used the geometry determined limiting angle (compare to equation 11) to calculate  $\Delta\phi_{crit}$  from the determined  $E_{crit}$  values (figure

16A). For simplification, we neglected the membrane conductance. The obtained  $\Delta\phi_{crit}$  values for PI permeabilization are given in Table 3. Theoretical  $\Delta\phi_{crit}$  values were only calculated for PI permeabilization for the reasons discussed above.

Please note that Fig. 17 refers to PI permeabilization only. Other probe molecules may yield different values. Nevertheless, the low deviation of the curves from the data points indicates that the cell parameters of Table 1 are reasonable assumptions for CRBCs.

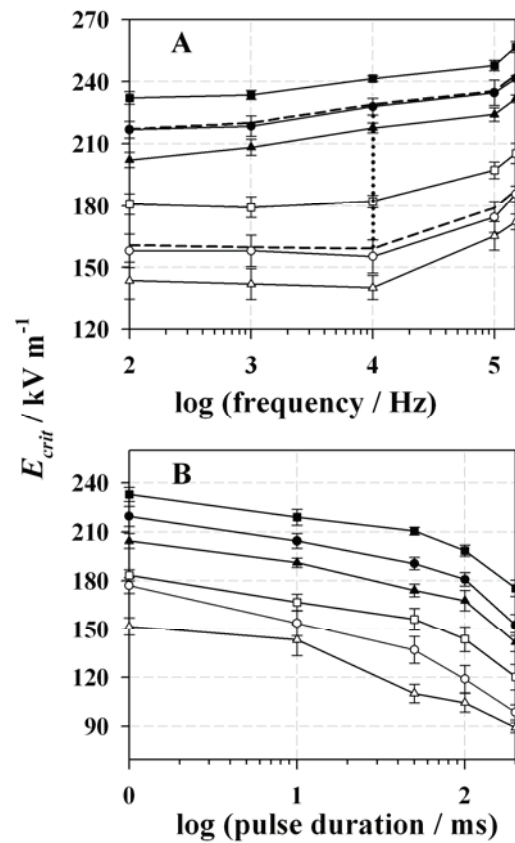


**Fig. 16.** Comparison of  $E_{crit}$  for PI permeabilization and non-lysis for various field frequencies (A, pulse duration 10 ms) and pulse durations (B, field frequency 1 kHz). Three cell orientations are considered. Dashed lines in (B) denote the average of the orientations for the two  $E_{crit}$  criteria. The dotted vertical line marks the optimal frequency for differentiation of PI permeabilization and non-lysis.

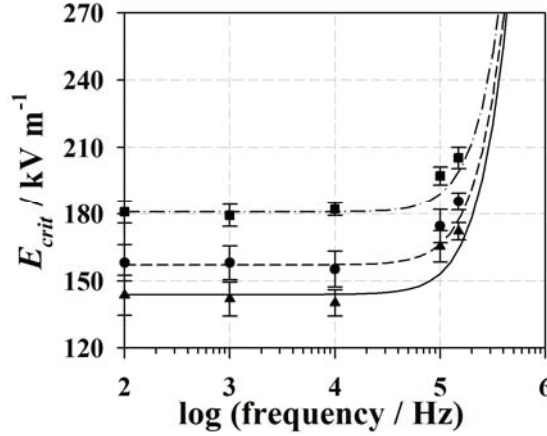


**Fig. 17.** Fitted frequency dependence of  $E_{crit}$  of PI permeabilization for three cell orientations over frequency (data of Fig. 16B). Equations (4) and (5) and the parameters of Table 1 were used. The fits yielded the  $\Delta\phi_{crit}$ -values of Table 3.

**Table 3** Comparison of critical field strengths ( $E_{crit}$ ) and critical  $\Delta\phi$  ( $\Delta\phi_{crit}$ ) for PI permeabilization for different orientations of semiaxis  $a$  with respect to the field. Please note that  $E_{crit}$  for PI permeabilization for a field rotating in the  $a$ - $b$  plane was approx. 115  $\text{kV m}^{-1}$  corresponding to a  $\Delta\phi_{crit}$  of 0.79 V.

Parameter	Cell orientations		
	0°	45°	90°
$E_{crit}/\text{kVm}^{-1}$ (PI permeabilization, 1 kHz, 10 ms)	141.89±7.53	158.07±7.59	179.34±4.88
$E_{crit}$ relative to $E_{crit}$ at 0°	1	1.11	1.26
$E_{crit}/\text{kVm}^{-1}$ (non-lysed cells, 1 kHz, 10 ms)	208.29±3.93	218.59±4.89	233.59±2.16
$E_{crit}$ relative to $E_{crit}$ at 0°	1	1.05	1.12
$\Delta\phi_{crit}/\text{V}$ (theoretical analysis of data in Fig. 17)	0.99	0.94	0.89
$\Delta\phi_{crit}$ relative to $\Delta\phi_{crit}$ at 0°	1	0.95	0.89

The assumption of a specific membrane capacitance even higher than  $0.025 \text{ Fm}^{-2}$  (Table 1) would probably result in a theoretical  $E_{crit}$  increase already at lower frequencies and improved fits at higher frequencies.

Our results confirm that the membrane sensitivity toward the field depends on membrane curvature. Three factors may be important for this effect: i) the larger the area oriented perpendicularly to the field (low curvature) the larger the area experiencing a high  $\Delta\phi$  and the higher the probability of pore formation. As a result the membrane sensitivity for the induced  $\Delta\phi$  will be higher along the two shorter semiaxes; ii) the surface tension generates forces attracting membrane molecules from other membrane areas. These forces are stronger in areas of higher curvature around the poles of the longer axis, i.e. when molecules are becoming available by the growth of pores they are faster collected in areas of high curvature leading to a facilitated pore growth in areas of low curvature. Nevertheless, such a global effect may require a membrane property that provides argument iii): areas of higher curvature may be stabilized by molecular structures near the poles of the longer semiaxis. As a result, the membrane will be less sensitive toward field induced distortions in these areas. In practice, a combination of the above and unknown effects may explain our findings. Please also note, that the actual curvatures in CRBCs are different from those of a general ellipsoid of the same axis-lengths (Fig. 5).

## 5. Conclusions

We developed a model for the  $\Delta\phi$  induced in three-axial ellipsoidal and spheroidal cells with an arbitrary orientation within the field in order to analyze the effects of cell orientation, field strength and frequency. The model was tested in EP experiments on ellipsoidal CRBCs of different orientations in a glass chip chamber with interdigitated electrodes. The chamber design allowed for the generation of different field strengths from a single driving pulse. The chamber provided homogeneous fields in large areas between the electrodes. The permeabilization and lysis rates were only increased for cells sedimented in the immediate vicinity of the electrodes due to the strongly inhomogeneous

fields at these sites. Integrated temperature sensors allowed us to prove that the EP pulse did not induce a strong temperature increase in the chamber.

The percentages of PI permeabilized and lysed cells increased with pulse duration and decreased with field frequency. The optimal pulse duration and field frequency, i.e. a high percentage of PI permeabilization at a low lysis rate, were approx. 10 ms and 10 kHz for CRBCs at an external conductivity of  $0.12 \text{ S m}^{-1}$ . Theoretical analysis showed that  $\Delta\phi$  is highest when the longest semiaxis is oriented in parallel to the field. This is expressed in the lowest  $E_{crit}$  values for PI permeabilization ( $142 \text{ kV m}^{-1}$ ) and cell lysis ( $208 \text{ kV m}^{-1}$ ) at this orientation. Nevertheless, model analysis revealed that  $\Delta\phi_{crit}$  for PI permeabilization was different along the  $a$ - ( $\delta = 0^\circ$ ,  $0.99 \text{ V}$ ) and  $c$ - axes ( $\delta = 90^\circ$ ,  $0.89 \text{ V}$ ) and for the intermediate orientation ( $\delta = 45^\circ$ ,  $0.94 \text{ V}$ ) [22]. Possible reasons for this higher field sensitivity of membrane areas with lower curvature are discussed. Comparison of the lowest  $E_{crit}$  for PI staining in a linear field ( $142 \text{ kV m}^{-1}$ ) and a field rotating in the  $a$ - $b$  plane ( $115 \text{ kV m}^{-1}$ ) revealed the higher EP efficiency of rotating fields.

Theoretically, the location of the  $\Delta\phi^{max}$  membrane point in DC or low frequency fields depends on cell parameters in the event that the field is not oriented parallel to one of the axes. Its location changes with frequency in the dispersion ranges of cell polarization.

### **Acknowledgements**

KM is grateful for a stipend from the Royal Thai government. This study has partly been supported by grant StSch 20020418A of the Bundesamt für Strahlenschutz to JG. The authors are grateful to the International Postgraduate Program (IPP) supported by DAAD, BMBF and DFG. We would like to thank C. Tautorat and Dr. W. Kröger for their help with the chip carriers, as well as M. Stubbe for help with the COMSOL Multiphysics program. J. Donath is acknowledged for technical assistance and R. Sleight for help with the manuscript. We also thank Prof. Dr. L. Jonas from the Electron Microscopy Centre of the Medical Faculty, University of Rostock for the SEM micrographs.

## Appendix

### *Simplified equations of the influential radius for spheroidal cells*

The plot of the relative influential radius  $a_{\text{infl}}/a$  compared to the logarithm of the axis ratio exhibits a sigmoidal shape for spheroids (see Maswivat et al. [46] for more details). This behavior can be approximated by:

$$\frac{a_{\text{infl}}}{a} = \frac{a+2c}{a+c} = 2 - \frac{1}{1+(c/a)} \quad (\text{A1})$$

The limiting values for infinitely thin disks, spheres and infinitely long cylinders 1, 1.5, and 2 are correctly reflected by equation (A1). Since the sum of the depolarizing factors ( $n_a + n_b + n_c$ ) along the three principal axes of a general ellipsoid is always unity [51,52] it follows that  $a/a_{\text{infl}}+b/b_{\text{infl}}+c/c_{\text{infl}}=2$  [49] and for the relative influential radius  $c_{\text{infl}}/c$  along the symmetry axis  $c$ :

$$\frac{c_{\text{infl}}}{c} = \frac{a+2c}{2c} = 1 + \frac{1}{2(c/a)} \quad (\text{A2})$$

## References

- [1] E. Neumann, A. Sprafke, E. Boldt, H. Wolf, Biophysical considerations of membrane electroporation, in: D.C. Chang, B.M Chassy, J.A. Saunders, A.E. Sowers (Eds.), Guide to electroporation and electrofusion, Academic Press, San Diego, 1992, pp. 77-90.
- [2] K.Jr. Kinosita, T.Y. Tsong, Voltage-induced pore formation and hemolysis of human erythrocytes, *Biochimica et Biophysica Acta* 471 (1977) 227-242.
- [3] A.J.H. Sale, W.A. Hamilton, Effects of high electric fields on microorganisms III. Lysis of erythrocytes and protoplasts *Biochim. Biophys. Acta* 163 (1968) 37-43.



- 
- [4] U. Zimmermann, The effect of high intensity electric field pulses on eukaryotic cell membranes: Fundamentals and applications, in: U. Zimmermann, G. A. Neil (Eds.), *Electromanipulation of Cells*, CRC, Boca Raton, FL, 1996, pp. 1-106.
- [5] J. Teissie, M.P. Rols, An experimental evaluation of the critical potential difference inducing cell membrane electropermeabilization, *Biophys. J.* 65 (1993) 409-413.
- [6] U. Zimmermann, R. Benz, Dependence of the electrical breakdown voltage on the charging time in *Valonia utricularis*, *Membrane Biol.* 53 (1980) 33-43.
- [7] R.W. Glaser, S.L. Leikin, L.V. Chernomordik, V.F. Pastushenko, A.I. Sokirko, Reversible electrical breakdown of lipid bilayers: formation and evolution of pores, *Biochim. Biophys. Acta* 940 (1988) 275-287.
- [8] R.W. Glaser, J. Gimsa, Gradual changes of membrane properties at high transmembrane electric potential simulate a breakdown threshold, in: M. Blank (Ed.), *Electricity and magnetism in biology and medicine*, San Francisco Press, Inc., San Francisco, 1993, pp. 135-137.
- [9] L.V. Chernomordik, S.I. Sukharev, S.V. Popov, V.F. Pastushenko, A.V. Sokirko, I.G. Abidor, Y.A. Chizmadzhev, The electrical breakdown of cell and lipid membranes: the similarity of phenomenologies, *Biochimica et Biophysica Acta* 902 (1987) 360-373.
- [10] R. Benz, U. Zimmermann, High electric field effects on the cell membranes of *Halicystis parvula*: A charge pulse study, *Planta* 152 (1981) 314-318.
- [11] A.M. Lebar, D. Miklavcic, Cell electropermeabilization to small molecules *in vitro*: control by pulse parameters, *Radiol. Oncol.* 35 (2001) 193-202.
- [12] K.J. Müller, V.L. Sukhorukov, U. Zimmermann, Reversible electropermeabilization of mammalian cells by high-intensity, ultra-short pulses of submicrosecond duration, *J. Membrane Biol.* 184 (2001) 161-170.
- [13] M. Puc, T. Kotnik, L.M. Mir, D. Miklavcic, Quantitative model of small molecules uptake after *in vitro* cell electropermeabilization, *Bioelectrochemistry* 60 (2003) 1-10.

- 
- [14] M.P. Rols, J. Teissie, Electropermeabilization of mammalian cells: Quantitative analysis of the phenomenon, *Biophys. J.* 58 (1990) 1089-1098.
- [15] M.P. Rols, J. Teissie, Electropermeabilization of mammalian cells to macromolecules: Control by pulse duration, *Biophys. J.* 75 (1998) 1415-1423.
- [16] J. Teissie, C. Ramos, Correlation between electric field pulse induced long-lived permeabilization and fusogenicity in cell membranes, *Biophys. J.* 74 (1998) 1889-1898.
- [17] H. Wolf, M.P. Rols, E. Boldt, E. Neumann, J. Teissie, Control by pulse parameters of electric field-mediated gene transfer in mammalian cells, *Biophys. J.* 66 (1994) 524-531.
- [18] D. Fologea, T.V. Dimov, I. Stoica, O. Csutak, M. Radu, Increase of *Saccharomyces cerevisiae* plating efficiency after treatment with bipolar electric pulses, *Bioelectrochem. Bioener.* 46 (1998) 285-287.
- [19] T. Kotnik, L.M. Mir, K. Flisar, M. Puc, D. Miklavcic, Cell membrane electropermeabilization by symmetrical bipolar rectangular pulses: Part I. Increased efficiency of permeabilization, *Bioelectrochemistry* 54 (2001) 83-90.
- [20] T. Kotnik, G. Pucihar, M. Rebersek, D. Miklavcic, L.M. Mir, Role of pulse shape in cell membrane electropermeabilization, *Biochim. Biophys. Acta* 1614 (2003) 193-200.
- [21] H.G.L. Coster, U. Zimmermann, The mechanism of electrical breakdown in the membranes of *Valonia utricularis*, *J. Membrane Biol.* 22 (1975) 73-90.
- [22] P. Marszalek, D.S. Liu, T.Y. Tsong, Schwan equation and transmembrane potential induced by alternating electric field, *Biophys. J.* 58 (1990) 1053-1058.
- [23] B. Valic, M. Golzio, M. Pavlin, A. Schatz, C. Faurie, B. Gabriel, J. Teissie, M.P. Rols, D. Miklavcic, Effect of electric field induced transmembrane potential on spheroidal cells: theory and experiment, *Eur. Biophys. J.* 32 (2003) 519-528.
- [24] H. Fricke, The electric permittivity of a dilute suspension of membrane-covered ellipsoids, *J. Appl. Phys.* 24 (1953) 644-646.

- 
- [25] J. Gimsa, D. Wachner, On the analytical description of transmembrane voltage induced on spheroidal cells with zero membrane conductance, *Eur. Biophys. J.* 30 (2001) 463-466.
- [26] D.C. Chang, J.R. Hunt, Q. Zheng, P.Q. Gao, Electroporation and electrofusion using a pulsed radio-frequency electric field, in: D.C. Chang, B.M. Chassy, J.A. Saunders, A.E. Sowers (Eds.), *Guide to electroporation and electrofusion*, Academic Press, San Diego, 1992, pp. 303-326.
- [27] J. Bernhardt, H. Pauly, On the generation of potential differences across the membranes of ellipsoidal cells in an alternating electrical field, *Biophysik* 10 (1973) 89-98.
- [28] G. Fuhr, R. Hagedorn, R. Glaser, J. Gimsa, T. Müller, Membrane potentials induced by external rotating electrical fields, *J. Bioelectricity* 6 (1987) 49-69.
- [29] J. Gimsa, D. Wachner, A unified resistor-capacitor model for impedance, dielectrophoresis, electrorotation, and induced transmembrane potential, *Biophys. J.* 75 (1998) 1107-1116.
- [30] J. Gimsa, D. Wachner, Analytical description of the transmembrane voltage induced on arbitrarily oriented ellipsoidal and cylindrical cells, *Biophys. J.* 81 (2001) 1888-1896.
- [31] C. Grosse, H.P. Schwan, Cellular membrane potentials induced by alternating fields, *Biophys. J.* 63 (1992) 1632-1642.
- [32] E. Neumann, The relaxation hysteresis of membrane electroporation, in: E. Neumann, A.E. Sowers, C.A. Jordan (Eds.), *Electroporation and electrofusion in cell biology*, Plenum Press, New York, 1989, pp. 61-82.
- [33] H.P. Schwan, Biophysics of the interaction of electromagnetic energy with cells and membranes, in: M. Grandolfo, S.M. Michaelson, A. Rindi (Eds.), *Biological effects and dosimetry of nonionizing radiation*, Plenum Press, New York, 1983, pp. 213-231.

- 
- [34] T.Y. Tsong, Electroporation of cell membranes: Mechanism and applications, in: E. Neumann, A.E. Sowers, .C.A. Jordan (Eds.), *Electroporation and electrofusion in cell biology*, Plenum Press, New York, 1989, pp. 149-163.
- [35] J. Gimsa, E. Donath, R. Glaser, Evaluation of the data of simple cells by electrorotation using square-topped fields, *Bioelectrochem. Bioener.* 19 (1988) 389-396.
- [36] J. Gimsa, P. Marszalek, U. Loewe, T.Y. Tsong, Electroporation in rotating electric fields, *Bioelectrochem. Bioenerg.* 29 (1992) 81-89.
- [37] Y. Huang, B. Rubinsky, Micro-electroporation: Improving the efficiency and understanding of electrical permeabilization of cells, *Biomed. Microdevices* 2 (1999) 145-150.
- [38] Y. Huang, B. Rubinsky, Microfabricated electroporation chip for single cell membrane permeabilization, *Sensors and Actuators A* 89 (2001) 242-249.
- [39] Y. Huang, B. Rubinsky, Flow-through micro-electroporation chip for high efficiency single-cell genetic manipulation, *Sensors and Actuators A* 104 (2003) 205-212.
- [40] Y.C. Lin, M.Y. Huang, Electroporation microchips for *in vitro* gene transfection, *J. Micromech. Microeng.* 11 (2001) 542-547.
- [41] Y.C. Lin, M. Li, C.S. Fan, L.W. Wu, A microchip for electroporation of primary endothelial cells, *Sensors and Actuators A* 108 (2003) 12-19.
- [42] Y.C. Lin, M. Li, C.C. Wu, Simulation and experimental demonstration of the electric field assisted electroporation microchip for *in vitro* gene delivery enhancement, *Lab Chip* 4 (2004) 104-108.
- [43] J.A. Kim, K. Cho, Y.S. Shin, N. Jung, C. Chung, J.K. Chang, A multi-channel electroporation microchip for gene transfection in mammalian cells, *Biosensors and Bioelectronics* 22 (2007) 3273-3277.
- [44] H. Lu, M.A. Schmidt, K.F. Jensen, A microfluidic electroporation device for cell lysis *Lab Chip* 5 (2005) 23-29.

- 
- [45] J. Gimsa, D. Wachner, A polarization model overcoming the geometric restrictions of the Laplace's solution for spheroidal cells: Obtaining new equations for field-induced forces and transmembrane potential, *Biophys. J.* 77 (1999) 1316-1326.
- [46] K. Maswiwat, D. Wachner, R. Warnke, J. Gimsa, Simplified equations for the transmembrane potential induced in ellipsoidal cells of rotational symmetry, *J. Phys. D: Appl. Phys.* 40 (2007) 914-923.
- [47] S. Lippert, J. Gimsa, High resolution measurements of dielectric cell properties by a combination of AC-electrokinetic effects, in: P. Kostarakis (Ed.), *Proc. 2<sup>nd</sup> International Workshop on Biological Effects of EMFs*, Rhodes, Greece, 2002, pp. 830-836.
- [48] C.J.G. Yeh, B.L. His, W.P. Faulk, Propidium iodide as a nuclear marker in immunofluorescence. II. Use with cellular identification and viability studies, *J. Immunol. Methods* 43 (1981) 269-275.
- [49] J. Gimsa, A comprehensive approach to electro-orientation, electrodeformation, dielectrophoresis, and electrorotation of ellipsoidal particles and biological cells, *Bioelectrochem.* 54 (2001) 23-31.
- [50] G. Pucihar, T. Kotnik, M. Kanduser, D. Miklavcic, The influence of medium conductivity on electroporation and survival of cells in vitro, *Bioelectrochemistry* 54 (2001) 107-115.
- [51] J.A. Stratton, *Electromagnetic theory*, McGraw-Hill, New York, 1941.
- [52] U. Stille, Der Entmagnetisierungsfaktor und Entelektrisierungsfaktor für Rotationsellipsoide, *Archiv Elektrotechnik* 38 (1944) 91-101 (in German).

---

## Bibliography

- Andersson H and Berg A van den 2003 Microfluidic devices for cellomics: a review. *Sensors and Actuators B* **92** 315-25
- Asencor F J, Santamaria C, Iglesias F J and Dominguez A 1993 Dielectric energy of orientation in dead and living cells of *Schizosaccharomyces pombe*: fitting of experimental results to a theoretical model. *Biophys. J.* **64** 1626-31
- Batzing B L 2002 *Microbiology* (Australia: Thomson Learning, Inc.)
- Benz R and Zimmermann U 1981 High electric field effects on the cell membranes of *Halicystis parvula*: a charge pulse study. *Planta* **152** 314-18
- Benz R, Beckers F and Zimmermann U 1979 Reversible electrical breakdown of lipid bilayer membranes: a charge-pulse relaxation study. *J. Membrane Biol.* **48** 181-204
- Bernhardt J and Pauly H 1973 On the generation of potential differences across the membranes of ellipsoidal cells in an alternating electrical field. *Biophysik* **10** 89-98
- Blanks J C 1989 Morphology of the retina. *Retina* ed T E Ogden and A P Schachat (ST. Louis: The C.V. Mosby company) pp 37-52
- Bryant G and Wolfe J 1987 Electromechanical stresses produced in the plasma membranes of suspended cells by applied electric fields. *J. Memb. Biol.* **96** 129-39
- Canatella P J, Black M M., Bonnicksen D M, McKenna C and Prausnitz M R 2004 Tissue electroporation: Quantification and analysis of heterogeneous transport in multicellular environments. *Biophys. J.* **86** 3260-68

- 
- Chang D C, Chassy B M, Saunders J A and Sowers A E 1992 *Guide to electroporation and electrofusion* (San Diego, California: Academic Press, Inc.)
- Chen W, Han Y, Chen Y and Astumian D 1998 Electric field-induced functional reductions in the K<sup>+</sup> channels mainly resulted from supramembrane potential-mediated electroconformational changes. *Biophys. J.* **75** 196-206
- Chernomordik L V, Sukharev S I, Popov S V, Pastushenko V F, Sokirko A V, Abidor I G and Chizmadzhev Y A 1987 The electrical breakdown of cell and lipid emembranes: the similarity of phenomenologies. *Biochimica et Biophysica Acta* **902** 360-73
- Coster H G L and Zimmermann U 1975 The mechanism of electrical breakdown in the membranes of *Valonia utricularis*. *J. Membrane Biol.* **22** 73-90
- Cui L and Morgan H 2000 Design and fabrication of traveling-wave dielectrophoresis structures. *J. Micromech. Microeng.* **10** 72-79
- Cukjati D, Batiuskaite D, Andre F, Miklavcic D and Mir L M 2007 Real time electroporation control for accurate and safe in vivo non-viral gene therapy. *Bioelectrochemistry* **70** 501-7
- Davalos R V, Mir L M and Rubinsky B 2005 Tissue ablation with irreversible electroporation. *Annals of Biomedical Engineering* **33** 223-31
- DeBruin K A and Krassowska W 1999 Modeling electroporation in a single cell II. effects of ionic concentrations. *Biophys. J.* **77** 1225-33

- 
- Dimaki M and Boggild P 2004 Dielectrophoresis of carbon nanotubes using microelectrodes: a numerical study. *Nanotechnology* **15** 1095–102
- Eynard N, Rodriguez F, Trotard J and Teissie J 1998 Electrooptics studies of *Escherichia coli* electropulsation: orientation, permeabilization, and gene transfer. *Biophys. J.* **75** 2587-96
- Freemann S A, Wang M A and Weaver J C 1994 Theory of electroporation of planar bilayer membranes: predictions of the aqueous area, change in capacitance and pore-pore separation. *Biophys. J.* **67** 42-56
- Fricke H 1953 The electric permittivity of a dilute suspension of membrane-covered ellipsoids. *J. Appl. Phys.* **24** 644-6
- Fologea D, Dimov T V, Stoica I, Csutak O and Radu M 1998 Increase of *Saccharomyces cerevisiae* plating efficiency after treatment with bipolar electric pulses. *Bioelectrochem. Bioener.* **46** 285-7
- Fox M B, Esveld D C, Valero A, Luttge R, Mastwijk H C, Bartels P V, Berg A van Den and Boom R M 2006 Electroporation of cells in microfluidic devices: a review. *Anal Bioanal Chem* **385** 474-85
- Fuhr G, Müller T, Schnelle T, Glasser H, Gimsa J, Hofmann U and Wagner B 1997 Handling and investigation of adherently growing cells and viruses of medical relevance in three-dimensional micro-structures. *Proc., IEEE., Tenth Annual International Workshop on Micro Electro Mechanical Systems* (Nagoya, Japan) pp 344-9



- 
- Fuhr G, Schnelle T and Wagner B 1994 Travelling wave-driven microfabricated electrohydrodynamic pumps for liquids. *J. Micromech. Microeng.* **4** 217-26
- Fuhr G, Arnold W M, Hagedorn R, Müller T, Benecke W, Wagner B and Zimmermann U 1992 Levitation, holding, and rotation of cells within traps made by high-frequency fields. *Biochimica et Biophysica Acta* **1108** 215-23
- Fuhr G, Hagedorn R, Müller T, Benecke W, Wagner B and Gimsa J 1991 Asynchronous traveling-wave induced linear motion of living cells. *Studia Biophysica* **140** 79-102
- Fuhr G, Hagedorn R, Glaser R, Gimsa J and Müller T 1987 Membrane potentials induced by external rotating electrical fields. *J. Bioelectricity* **6** 49-69
- Gabriel B and Teissié J 1999 Time courses of mammalian cell electropermeabilization observed by millisecond imaging of membrane property changes during the pulse. *Biophys. J.* **76** 2158-65
- Gimsa J 2002 Characterization of particles and biological cells by AC electrokinetics. *Interfacial electrokinetics and electrophoresis* ed A V Delgado (New York: Marcel Dekker Inc.) pp 369-400
- Gimsa J 2001 A comprehensive approach to electro-orientation, electrodeformation, dielectrophoresis, and electrorotation of ellipsoidal particles and biological cells. *Bioelectrochemistry* **54** 23-31
- Gimsa J and Wachner D 2001a Analytical description of the transmembrane voltage induced on arbitrarily oriented ellipsoidal and cylindrical cells. *Biophys. J.* **81** 1888-96

- 
- Gimsa J and Wachner D 2001b On the analytical description of transmembrane voltage induced on spheroidal cells with zero membrane conductance. *Eur. Biophys. J.* **30** 463-6
- Gimsa J and Wachner D 1999 A polarization model overcoming the geometric restrictions of the Laplace's solution for spheroidal cells: obtaining new equations for field-induced forces and transmembrane potential. *Biophys. J.* **77** 1316-26
- Gimsa J and Wachner D 1998 A unified resistor-capacitor model for impedance, dielectrophoresis, electrorotation, and induced transmembrane potential. *Biophys. J.* **75** 1107-16
- Gimsa J, Müller T, Schelle T and Fuhr G 1996 Dielectric spectroscopy of single human erythrocytes at physiological ionic strength: Dispersion of the cytoplasm. *Biophys. J.* **71** 495-506
- Gimsa J, Marszalek P, Loewe U and Tsong T Y 1992 Electroporation in rotating electric fields. *Bioelectrochem. Bioener.* **29** 81-9
- Gimsa J, Marszalek P, Loewe U and Tsong T Y 1991a Dielectrophoresis and electrorotation of neurospora slime and murine myeloma cells. *Biophys. J.* **60** 749-60
- Gimsa J, Glaser R and Fuhr G 1991b Theory and application of the rotation of biological cells in rotating electric fields (Electrorotation). *Physical characterization of biological cells* ed W Schütt, H Klinkmann, I Lamprecht and T Wilson (Berlin: Verlag Gesundheit GmbH) pp 295-323
- Gimsa J, Donath E and Glaser R 1988a Evaluation of the data of simple cells by electrorotation using square-topped fields. *Bioelectrochem. Bioener.* **19** 389-96

- 
- Gimsa J, Glaser R and Fuhr G 1988b Remarks on the field distribution in four electrode chambers for electrorotational measurements. *Studia biophysica* **125** 71-6
- Glaser R 2001 *Biophysics* (Berlin: Springer-Verlag)
- Glaser R W and Gimsa J 1993 Gradual changes of membrane properties at high transmembrane electric potential simulate a breakdown threshold. *Electricity and magnetism in biology and medicine* ed M Blank (San Francisco: San Francisco Press, Inc.) pp 135-7
- Glaser R W, Leikin S L, Chernomordik L V, Pastushenko V F and Sokirko A I 1988 Reversible electrical breakdown of lipid bilayers: formation and evolution of pores. *Biochim. Biophys. Acta* **940** 275-87
- Gothelf A, Mir L M and Gehl J 2003 Electrochemotherapy: results of cancer treatment using enhanced delivery of bleomycin by electroporation. *Canc. Treat. Rev.* **29** 371-87
- Grimes S E 2002 A basic laboratory manual for the small-scale production and testing of I-2 Newcastle disease vaccine. *RAP publication*: ISBN 974-7946-26-2 (FAO-APHCA, Bangkok, Thailand)
- Grosse C and Schwan H P 1992 Cellular membrane potentials induced by alternating fields. *Biophys. J.* **63** 1632-42
- Gunsalus I C and Stanier R Y 1960 The bacterial protoplasm: composition and organization. *The bacteria: a treatise on structure and function* ed S E Luria (New York: Academic Press) pp 1-34

- 
- Hibino M, Itoh H and Kinoshita K Jr 1993 Time courses of cell electroporation as revealed by submicrosecond imaging of transmembrane potential. *Biophys. J.* **64** 1789-800
- Hibino M, Shigemori M, Itoh H, Nagayama K, and Kinoshita K Jr 1991 Membrane conductance of an electroporated cell analyzed by submicrosecond imaging of transmembrane potential. *Biophys. J.* **59** 209-20
- Hoffman J F 1987 On the mechanism and measurement of shape transformations of constant volume of human red blood cells. *Blood Cells* **12** 256-586
- Hofmann G A, Dev S B, Dimmer S and Nanda G S 1999 Electroporation therapy: a new approach for the treatment of head and neck cancer. *IEEE Transactions on Biomedical Engineering* **46** 752-9
- Hölzel R 1993 Electric field calculation for electrorotation electrodes. *J. Phys. D: Appl. Phys.* **26** 2112-16
- Huang Y and Rubinsky B 2003 Flow-through micro-electroporation chip for high efficiency single-cell genetic manipulation. *Sensors and Actuators A* **104** 205-12
- Huang Y and Rubinsky B 2001 Microfabricated electroporation chip for single cell membrane permeabilization. *Sensors and Actuators A* **89** 242-9
- Huang Y and Rubinsky B 1999 Micro-electroporation: improving the efficiency and understanding of electrical permeabilization of cells. *Biomed. Microdevices* **2** 145-50
- Huang Y, Wang X-B, Tame J A and Pethig R 1993 Electrokinetic behaviour of colloidal particles in traveling electric fields: studies using yeast cells. *J. Phys. D: Appl. Phys.* **26** 1528-35

- 
- Hughes M P 2000 AC electrokinetics: applications for nanotechnology. *Nanotechnology* **11** 124-32
- Hughes M P 1998 Computer-aided analysis of conditions for optimizing practical electrorotation. *Phys. Med. Biol.* **43** 3639-48
- Hughes M P, Archer S and Morgan H 1999 Mapping the electrorotational torque in planar microelectrodes. *J. Phys. D: Appl. Phys.* **32** 1548-52
- Hughes M P, Wang X-B, Becker F F, Gascoyne P R C and Pethig R 1994 Computer-aided analyses of electric fields used in electrorotation studies. *J. Phys. D: Appl. Phys.* **27** 1564-70
- Jerry R A, Popel A S and Brownell W E 1996 Potential distribution for a spheroidal cell having a conductive membrane in an electric field. *IEEE Trans. Biomed. Eng.* **43** 970-2
- Jones T B 1995 *Electromechanics of particles* (USA: Cambridge University Press)
- Junior P, Deitinghoff H, Halfmann K D, Neumann W and Zoubek N 1983 Design considerations on peak electrical fields and maximum beam currents for heavy ion RFQ linacs. *IEEE Trans. Nuc. Sci.* **NS30** 2639-41
- Katrina T, Cathleen C, Yvette R, Emmanuel A, Evan H, Didier L, Rachel T, Alan K, and Richard W 2004 Generation of dendritic cell-tumor cell hybrids by electrofusion for clinical vaccine application. *Cancer Immunology, Immunotherapy* **53** 705-14
- Katsov K, Müller M and Schick M 2006 Field theoretic study of bilayer membrane fusion: II Mechanism of a stalk-hole complex. *Biophys. J.* **90** 915-26

- 
- Khine M, Lau A, Ionescu-Zanetti C, Seo J and Lee L P 2005 A single cell electroporation chip. *Lab Chip* **5** 38-43
- Kim J A, Cho K, Shin Y S, Jung N, Chung C and Chang J K 2007 A multi-channel electroporation microchip for gene transfection in mammalian cells. *Biosensors and Bioelectronics* **22** 3273-77
- Kinosita K Jr and Tsong T Y 1977 Voltage-induced pore formation and hemolysis of human erythrocytes. *Biochimica et Biophysica Acta* **47** 1227-242
- Kjaergaard J, Shimizu K and Shu S 2003 Electroporation of syngeneic dendritic cells and tumor generates potent therapeutic vaccine. *Cellular Immunology* **225** 65-74
- Kotnik T, Mir L M, Flisar K, Puc M and Miklavcic D 2001 Cell membrane electroporation by symmetrical bipolar rectangular pulses: part I. Increased efficiency of permeabilization. *Bioelectrochemistry* **54** 83-90
- Kotnik T, Pucihar G, Rebersek M, Miklavcic D and Mir L M 2003 Role of pulse shape in cell membrane electroporation. *Biochim. Biophys. Acta* **1614** 193-200
- Kozlov M M, Leikin S L, Chernomordik L V, Markin V S and Chizmadzhev Y A 1989 Stalk mechanism of vesicle fusion: intermixing of aqueous contents. *Eur Biophys. J.* **17** 121-9
- Kramar P, Miklavcic D and Lebar A M 2007 Determination of the lipid bilayer breakdown voltage by means of linear rising signal. *Bioelectrochemistry* **70** 23-7

- 
- Lampa A 1906 Über Rotation im electrostatischen Drehfelde. *Wiener Berichte* **15** 1659-90
- Lebar A M and Miklavcic D 2001 Cell electropermeabilization to small molecules *in vitro*: control by pulse parametes. *Radiol. Oncol.* **35** 193-202
- Lin Y-C and Huang M-Y 2001 Electroporation microchips for *in vitro* gene transfection. *J. Micromech. Microeng.* **11** 542-7
- Lin Y-C, Li M and Wu C-C 2004 Simulation and experimental demonstration of the electric field assisted electroporation microchip for in vitro gene delivery enhancement. *Lab Chip* **4** 104-8
- Lin Y-C, Li M, Fan C-S and Wu L-W 2003 A microchip for electroporation of primary endothelial cells. *Sensors and Actuators A* **108** 12-9
- Lippert S and Gimsa J 2002 High resolution measurements of dielectric cell properties by a combination of AC-electrokinetic effects. *Proc. 2<sup>nd</sup> International Workshop on Biological Effects of EMFs* ed P Kostarakis (Rhodes, Greece) pp 830-6
- Lu H, Schmidt M A and Jensen K F 2005 A microfluidic electroporation device for cell lysis. *Lab Chip* **5** 23-9
- Markin V S and Tsong T Y 1991 Frequency and concentration windows for the electric activation of a membrane active transport system. *Biophys. J.* **59** 1308-16
- Markin V S, Kozlov M M and Borovjagin V L 1984 On the theory of membrane fusion: the stalk mechanism. *Gen. Physiol. Biophys.* **3** 361-77

- 
- Marszalek P, Liu D-S and Tsong T Y 1990 Schwan equation and transmembrane potential induced by alternating electric field. *Biophys. J.* **58** 1053-58
- Maswiwat K, Holtappels M and Gimsa J 2007a Optimizing the electrode shape for four-electrode electrorotation chips *ScienceAsia* **33** 61-7
- Maswiwat K, Wachner D, Warnke R and Gimsa J 2007b Simplified equations for the transmembrane potential induced in ellipsoidal cells of rotational symmetry *J. Phys. D: Appl. Phys.* **40** 914-23
- Maswiwat K, Holtappels M and Gimsa J 2006 On the field distribution in electrorotation chambers-influence of electrode shape *Electrochimica Acta* **51** 5215-20
- Miklavcic D, Corovic S, Pucihar G and Pavselj N 2006 Importance of tumour coverage by sufficiently high local electric field for effective electrochemotherapy. *EJC Supplements* **4** 45-51
- Mir L M and Orłowski S 1999 Mechanisms of electrochemotherapy. *Advance Drug Delivery Reviews* **35** 107-18
- Morgan H, Izquierdo A G, Bakewell D, Green N G and Ramos A 2001 The dielectrophoretic and travelling-wave forces generated by interdigitated electrode arrays: analytical solution using Fourier series. *J. Phys. D: Appl. Phys.* **34** 1553-61
- Morgan H, Green N G, Hughes M P, Monaghan W and Tan T C 1997 Large-area travelling-wave dielectrophoresis particle separator. *J. Micromech. Microeng.* **7** 65-70



- 
- Müller K J, Sukhorukov V L and Zimmermann U 2001 Reversible electropermeabilization of mammalian cells by high-intensity, ultra-short pulses of submicrosecond duration. *J. Membrane Biol.* **184** 161-70
- Needham D and Hochmuth R M 1989 Electro-mechanical permeabilization of lipid vesicles: role of membrane tension and compressibility. *Biophys. J.* **55** 1001-9
- Neumann E 1989 The relaxation hysteresis of membrane electroporation. *Electroporation and electrofusion in cell biology* ed E Neumann, A E Sowers and C A Jordan (New York: Plenum Press) pp 61-82
- Neumann E, Toensing K, Kakorin S, Budde P and Frey J 1998 Mechanism of electroporative dye uptake by mouse B cells. *Biophys. J.* **74** 98-108
- Neumann E, Sprafke A, Boldt E and Wolf H 1992 Biophysical considerations of membrane electroporation. *Guide to electroporation and electrofusion* ed D C Chang, B M Chassy, J A Saunders and A E Sowers (San Diego, California: Academic Press, Inc.) pp 77-90
- Neumann E, Sowers A E and Jordan C A 1989 *Electroporation and electrofusion in cell biology* (New York: Plenum Press)
- Nikinmaa M 1990 *Vertebrate red blood cells* (Berlin: Springer-Verlag) pp 44-61
- Olofsson J, Nolkrantz K, Ryttsen F, Lambie B A, Weber S G and Orw Parker K H and Winlove C P 1999 The deformation of spherical vesicles with permeable, constant-area membranes: application to the red blood cell. *Biophys. J.* **77** 3096-107

- 
- Pethig R, Talary M S and Lee R S 2003 Enhancing traveling-wave dielectrophoresis with signal superposition. *IEEE Engineering in Medicine and Biology Magazine* **November/December** 43-50
- Pliquett U 2003 Joule heating during solid tissue electroporation. *Medical & Biological Engineering & Computing* **41** 215-9
- Pohl H A 1978 *Dielectrophoresis* (Cambridge: Cambridge University Press)
- Puc M, Kotnik T, Mir L M, Miklavcic D 2003 Quantitative model of small molecules uptake after in vitro cell electropermeabilization. *Bioelectrochemistry* **60** 1-10
- Pucihar G, Kotnik T, Kanduser M and Miklavcic D 2001 The influence of medium conductivity on electropermeabilization and survival of cells in vitro. *Bioelectrochemistry* **54** 107-15
- Radu M, Ionescu M, Irimescu N, Iliescu K, Pologea-Moraru R and Kovacs E 2005 Orientation behavior of retinal photoreceptors in alternating electric fields. *Biophys. J.* **89** 3548-54
- Rols M-P and Teissié J 1998 Electropermeabilization of mammalian cells to macromolecules: control by pulse duration. *Biophys. J.* **75** 1415-23
- Rols M P and Teissié J 1990 Electropermeabilization of mammalian cells: quantitative analysis of the phenomenon. *Biophys. J.* **58** 1089-98
- Rubinsky B 2007 Irreversible electroporation in medicine. *Technology in Cancer Research and Treatment* **6** 255-9

- 
- Sale A J H and Hamilton W A 1968 Effects of high electric fields on microorganisms III. Lysis of erythrocytes and protoplasts. *Biochim. Biophys. Acta* **163** 37-43
- Sale A J H and Hamilton W A 1967 Effects of high electric fields on microorganisms I. Killing of bacteria and yeasts. *Biochim. Biophys. Acta* **148** 781-8
- Schoenbach K H, Katsuki S, Stark R H, Buescher E S and Beebe S J 2002 Bioelectrics-new applications for pulsed power technology. *IEEE Transactions on Plasma Science* **30** 293-300
- Schwan H P 1988 Dielectric spectroscopy and electro-rotation of biological cells. *Ferroelectrics* **86** 205-23
- Schwan H P 1983a Biophysics of the interaction of electromagnetic energy with cells and membranes. *Biological effects and dosimetry of nonionizing radiation* ed M Grandolfo, S M Michaelson and A Rindi (New York: Plenum Press) pp 213-31
- Schwan H P 1983b Dielectric properties of biological tissue and cells at RF- and MW-frequencies. *Biological effects and dosimetry of nonionizing radiation* ed M Grandolfo, S M Michaelson and A Rindi (New York: Plenum Press) pp 195-211
- Sekine K, Torii N, Kuroda C and Asami K 2002 Calculation of dielectric spectra of suspensions of rod-shaped cells using boundary element method. *Bioelectrochemistry* **57** 83-7
- Smith K C, Neu J C and Krassowska W 2004 Model of creation and evolution of stable electropores for DNA delivery. *Biophys. J.* **86** 2813-26

- 
- Stille U 1944 Der Entmagnetisierungsfaktor und Entelektrisierungsfaktor für Rotationsellipsoide. *Archiv Elektrotechnik* **38** 91-101 (in German)
- Stokes R H, Crandall K R, Stovall J E and Swenson D A 1979 RF Quadrupole beam dynamics. *IEEE Trans. Nuc. Sci.* **NS26** 3469-79
- Stratton J A 1941 *Electromagnetic theory* (New York: McGraw-Hill)
- Sudsiri J, Wachner D and Gimsa J 2007 On the temperature dependence of the dielectric membrane properties of human red blood cells. *Bioelectrochemistry* **70** 134-40
- Sugar I P and Neumann E 1984 Stochastic model for electric field-induced membrane pores electroporation. *Biophysical Chemistry* **19** 211-25
- Takashima S, Chang S and Asakura T 1985 Shape change of sickled erythrocytes induced by pulsed rf electrical fields. *Proc. Natl. Acad. Sci. USA* **82** 6860-64
- Teissié J and Ramos C 1998 Correlation between electric field pulse induced long-lived permeabilization and fusogenicity in cell membranes. *Biophys. J.* **74** 1889-98
- Teissié J and Rols M-P 1993 An experimental evaluation of the critical potential difference inducing cell membrane electropermeabilization. *Biophys. J.* **65** 409-13
- Tien H T and Ottova A 2003 The bilayer lipid membrane (BLM) under electrical fields. *IEEE Transactions on Dielectrics and Electrical Insulation* **10** 717-27
- Trefzer U and Walden P 2003 Hybrid-cell vaccines for cancer immune therapy. *Molecular Biotechnology* **25** 63-9

- 
- Tsong T Y 1992 Time sequence of molecular events in electroporation. *Guide to electroporation and electrofusion* ed D C Chang, B M Chassy, J A Saunders and A E Sowers (San Diego, California: Academic Press, Inc.) pp 47-61
- Tsong T Y 1991 Electroporation of cell membranes *Biophys. J.* **60** 297-306
- Tsong T Y 1990 Electrical modulation of membrane proteins: enforced conformational oscillations and biological energy and signal transductions. *Annu. Rev. Biophys. Biophys. Chem.* **19** 83-106
- Tsong T Y 1989 Electroporation of cell membranes: Mechanism and applications. *Electroporation and electrofusion in cell biology* ed E Neumann, A E Sowers and C A Jordan (New York: Plenum Press) pp 149-63
- Tuukkanen S; Toppari J J; Hytonen V P; Kuzyk A; Kulomaa M S and Torma P 2005 Dielectrophoresis as a tool for nanoscale DNA manipulation. *International J. Nanotechnology* **2** 280-91
- Valic B, Golzio M, Pavlin M, Schatz A, Faurie C, Gabriel B, Teissie J, Rols M-P and Miklavcic D 2003 Effect of electric field induced transmembrane potential on spheroidal cells: theory and experiment. *Eur. Biophys. J.* **32** 519-28
- Wachner D, Simeonova M and Gimsa J 2002 Estimating the subcellular absorption of electric field energy: equations for an ellipsoidal single shell model. *Bioelectrochemistry* **56** 211 –3
- Warnke R 2003 Eine Approximationsfunktion zur Berechnung des Feldverstaerkungsfaktors sphaeroider Zellen. *Laboratory Report (Forschungspraktikum) Department of Biology, University of Rostock (in German)*

- 
- Weaver J C 2000 Electroporation of cells and tissues. *IEEE Transaction on Plasma Science* **28** 24-33
- Weaver J C and Chizmadzhev Y A 1996 Theory of electroporation: a review. *Bioelectrochemistry and Bioenergetics* **41** 135-60
- Weise J B, Maune S, Görögh T, Kabelitz D, Arnold N, Pfisterer J, Hilpert F and Heiser A 2004 A dendritic cell based hybrid cell vaccine generated by electrofusion for immunotherapy strategies in HNSCC. *Auris. Nasus. Larynx* **31** 149-53
- Winterhalter M, Klotz K-H and Benz R 1996 High-intensity field effects on artificial lipid bilayer membranes: Theoretical considerations and experimental evidence. *Electromanipulation of cells* ed U Zimmermann and G A Neil (Boca Raton: CRC Press) pp 137-72
- Wolf H, Rols M P, Boldt E, Neumann E and Teissié J 1994 Control by pulse parameters of electric field-mediated gene transfer in mammalian cells. *Biophys. J.* **66** 524-31
- Xie T-D and Tsong T Y 1992 Study of mechanisms of electric field-induced DNA transfection III. Electric parameters and other conditions for effective transfection. *Biophys. J.* **63** 28-34
- Xie T-D and Tsong T Y 1990 Study of mechanisms of electric field-induced DNA transfection II. Transfection by low-amplitude, low frequency alternating electric fields. *Biophys. J.* **58** 897-903
- Xie T-D, Chen Y, Marszalek P and Tsong T Y 1997 Fluctuation-driven directional flow in biochemical cycle: further study of electric activation of Na,K pumps. *Biophys. J.* **72** 2496-502

- 
- Xie T-D, Marszalek P, Chen Y and Tsong T Y 1994 Recognition and processing of randomly fluctuating electric signals by Na,K-ATPase. *Biophys. J.* **67** 1247-51
- Xie T-D, Sun L and Tsong T Y 1990 Study of mechanisms of electric field-induced DNA transfection I. DNA entry by surface binding and diffusion through membrane pores. *Biophys. J.* **58** 13-91
- Yeh C-J G, Hsi B-L and Faulk W P 1981 Propidium iodide as a nuclear marker in immunofluorescence. II. Use with cellular identification and viability studies. *J. Immunol. Methods* **43** 269-75
- Zimmermann U 1996 The effect of high intensity electric field pulses on eukaryotic cell membranes: fundamentals and applications. *Electromanipulation of Cells* ed U Zimmermann and G A Neil (Boca Raton, FL: CRC Press) pp 1-106
- Zimmermann U and Neil G A 1996 *Electromanipulation of cells* (Boca Raton: CRC Press)
- Zimmermann U and Benz R 1980 Dependence of the electrical breakdown voltage on the charging time in *Valonia utricularis*. *Membrane Biol.* **53** 33-43
- Zimmermann, U, Friedrich U, Mussauer H, Gessner P, Hämel K and Sukhorukov V 2000 Electromanipulation of mammalian cells: fundamentals and application. *IEEE Trans. Plasma Sci.* **28** 72-82

# Erklärung

Hiermit erkläre ich, daß ich die vorliegende Dissertation selbstständig verfasst, noch nicht anderweitig für Prüfungszwecke vorgelegt, keine anderen als die angegebenen Quellen oder Hilfsmittel verwendet sowie wörtliche und sinngemäße Zitate als solche gekennzeichnet habe.

Rostock, October 2007

Kanokkan Maswiwat



# Curriculum vitae

## Personal data

Name	Mrs. Kanokkan Maswiwat
Date and place of birth	25.03.1974 in Phatthalung, Thailand
Nationality	Thai

## Education

1993-1996	Bachelor of Education (with honor), Physics Thaksin University, Songkla, Thailand
1997-2000	Master of Science, Physics Prince of Songkla University, Songkla, Thailand Thesis title: "The deformation of <i>Dendrobium</i> sp. protoplasts in AC electric fields"
02/2003-03/2003	Visit at the Biophysics Group (Prof. Jan Gimsa, chair), Institute of Biology, University of Rostock, Germany
10/2003-10/2007	Doctoral study in Biophysics at University of Rostock, Germany, funded by the Royal Thai government and supported by grant StSch 20020418A of the Bundesamt für Strahlenschutz to Prof. Dr. J. Gimsa and by the IPP at the University of Rostock supported by DAAD, BMBF and DFG.

## Work / Research Experiences

- since 04/2000                      Lecturer in Physics, Department of Physics, Faculty of Science and Technology, Suratthani Rajabhat University, Suratthani, Thailand
- 2001-2002                              Research fellowship: “Effect of AC electric field on growth of *Acetobacter xylinum* bacteria”, Maswiwat K and Panwichian S (in Thai), supported by Suratthani Rajabhat University, Thailand
- 2002-2003                              Research fellowship: “The study of tap water quality supplied for Suratthani Rajabhat Institute”, Intawongse M, Kongchouy N, Maswiwat K and Sukkaewmanee P (in Thai), supported by Suratthani Rajabhat University, Thailand

# List of Publications and Presentations

## Publications

1. Wanichapichart P, Maswiwat K and Kanchanapoom K 2002 Elastic constant of *Dendrobium* protoplasts in AC electric fields. *Songklanakarin J. Sci. Technol.* **24** 799-806
2. Maswiwat K, Holtappels M and Gimsa J 2005 Optimizing the electrode shape of electrorotation chambers. *Proceedings of the 3<sup>rd</sup> Regional Symposium on Membrane Science & Technology 2005* (Bandung, Indonesia) p 68
3. Maswiwat K, Wachner D, Westendorf C and Gimsa J 2005 Handy equations for the transmembrane potential induced on ellipsoidal cells of rotational symmetry. *Proceedings of the 3<sup>rd</sup> Regional Symposium on Membrane Science & Technology 2005* (Bandung, Indonesia) p 65
4. Maswiwat K, Holtappels M and Gimsa J 2005 On the field distribution in electrorotation chambers-influence of electrode shape. *Proceedings of the XVIII International Symposium on Bioelectrochemistry and Bioenergetics of the Bioelectrochemical Society (BES) and 3<sup>rd</sup> Spring Meeting Bioelectrochemistry of the International Society of Electrochemistry (ISE)* (Coimbra, Portugal) p P-194
5. Maswiwat K, Holtappels M and Gimsa J 2006 On the field distribution in electrorotation chambers-influence of electrode shape. *Electrochimica Acta* **51** 5215-20
6. Maswiwat K, Holtappels M and Gimsa J 2007 Optimizing the electrode shape for four-electrode electrorotation chips. *ScienceAsia* **33** 61-7

7. Maswiwat K, Wachner D, Warnke R and Gimsa J 2007 Simplified equations for the transmembrane potential induced on ellipsoidal cells of rotational symmetry. *J. Phys. D: Appl. Phys.* **40** 914-23
8. Maswiwat K, Wachner D and Gimsa J 2007 Effects of cell orientation and electric field frequency on the transmembrane potential induced in ellipsoidal cells. (submitted)

## **Presentations**

1. Maswiwat K, Wachner D, Westendorf C and Gimsa J 2005 Handy equations for the transmembrane potential induced on ellipsoidal cells of rotational symmetry. 3<sup>rd</sup> *Regional Symposium on Membrane Science & Technology 2005* (Bandung, Indonesia) **Poster**
2. Maswiwat K, Holtappels M and Gimsa J 2005 Optimizing the electrode shape of electrorotation chambers. 3<sup>rd</sup> *Regional Symposium on Membrane Science & Technology 2005* (Bandung, Indonesia) **Poster**
3. Maswiwat K, Holtappels M and Gimsa J 2005 On the field distribution in electrorotation chambers-influence of electrode shape. *XVIII International Symposium on Bioelectrochemistry and Bioenergetics of the Bioelectrochemical Society (BES) and 3<sup>rd</sup> Spring Meeting Bioelectrochemistry of the International Society of Electrochemistry (ISE)* (Coimbra, Portugal) **Poster**
4. Maswiwat K 2007 Effects of cell orientation and field frequency on the transmembrane potential induced in ellipsoidal cells by external electric fields. *Seminar of the International Postgraduate Programmes (IPP) supported by DAAD, BMBF and DFG* (University of Rostock, Germany) **Oral**